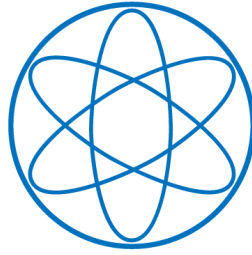


PHYSIK - DEPARTMENT



SIGNAL AND BACKGROUND STUDIES FOR THE SEARCH OF
NEUTRINOLESS DOUBLE BETA DECAY IN GERDA

MATTEO AGOSTINI



TECHNISCHE UNIVERSITÄT MÜNCHEN

2013

TECHNISCHE UNIVERSITÄT MÜNCHEN

Lehrstuhl E15 für Experimentalphysik und Astroteilchenphysik

Signal and background studies for the search of neutrinoless double beta decay in GERDA

Matteo Agostini

Vollständiger Abdruck der von der Fakultät für Physik der Technischen Universität München zur Erlangung des akademischen Grades eines

Doktors der Naturwissenschaften (Dr. rer. nat.)

genehmigten Dissertation.

Vorsitzender:

Univ.-Prof. Dr. A. Ibarra

Prüfer der Dissertation:

1. Univ.-Prof. Dr. St. Schönert

2. Hon.-Prof. A. C. Caldwell, Ph.D.

Die Dissertation wurde am 21.03.2013 bei der Technischen Universität München eingereicht und durch die Fakultät für Physik am 24.04.2013 angenommen.

Abstract

Various extensions of the Standard Model of particle physics predict the existence of a lepton-number-violating nuclear transition called neutrinoless double beta decay ($0\nu\beta\beta$). Any realization of this transition requires physics beyond the Standard Model and implies that neutrinos have a Majorana mass component. Besides one unconfirmed claim from a part of the Heidelberg-Moscow collaboration ($T_{1/2} = 1.19^{+0.37}_{-0.23} \cdot 10^{25}$ yr), $0\nu\beta\beta$ has not been observed to date. The GERDA experiment searches for this transition in ^{76}Ge , by operating bare HPGe detectors in ultra-pure liquid argon. GERDA will scrutinize the claim in the current data-taking phase (Phase I, Nov 2011 - May 2013). After an upgrade of the experimental apparatus, a second phase is planned to increase the sensitivity by one order of magnitude and start the exploration of $0\nu\beta\beta$ half-life values at the level of 10^{26} yr within a few years of data taking (Phase II).

In this dissertation, a complete decomposition of the Phase I background has been obtained at the energy of interest for $0\nu\beta\beta$ search ($Q_{\beta\beta}$) by a combined use of pulse shape analysis, Monte Carlo simulations and spectral fitting. The analysis has been performed on the first data collected in Phase I. The data set has a total exposure of $6.1 \text{ kg}\cdot\text{yr}$ and average background index of $20^{+6}_{-4} \cdot 10^{-3} \text{ cts}/(\text{keV}\cdot\text{kg}\cdot\text{yr})$. Procedures for data reduction have been developed and defined, including the algorithms used for processing the digitized signals and to monitor the data quality. The background index was found to be dominated by the gamma-rays of ^{214}Bi , ^{208}Tl and ^{42}K , accounting for $14.7^{+4.8}_{-4.4} \cdot 10^{-3} \text{ cts}/(\text{keV}\cdot\text{kg}\cdot\text{yr})$. Secondary components were identified in the beta-rays from ^{42}K and ^{214}Bi , and the alpha-rays from ^{210}Po .

An integrated simulation tool – reproducing the response of HPGe detectors to charged particles and radiations – has been implemented and validated to support the development of BEGe detectors for Phase II. This tool has been applied to elaborate the first comprehensive modeling of the signal formation and evolution for this particular detector design. It was also used, together with experimental measurements on prototype detectors, to estimate the pulse shape discrimination performance achievable with BEGe detectors on the critical background components expected in Phase II. The recently proposed A/E method was found capable of suppressing all the considered backgrounds while maintaining a $(86 \pm 3)\%$ acceptance of the $0\nu\beta\beta$ signal. The survival probabilities estimated at $Q_{\beta\beta}$ are: $(0.9^{+0.4}_{-0.2})\%$ and $(4.5 \pm 0.3)\%$ for cosmogenic ^{60}Co and ^{68}Ga decays inside the detector; $< 1.6\%$ (95% C.I.) for beta-rays penetrating the detector n+ surface; $< 8\%$ (95% C.I.) for alpha-decays on the p+ surface.

Given the decomposition of the Phase I background and the estimated pulse shape discrimination performances, it has been shown that GERDA Phase II has the potentiality to reach its background index goal of $\lesssim 10^{-3} \text{ cts}/(\text{keV}\cdot\text{kg}\cdot\text{yr})$ and to probe half-life values between $1\text{-}2 \cdot 10^{26}$ yr in less than three years of data taking.

Zusammenfassung

Verschiedene Erweiterungen des Standard-Modells der Teilchenphysik sagen die Existenz des sogenannten neutrinolosen doppelten Beta-Zerfalls ($0\nu\beta\beta$) voraus. Dieser Kernübergang würde die Leptonenzahl-Erhaltung verletzen. Jede Form dieses Übergangs ist nur mit Physik jenseits des Standard-Modells realisierbar und impliziert, dass Neutrinos eine Majorana-Massenkomponente besitzen. Abgesehen von einem unbestätigten Resultat seitens eines Teils der Heidelberg-Moskau Kollaboration ($T_{1/2} = 1.19^{+0.37}_{-0.23} \cdot 10^{25}$ a), wurde der $0\nu\beta\beta$ bis jetzt noch nicht beobachtet. Das GERDA Experiment sucht nach diesem Übergang in ^{76}Ge indem es nackte HPGe Detektoren in ultra-reinem flüssigen Argon betreibt. In der laufenden Datennahme untersucht GERDA die Halbwertszeit der behaupteten Beobachtung (Phase I, Nov 2011 - May 2013). Nach einer Verbesserung des experimentellen Aufbaus ist eine weitere Datennahme geplant. Diese Phase wird eine um eine Größenordnung vergrößerte Sensitivität besitzen und innerhalb weniger Jahre kann der Halbwertszeitbereich des $0\nu\beta\beta$ um 10^{26} a untersucht werden (Phase II).

In der vorliegenden Arbeit wird eine vollständige Aufschlüsselung des Phase I Untergrunds in der Nähe der Zerfallsenergie von $0\nu\beta\beta$ ($Q_{\beta\beta}$) vorgestellt. Diese wurde erreicht durch die kombinierte Nutzung von Puls-Form Analysen, Monte Carlo Simulationen und spektraler Fits. Die Analyse wurde mit den ersten Daten der Phase I durchgeführt. Das Datenset umfasst eine Exposition von $6.1 \text{ kg} \cdot \text{a}$ und einen mittleren Untergrundindex von $20^{+6}_{-4} \cdot 10^{-3} \text{ cts}/(\text{keV} \cdot \text{kg} \cdot \text{yr})$. Es wurden Prozeduren für die Daten-Reduktion entwickelt, die die Algorithmen für das Prozessieren der digitalisierten Signale und die Überwachung der Datenqualität beinhalten. Der Untergrundindex wird durch Gamma-Strahlen von ^{214}Bi , ^{208}Tl und ^{42}K dominiert, mit einem Beitrag von $14.7^{+4.8}_{-4.4} \cdot 10^{-3} \text{ cts}/(\text{keV} \cdot \text{kg} \cdot \text{yr})$. Weitere Komponenten wurden als Beta-Strahlen von ^{42}K und ^{214}Bi sowie Alpha-Strahlen von ^{210}Po identifiziert.

Ein integriertes Simulationspaket – zur Reproduktion der Signale von HPGe Detektoren ausgelöst durch geladene Teilchen und Strahlung – wurde implementiert und validiert um die Entwicklung der BEGe Detektoren für Phase II zu unterstützen. Mittels dieses Werkzeugs wurde die erste vollständige Modellierung der Signalentstehung und -entwicklung für diesen bestimmten Detektortyp vorgenommen. Die Simulation wurde zusammen mit experimentellen Messungen an Prototypdetektoren benutzt, um die Puls-Form Diskriminierungsfähigkeit von BEGe Detektoren für die kritischen Untergrundkomponenten in Phase II abzuschätzen. Es konnte gezeigt werden, dass die kürzlich vorgestellte A/E Methode sämtliche betrachtete Untergründe unterdrücken kann, wobei eine Akzeptanz des $0\nu\beta\beta$ Signals von $(86 \pm 3)\%$ erhalten bleibt. Die abgeschätzten Überlebenswahrscheinlichkeiten bei $Q_{\beta\beta}$ sind: $(0.9^{+0.4}_{-0.2})\%$ und $(4.5 \pm 0.3)\%$ für ^{60}Co und ^{68}Ga Zerfälle innerhalb des Detektors; $< 1.6\%$ (95% C.I.) für durch die n+ Oberfläche des Detektors eindringende Beta-Strahlen; $< 8\%$ (95% C.I.) für Alpha-Zerfälle auf der p+ Oberfläche.

Mit der gegebenen Aufschlüsselung des Phase I Untergrunds und der abgeschätzten Puls-Form Diskriminierungsfähigkeit, konnte gezeigt werden, dass GERDA Phase II das Potenzial besitzt das Untergrundindexziel von $\lesssim 10^{-3} \text{ cts}/(\text{keV} \cdot \text{kg} \cdot \text{yr})$ zu erreichen und damit in weniger als drei Jahren Datennahme Halbwertszeiten von $1\text{-}2 \cdot 10^{26}$ a zu untersuchen.

Table of Contents

1	Introduction	1
1.1	Double beta decay and neutrino phenomenology	1
1.2	Experimental aspects of the $0\nu\beta\beta$ search	8
1.3	The search of $0\nu\beta\beta$ decay in ^{76}Ge and the GERDA experiment	11
1.4	Outline of the dissertation	13
 GERDA Phase I: data processing and background analysis		
2	Data processing and spectral analysis	17
2.1	Detector array configuration and signal read-out	17
2.2	Data processing	20
2.2.1	Off-line digital signal processing	21
2.2.2	Signal quality monitoring	23
2.2.3	Calibration	25
2.3	Spectral analysis	28
2.4	Conclusions	33
3	Background decomposition at $Q_{\beta\beta}$	35
3.1	Considered background sources	35
3.2	Pulse shape analysis	38
3.2.1	Signal modeling of coaxial detectors	38
3.2.2	Discrimination method and application	40
3.2.3	Energy dependence of the cut acceptance	43
3.3	Background decomposition at $Q_{\beta\beta}$	44
3.3.1	Monte Carlo simulation of beta-emitting isotopes	46
3.3.2	Statistical analysis of the gamma-induced background	50
3.3.3	Spectral fitting of ^{210}Po degraded alpha-events	51
3.3.4	Overview	55
3.4	GERDA Phase I sensitivity	56

3.5	Conclusions	58
-----	-----------------------	----

GERDA Phase II: detector development and off-line background reduction techniques

4	Overview of the Phase II HPGe detector design and development	63
5	Signal modeling	69
5.1	Overview of the simulation	69
5.1.1	Charge collection and signal formation	70
5.1.2	Read-out electronics response and noise	72
5.2	Modeling of BEGe detectors	72
5.2.1	The electric field inside BEGe detectors	72
5.2.2	Signal development in dependence of the interaction position	74
5.2.3	Discrimination between single-site and multiple-site events	78
5.3	Validation of the simulation	80
5.3.1	Experimental setup and data processing	80
5.3.2	Pulse shape comparison with low energy gamma-ray beams	81
5.3.3	Rise time and A/E distribution studies	84
5.4	Conclusions	87
6	Background rejection and signal identification studies	91
6.1	Decays internal to the germanium crystal	91
6.1.1	A/E cut performance on simulated and experimental data	92
6.1.2	$0\nu\beta\beta$ decay of ^{76}Ge and intrinsic cosmogenic isotopes	95
6.2	Energy depositions on the p+ B-implanted electrode and groove surfaces . .	97
6.2.1	Experimental setup and data acquisition system	98
6.2.2	Data processing and selection	100
6.2.3	Data analysis	101
6.3	Energy depositions in the Li-diffused surface layer forming the n+ electrode	106
6.4	Conclusions	109
7	Background expectation and experimental sensitivity	111
7.1	Backgrounds expected in Phase II configuration	111
7.2	Active techniques for background reduction	115
7.3	Surviving backgrounds and sensitivity to the $0\nu\beta\beta$ signal	118
7.4	Conclusions and discussion	122
	Summary and outlook	125

Appendix

A Framework for digital signal processing and analysis	131
A.1 Concept and design	131
A.1.1 Multi-level data structure	132
A.1.2 Modular digital signal processing	133
A.2 Implementation	134
A.2.1 Conversion of raw data to the analysis format	134
A.2.2 Implementation of digital signal processing	137
A.2.3 Utilities	138
A.2.4 The graphical interface	139
A.3 Application and Benchmarking	139
A.4 List of software packages	140
B Module description	141
C Statistical models	145
C.1 Signal in presence of measured background	145
C.1.1 Gamma-line intensities	146
C.1.2 p+ electrode alpha- and beta-event count rate at $Q_{\beta\beta}$	147
C.2 Signal in presence of hypothetical background	147
Bibliography	151

List of abbreviations

$0\nu\beta\beta$	Neutrinoless double beta decay
$2\nu\beta\beta$	Two-neutrino double beta decay
$^{\text{nat}}\text{Ge}$	Natural Ge material
$^{\text{enr}}\text{Ge}$	Ge material enriched in ^{76}Ge
$Q_{\beta\beta}$	Q-value of $0\nu\beta\beta$ (2039 keV)
$Q_{\beta\beta}^{160}$	200 keV energy window centered at $Q_{\beta\beta}$ (central 40 keV excluded for blinded analysis)
$T_{1/2}^{0\nu}$	Half-life of $0\nu\beta\beta$
$T_{1/2}^{2\nu}$	Half-life of $2\nu\beta\beta$
BEGe (detector)	Broad energy germanium detector
BI	Background index [cts/(keV·kg·yr) at $Q_{\beta\beta}$]
C.I.	Credible interval
DAQ (system)	Data acquisition system
FADC	Flash analog-to-digital converter
GERDA	Germanium detector array
HPGe (detector)	High purity germanium detector
LAr	Liquid argon
PMT	Photo-multiplier
PSA	Pulse shape analysis
PSD	Pulse shape discrimination
ROI	Region of interest for $0\nu\beta\beta$ at $Q_{\beta\beta}$

Chapter 1

Introduction

The neutrinoless double beta decay ($0\nu\beta\beta$) is a hypothetical lepton-number-violating nuclear transition predicted by several extensions of the Standard Model of particle physics. Its detection would prove the existence of new physics beyond the Standard Model and imply that neutrinos have a Majorana mass component. This introductory chapter is organized as follows. In Section 1.1 the physics of double beta decay transitions is reviewed, focusing on the implications of a positive $0\nu\beta\beta$ detection for the neutrino phenomenology. The experimental aspects of the $0\nu\beta\beta$ search are discussed in Section 1.2, along with a summary of the current limits on the process half-life and the goals of the new generation of experiments. In particular, the search of $0\nu\beta\beta$ in ^{76}Ge is discussed in Section 1.3 focusing on the concept and design of the GERDA experiment. Finally, the last section outlines the structure of this thesis and its contribution to the GERDA project.

1.1 Double beta decay and neutrino phenomenology

Double beta decays are second-order nuclear transitions consisting of the simultaneous decay of two neutrons into two protons. The transition preserves the atomic number (A) of the initial nucleus and changes the proton number (Z) by two units. The only final state allowed by the Standard Model of particle physics consists of two electrons and two anti-neutrinos besides the transformed nuclei:

$$(A, Z) \rightarrow (A, Z + 2) + 2e^- + 2\bar{\nu}_e \quad (1.1)$$

The transition providing this final state is called two-neutrino double beta decay ($2\nu\beta\beta$) and its leading channel is shown in Figure 1.1. It has been observed in several elements and the directly measured half-life is in the range $10^{19} - 10^{21}$ yr [1]. A second final state of the process in which no neutrinos are emitted can be considered:

$$(A, Z) \rightarrow (A, Z + 2) + 2e^- \quad (1.2)$$

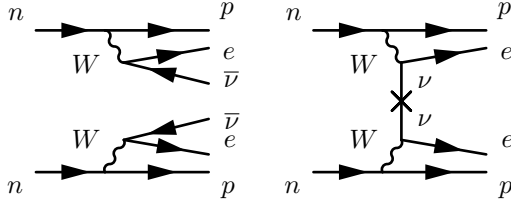


Figure 1.1: Diagram for $2\nu\beta\beta$ (left) and $0\nu\beta\beta$ mediated by the exchange of two light Majorana neutrinos (right).

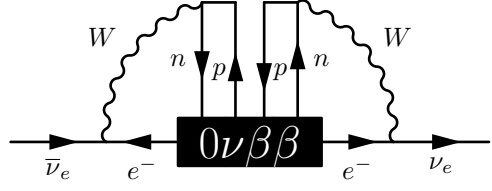


Figure 1.2: Diagram showing a $\bar{\nu}_e\text{-}\nu_e$ transition (i.e. a Majorana mass term for ν_e) realized by the $0\nu\beta\beta$ operator [5]. Adapted from Ref. [6].

In this case, the transition is called neutrinoless double beta decay ($0\nu\beta\beta$). The amount of leptons in the initial and final states differs now by two units. The experimental observation of $0\nu\beta\beta$ would hence establish that lepton number is not conserved, proving the existence of new physics beyond the Standard Model [2, 3]. The detection of $0\nu\beta\beta$ is presently a central research topic in fundamental physics. With the exception of one unconfirmed claim, it has not been reported and the current limits are in the range $10^{21} - 10^{25}$ yr [4].

$0\nu\beta\beta$ can be mediated by various mechanisms (see Ref. [2] for a recent review). The simplest channel is based on the exchange of light massive Majorana neutrinos¹ and its diagram is shown in Figure 1.1. Other channels involve right-handed weak currents, the exchange of super-symmetric particles, or other lepton-number-violating non-standard interactions. Independently of the mechanisms, each realization of $0\nu\beta\beta$ leads to a nonzero effective Majorana mass term through the diagram shown in Figure 1.2 (this argument is known as black-box or Schechter-Valle theorem [5]). A detection of the $0\nu\beta\beta$ -decay would hence establish unambiguously that neutrinos are massive Majorana particles. However, it should be noted that the 4-loop diagram of Figure 1.2 cannot account alone for the observed neutrino mass and other leading terms have to be present [6].

In general, different mechanisms can contribute to $0\nu\beta\beta$ at the same time and the half-life of the decay ($T_{1/2}^{0\nu}$) can be written as [2]:

$$\left(T_{1/2}^{0\nu}\right)^{-1} = \sum_x G_x(Q_{\beta\beta}, Z) |\mathcal{M}_x(A, Z) \eta_x|^2 \quad (1.3)$$

where x denotes the specific underlying process and η_x a function of its physical parameters, G_x indicates the phase space factor and \mathcal{M}_x the nuclear matrix element. While G_x is computable analytically, the computation of \mathcal{M}_x requires approximated methods and introduces significant systematics uncertainties. For instance, in the case of $0\nu\beta\beta$ mediated

¹A Majorana fermion is a fermion that corresponds to its own antiparticle. If neutrinos are Majorana particles, new terms can enter the Lagrangian. In particular, besides the usual Dirac mass term ($\mathcal{L}_D = -m_D \bar{\nu}_L \nu_R + h.c.$), we can introduce Majorana mass terms of the form: $\mathcal{L}_M = -m_R (\nu_R)^c \nu_R + h.c.$, where the $\nu_{L,R}$ indicate the left/right handed components of the neutrino fields and the superscript c the charged conjugate operator.

by the exchange of light Majorana neutrinos, the uncertainty is roughly a factor of two [4]. Considering this and the fact that $T_{1/2}^{0\nu}$ is not directly linked to the model parameters, in case of a detection the physical interpretation would not be trivial.

In the remaining part of the section, we will first summarize the physical parameters of the three-neutrino physics and then discuss their correlation with $0\nu\beta\beta$ under the assumption that the process is mediated by the exchange of light Majorana neutrinos. This interpretation is interesting because it requires only a minimal extension of the Standard Model, namely the Majorana nature of neutrinos and their nonzero mass which has been already proved by oscillation experiments. In addition, under this assumption, an observation of $0\nu\beta\beta$ would have profound implications on neutrino phenomenology, providing direct information about the neutrino mass ordering, the Majorana CP phases and the neutrino mass scale. The formalism used in the following is adapted from Refs. [2, 7].

In the last decade, experiments studying solar, atmospheric, reactor and accelerator neutrinos provided compelling evidences for neutrino oscillations caused by nonzero neutrino masses and neutrino flavor mixing [8]. This means that the neutrino flavor eigenstates (ν_e, ν_μ, ν_τ), which are coupled to the W boson and the charged leptons in the CC weak interactions, are superposition of three or more mass eigenstates (ν_i with $i = 1, 2, 3 \dots$) associated to nonzero mass eigenvalues (m_i):

$$|\nu_\alpha\rangle = \sum_i U_{\alpha i}^* |\nu_i\rangle \quad \text{with } \alpha = e, \mu, \tau \quad (1.4)$$

where U is the leptonic mixing matrix (PMNS matrix). Assuming the existence of only three mass eigenstates and that the mixing matrix is unitary, the PMNS matrix can be parametrized using three mixing angles ($\theta_{12}, \theta_{13}, \theta_{23}$) and three CP-violating phases (α, β and δ):

$$U = \begin{pmatrix} c_{12}c_{13} & s_{12}c_{13} & s_{13}e^{-i\delta} \\ -s_{12}c_{23} - c_{12}s_{23}s_{13}e^{i\delta} & c_{12}c_{23} - s_{12}s_{23}s_{13}e^{i\delta} & s_{23}c_{13} \\ s_{12}s_{23} - c_{12}c_{23}s_{13}e^{i\delta} & -c_{12}s_{23} - s_{12}c_{23}s_{13}e^{i\delta} & c_{23}c_{13} \end{pmatrix} \text{diag}\left(1, e^{i\alpha}, e^{i(\beta+\delta)}\right) \quad (1.5)$$

where $s_{ij} = \sin(\theta_{ij})$ and $c_{ij} = \cos(\theta_{ij})$. The phase δ is known as Dirac phase and it has physical consequences regardless of whether neutrinos are Dirac or Majorana particles. The phases α and β have a physical meaning only for Majorana neutrinos, otherwise they can be absorbed through redefinition of the other terms.

The phenomenology of neutrino physics is hence described by nine parameters (three mass eigenvalues, three mixing angles and three phases). The study of neutrino oscillations can provide information only about the angles, the Dirac phase and the mass-squared differences ($\Delta m_{ij}^2 = m_i^2 - m_j^2$). These parameters are connected to the probability that a

Table 1.1: Best fit values and 2σ allowed ranges of the oscillation observables. The values are taken from Ref. [12] and are the results of a global analysis of the results of neutrino oscillation experiments. The values are reported with respect to the normal (NH) and inverted (IH) hierarchy. Note that Δm_{32}^2 is defined herein as $m_3^2 - (m_1^2 + m_2^2)/2$. See also Ref. [13] for a second global analysis providing similar results.

Parameter	Hierarchy	Best fit	2σ range
Δm_{21}^2 [10^{-5} eV 2]	NH or IH	7.54	7.15 – 8.00
$ \Delta m_{32}^2 $ [10^{-3} eV 2]	NH	2.43	2.27 – 2.55
	IH	2.42	2.26 – 2.53
$\sin^2 \theta_{12}$	NH or IH	0.307	2.75 – 3.42
$\sin^2 \theta_{13}$	NH	0.0241	1.93 – 2.90
	IH	0.0244	1.94 – 2.91
$\sin^2 \theta_{23}$	NH	0.386	3.48 – 4.48
	IH	0.392	$3.53 - 4.84 \oplus 5.43 - 6.41$
δ	NH	1.08π	—
	IH	1.09π	—

neutrino changes flavor from α to β while propagating in vacuum through the equation:

$$\begin{aligned}
P(\nu_\alpha \rightarrow \nu_\beta) = & \delta_{\alpha\beta} - 4 \sum_{i>j} \text{Re} \{ U_{\alpha i}^* U_{\beta j}^* U_{\beta i} U_{\alpha j} \} \sin^2 \frac{\Delta m_{ij}^2 L}{4E} \\
& + 2 \sum_{i>j} \text{Im} \{ U_{\alpha i}^* U_{\beta j}^* U_{\beta i} U_{\alpha j} \} \sin \frac{\Delta m_{ij}^2 L}{2E}
\end{aligned} \tag{1.6}$$

where E is the neutrino energy and L the distanced covered. When the propagation occurs through matter (e.g. in the Sun, Earth or a supernova), the oscillation probability is affected by the coherent forward-scattering of neutrinos with the particle encountered along their path [9]. The amplitude of the process can be significantly modified (MSW effect) [10, 11], but it remains a function of the same neutrino parameters.

The spectrum of the neutrino mass eigenstates can take different forms. Given the data available, three mass hierarchies are considered:

- normal hierarchy (NH): $m_1 \ll m_2 \ll m_3$ with $m_2 \simeq \sqrt{\Delta m_{21}^2}$ and $m_3 \simeq \sqrt{\Delta m_{32}^2}$
- inverted hierarchy (IH): $m_3 \ll m_1 < m_2$ with $m_{1,2} \simeq \sqrt{\Delta m_{32}^2}$
- quasi-degenerate hierarchy (QD): $m_1 \simeq m_2 \simeq m_3 \gg \sqrt{\Delta m_{32}^2}$

The best fit values of the neutrino oscillation observables are reported in Table 1.1. The values of Δm_{21}^2 (including its sign) and θ_{21} have been measured with solar neutrinos (using the MSW effect) [8] and the long-baseline reactor experiment KamLAND [14]. The value of $|\Delta m_{32}^2|$ and $\sin^2 \theta_{23}$ have been instead estimated by atmospheric and long-baseline accelerator neutrino experiments [8]. The first measurement of $\sin^2 \theta_{13}$ has been

performed only recently (Summer 2012) by the reactor neutrino experiments: DOUBLE CHOOZ [15], Daya Bay [16] and RENO [17]. The sign of Δm_{32}^2 is currently unknown and its determination is a central and challenging research topic in elementary particle physics. Promising approaches are the study of MSW effects on atmospheric neutrinos using megaton-scale Cherenkov detectors with ~ 1 GeV energy threshold, PINGU [18], or magnetized detectors, INO [19]. Also a second generation of long-baseline accelerator neutrino experiments is under consideration, e.g. the European LAGUNA-LBNO [20] and US LBNE [21] projects.

The spectrum of neutrino mass eigenstates and the absolute mass scale are hence not accessible from neutrino oscillation processes. However they can be studied using complementary approaches which are sensitive to the so-called “neutrino absolute mass observables”. The approaches are: high-precision measurement of the beta-decay kinematics, cosmological observations and search for neutrinoless double beta decay. The first method aims at reconstructing the neutrino mass measuring the kinematics of electrons emitted from beta decays with high-precision [22]. The end point of the electron spectrum is affected directly by the rest mass of the neutrino emitted and the observable measured is:

$$\langle m_\beta \rangle \equiv \sqrt{\sum_i |U_{ei}|^2 m_i^2} = \sqrt{c_{12}^2 c_{13}^2 m_1^2 + s_{12}^2 c_{13}^2 m_2^2 + s_{13}^2 m_3^2} \quad (1.7)$$

The current limit of 2.1 eV (95% C.L.) has been set by the Mainz [23] and Troitsk [24] experiments. The limit will be improved by one order of magnitude in the next years by the KATRIN [25] experiment, which is being presently assembled. Cosmological and astrophysical observation are instead sensitive to the sum of the neutrino masses:

$$\Sigma \equiv \sum_i m_i \quad (1.8)$$

The present limits are of the order of eV and they will be improved at the level of few tenths of eV in early 2013, when the data of the ESA’s Planck mission will be released [26]. This approach however is dependent on the cosmological model considered. The third approach is the search of $0\nu\beta\beta$ and the measurement of its count rate. The process probability is a function of an observable called effective Majorana neutrino mass and defined as:

$$\langle m_{\beta\beta} \rangle \equiv \left| \sum_i U_{ei}^2 m_i \right| = |c_{12}^2 c_{13}^2 m_1 + s_{12}^2 c_{13}^2 m_2 e^{i2\alpha} + s_{13}^2 m_3 e^{i2\beta}| \quad (1.9)$$

Given the constraints on the mass squared differences and the mixing angles induced by oscillation experiments, the allowed range for $\langle m_{\beta\beta} \rangle$ is $(0.2 - 5.1)$ meV assuming the NH and $(9.2 - 61)$ meV (99% C.L.) assuming the IH [27]. The present limits are of the order of tenths of eV and the next generation of experiments will push the value by more than one

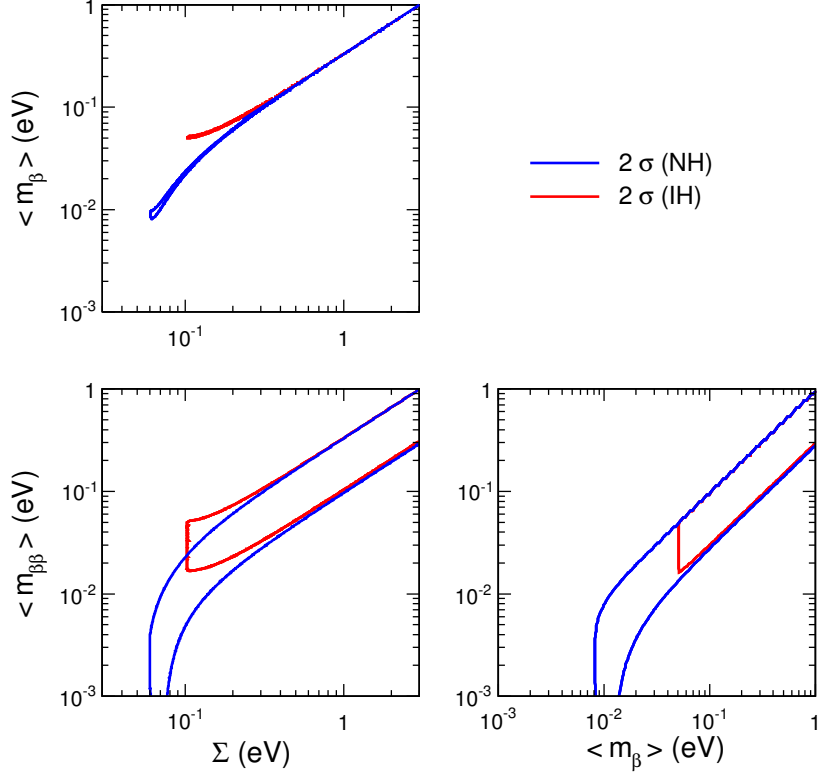


Figure 1.3: Correlation among the three absolute mass observables ($\langle m_\beta \rangle$, Σ , $\langle m_{\beta\beta} \rangle$) assuming the constraints induced by the oscillation data at 2σ level. The blue and red bands refer to the normal and inverted hierarchy, respectively. Taken from Ref. [12].

order of magnitude [4], exploring part of the parameter space allowed for the degenerated and inverted hierarchy.

The information encoded in the three absolute mass observables is complementary and highly correlated. Figure 1.3 shows the correlations between them assuming the best fit values for the oscillation parameters as reported in Table 1.1. Their combined measurement can set strong constraints for new flavor symmetry theories, always under the assumption that $0\nu\beta\beta$ is mediated by the channel shown in Figure 1.1.

It is important to remark that even small modifications to the model have strong implications on the interpretation and expectation of $0\nu\beta\beta$ results. An illustrative example is given by the current popular extensions to the three-massive neutrino model which take into account one or two additional light sterile neutrinos to explain the results of the LSND/MiniBooNE experiments and the reactor anomaly [28]. In this case, the effective Majorana mass would be composed of four/five terms and the upper bound of the allowed values increases. The plots in Figure 1.4 show the correlation between $\langle m_{\beta\beta} \rangle$ and the

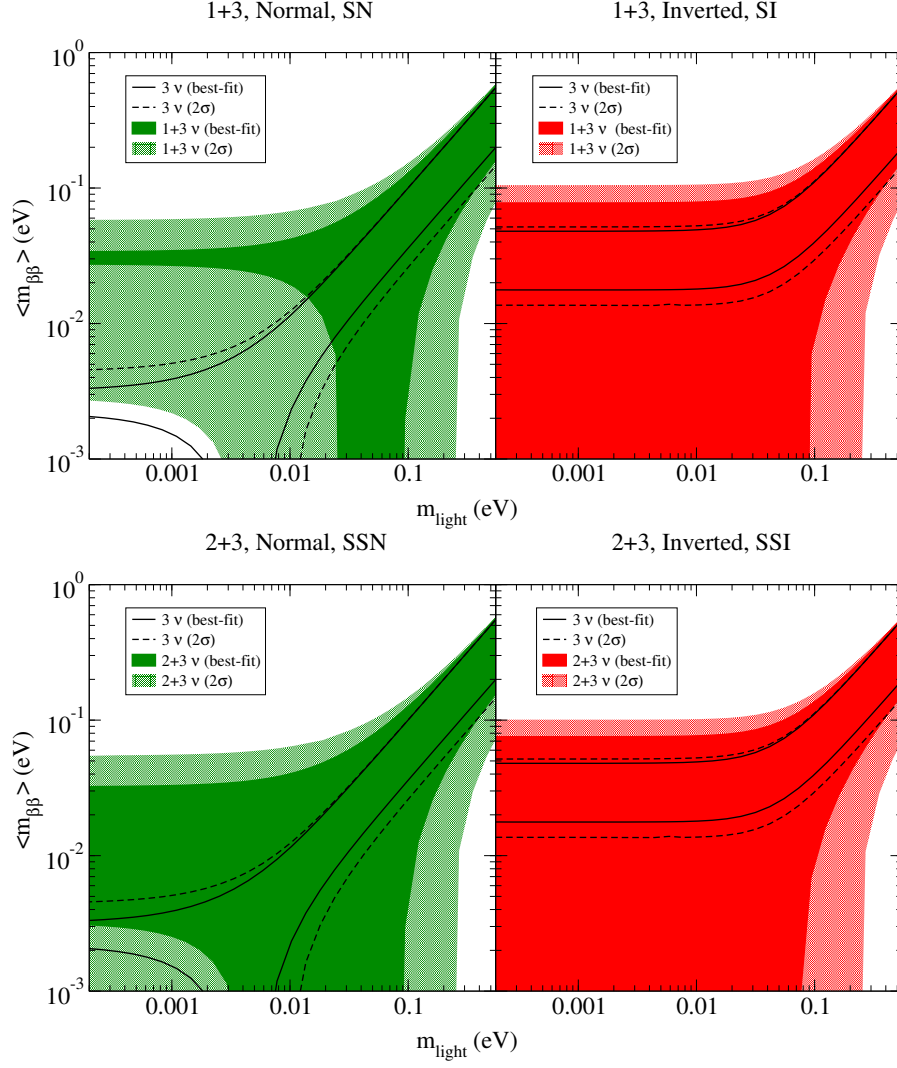


Figure 1.4: Effective Majorana mass against the smallest mass in the standard three light neutrino model and its extension considering additional one or two heavier sterile neutrinos (1+3 and 2+3 scheme). The constraints are given for the best fit of the oscillation parameter and the two sigma interval. Taken from Ref. [29].

lightest neutrino mass eigenvalue, m_{light} , for the different scenarios assuming the constraints induced by the oscillation data. Assuming the conventional three-neutrino model, the next generation of $0\nu\beta\beta$ experiments will be able to scrutinize only a fraction of the IH region while the NH space will not be accessible in the near future. Conversely, the existence of sterile neutrinos would reverse the situation. The effective Majorana mass can vanish in the IH for a large range of the lightest neutrino mass values. The next generation of experiments will access only a small part of it. However, the discovery power increases significantly for the NH, for which the parameter region would be widely probed.

1.2 Experimental aspects of the $0\nu\beta\beta$ search

The experimental signature of $0\nu\beta\beta$ is a peak in the distribution of the energy sum of two electrons at the Q-value of the decay ($Q_{\beta\beta}$). Typically only a few signal counts per year are expected over a continuum background distribution. The energy region around or close to $Q_{\beta\beta}$ containing the signal is called region of interest (ROI). Its width is determined by the energy resolution. The experimentally measured quantity is the half-life of the process ($T_{1/2}^{0\nu}$) and its sensitivity is given by the number of signal ($\lambda_{0\nu\beta\beta}$) and background (λ_{bkg}) events in the ROI. The expected value of $\lambda_{0\nu\beta\beta}$ in a time t is given by:

$$\lambda_{0\nu\beta\beta}(t) = \varepsilon \cdot N_{\beta\beta} \cdot (1 - e^{-t/\tau}) \stackrel{t \ll \tau}{\approx} \varepsilon \cdot N_{\beta\beta} \cdot t/\tau = \ln 2 \cdot \varepsilon \cdot N_{\beta\beta} \cdot \frac{t}{T_{1/2}^{0\nu}} \quad (1.10)$$

where $N_{\beta\beta}$ is the amount of $0\nu\beta\beta$ -decaying atoms, ε the detection efficiency, and $\tau = T_{1/2}^{0\nu}/(\ln 2)$ the mean lifetime of the process. The background rate in the ROI often scales to first approximation with the active detector mass M . In this case it is defined as background index (BI) and is given in units of $\text{cts}/(\text{keV} \cdot \text{kg} \cdot \text{yr})$. The number of background counts can thus be expressed as:

$$\lambda_{\text{bkg}}(t) = M \cdot \Delta E \cdot \text{BI} \cdot t \quad (1.11)$$

where ΔE is the width of the ROI.

If no signal is present and the experiment is background-free ($\lambda_{\text{bkg}} \ll 1$), the sensitivity on the half-life scales directly with $\lambda_{0\nu\beta\beta} \propto \varepsilon \cdot N_{\beta\beta} \cdot t$. In presence of background, the full statistical analysis is more complicated (see Ref. [30] for a complete discussion). An approximated solution can be given assuming that the statistical fluctuations on λ_{bkg} are Gaussian ($\sigma \propto \sqrt{\lambda_{\text{bkg}}}$) and that no signal is present. In this case, the sensitivity is given by:

$$\lambda_{0\nu\beta\beta} < \sqrt{\lambda_{\text{bkg}}} \quad \Rightarrow \quad T_{1/2}^{0\nu} > \frac{\ln 2 \cdot \varepsilon \cdot N_{\beta\beta} \cdot t}{\sqrt{M \cdot \Delta E \cdot \text{BI} \cdot t}} = \ln 2 \cdot \varepsilon \cdot N_{\beta\beta} \sqrt{\frac{t}{M \cdot \Delta E \cdot \text{BI}}} \quad (1.12)$$

To improve the half-life limits above $T_{1/2}^{0\nu} \sim 10^{25}$ yr several kilograms of material enriched in the $0\nu\beta\beta$ -decaying isotope (equivalent to $N_{\beta\beta} > 10^{25}$ atoms) have to be deployed for years in apparatus with $\text{BI} \lesssim 10^{-1}$ cts/(keV·kg·yr) and energy resolution $\lesssim 1\%$ at $Q_{\beta\beta}$. A common experimental approach to $0\nu\beta\beta$ detection is the use of detectors made of material enriched in a $0\nu\beta\beta$ -decaying isotope. In this particular case, the detection efficiency is maximized, $M \propto N_{\beta\beta}$ and, consequently, the sensitivity is proportional to $\sqrt{(M \cdot t)/(\Delta E \cdot \text{BI})}$. It should be emphasized that equation (1.12) is only illustrative. The new generation of experiments aims at reaching such a low background level in the ROI that its sensitivity would increase almost linearly with the exposure for a significant fraction of the data taking.

Historically, $0\nu\beta\beta$ decay experiments had to cope with three main classes of background sources. The natural radioactivity is typically the dominant one, in particular, the radioactive isotopes occurring in the decay chain of ^{238}U and ^{232}Th which are naturally present as contaminants in basically all materials. This includes alpha-, beta- and gamma-emitting isotopes and the Q-value of the decay is usually higher than $Q_{\beta\beta}$. Alpha-decays are also a source of neutrons through (α, n) reactions. The second component is due to cosmic rays, in particular muons, which induce signals both by direct interaction or production of secondary particle, namely neutrons and radioactive isotopes. Finally, an irreducible background is given by the $2\nu\beta\beta$ decays. This component can be critical because it generates events with the same topology of $0\nu\beta\beta$ and the sum energy distribution of the two output electrons extends up to $Q_{\beta\beta}$ (see Figure 1.5).

To overcome these backgrounds, the design of $0\nu\beta\beta$ experiments is usually based on a graded shielding concept with the decaying isotope in the inner highest pure region. The $0\nu\beta\beta$ source can be intrinsic to the detector material or dissolved in liquid scintillators (calorimetric experiments), or confined in thin foils placed among the detectors (tracking experiments). Extreme care is used in the selection and purification of the apparatus materials. The experiments are conducted deep underground to reduce cosmic-ray interactions and equipped with muon-veto systems. Finally, the detection technology must be able to distinguish $0\nu\beta\beta$ events from background while having a good energy resolution, which is the only way to mitigate the $2\nu\beta\beta$ background.

Various detection technology are pursued according to the choice of the source material. The candidate $0\nu\beta\beta$ isotopes are even-even nuclei (A, Z) that are more bound than their $(A, Z + 1)$ neighbor but less than the corresponding $(A, Z + 2)$ nuclei because of pairing forces (see Figure 1.6). For these isotopes, the single beta-decay is energetically forbidden and the transition can occur only via double beta decays. The candidate isotope is also required to have a large $Q_{\beta\beta}$ in order to place the region of interest above the end point of many potential background sources and to ensure a relatively fast $0\nu\beta\beta$ rate, which is proportional to the phase space factor $G_x(Q_{\beta\beta}, Z) \propto (Q_{\beta\beta})^5$ [3]. Additional requirements include the availability of an enrichment technique for a large scale production and the detection technologies deployable with the specific source material. The isotopes considered

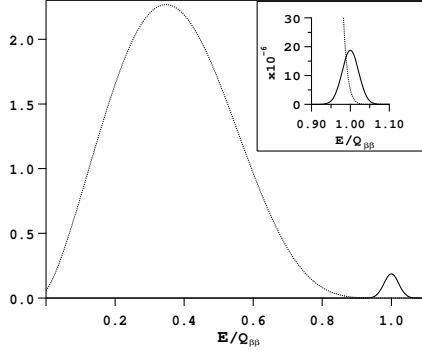


Figure 1.5: Distribution of the sum electron energies for $2\nu\beta\beta$ (dotted line, normalized to 1) and $0\nu\beta\beta$ (solid line, normalized to 10^{-2} and 10^{-6} in the figure inset) assuming 5% energy resolution [31]. The plot shows the importance of the energy resolution to resolve the two distributions.

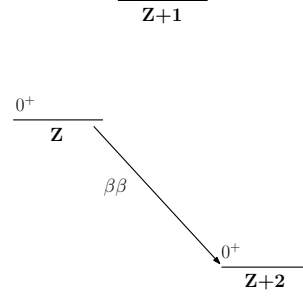


Figure 1.6: Energy level diagram of double beta decaying nuclei. Adapted from Ref. [3].

by the present or future experiments are summarized in Table 1.2 along with the detection techniques.

In the first decade of this millennium, the most sensitive results in $0\nu\beta\beta$ search have been given by the Heidelberg-Moscow (HdM) and the IGEX experiments using high purity Ge detectors enriched in ^{76}Ge . The two experiments set similar limits at $T_{1/2}^{0\nu}(^{76}\text{Ge}) \geq 1.9 \cdot 10^{25}$ yr and $T_{1/2}^{0\nu}(^{76}\text{Ge}) \geq 1.6 \cdot 10^{25}$ yr respectively (90% C.L.) [32, 33]. A subgroup of the HdM experiment claimed a positive observation at $T_{1/2}^{0\nu}(^{76}\text{Ge}) = 1.19^{+0.37}_{-0.23} \cdot 10^{25}$ yr [34] that has been criticized by part of the scientific community [27, 35, 36]. The best limits achieved in the past using other $0\nu\beta\beta$ isotopes were set by the Cuoricino (^{130}Te) and NEMO (^{82}Se , ^{100}Mo) experiments. Cuoricino operated at cryogenic temperature an array of 62 TeO_2 crystals (11.3 kg of ^{130}Te) as bolometers. The best limit reported by the collaboration is $T_{1/2}^{0\nu}(^{130}\text{Te}) > 2.8 \cdot 10^{24}$ yr (90% C.L.) [37]. NEMO is a tracking experiments in which thin foils of material enriched in $0\nu\beta\beta$ isotopes are placed inside drift chambers surrounded by calorimeters. The collaboration provided best limits for seven isotopes, the most stringent being $T_{1/2}^{0\nu}(^{82}\text{Se}) > 3.2 \cdot 10^{23}$ yr and $T_{1/2}^{0\nu}(^{100}\text{Mo}) > 1.0 \cdot 10^{24}$ yr (90% C.L.) [38].

Three new-generation experiments started the data taking in 2010/2011: GERDA, EXO and KamLAND-Zen. The GERDA experiment [39, 40] is designed to scrutinize the positive observation in ^{76}Ge using the same detection method of the previous experiments. If the claim is confirmed, GERDA will perform a precise measurement of the process half-life. Otherwise it will improve the present limit by an order of magnitude. The EXO and KamLAND-Zen experiment use ^{136}Xe as target material. Both of them have already improved the previous experimental limits on its half-life. EXO is a time projection chamber

Table 1.2: Summary of the $0\nu\beta\beta$ isotopes, $Q_{\beta\beta}$, natural abundances, detection techniques and a selection of the experiments in which they are studied. Adapted from Refs. [2, 3]. The experiments marked with a star have been already completed.

Isotopes	$Q_{\beta\beta}$ [keV]	abund. [%]	Detection technique	experiments
^{48}Ca	4274	0.19	CaF_2 scintillation crystals	CANDLES
^{76}Ge	2039	7.8	High purity $^{\text{enr}}\text{Ge}$ detectors	GERDA, Majorana
^{82}Se	2995	9.2	Thin ^{82}Se foils and tracking	SuperNEMO
			Scintillating bolometers	Lucifer
^{100}Mo	3035	9.6	Thin ^{100}Mo foils and tracking	NEMO3 *
			Scintillating bolometers	LUMINEU
^{116}Cd	2809	7.6	CdZnTe semiconductor detectors	COBRA
^{130}Te	2530	34.5	TeO_2 bolometers	CUORICINO *
				CUORE
^{136}Xe	2462	8.9	Xe-loaded organic liquid scintillator	KamLAND-Zen
			Liquid Xe time projection chamber	EXO
			Gas Xe time projection chamber	NEXT
^{150}Nd	3367	5.6	Nd-loaded organic liquid scintillator	SNO+
			Magnetic tracking detectors	DCBA/MTD

(TPC) designed to measure both the scintillation of liquid Xe and its ionization signal [41]. The experiment operates roughly 80 kg of ^{136}Xe and has an energy resolution at $Q_{\beta\beta}$ of about 5% (full width half maximum). The best limit published by the collaboration is $T_{1/2}^{0\nu}(^{136}\text{Xe}) > 1.6 \cdot 10^{25} \text{ yr}$ (90% C.L.) [42]. KamLAND-Zen operates ~ 13 tons of Xe-loaded organic liquid scintillator (~ 290 kg of ^{136}Xe) surrounded by 1 kton of liquid scintillator inside the KamLAND detector [43, 44]. The relatively poor energy resolution ($\sim 10\%$ full width half maximum) at $Q_{\beta\beta}$ is balanced by the large mass of target material and low background level. KamLAND-Zen published a limit at $T_{1/2}^{0\nu}(^{136}\text{Xe}) > 5.7 \cdot 10^{24} \text{ yr}$ at 90% C.L. [44] and recently reported improved results [45]. The results of the ^{136}Xe -based experiments are in tension with the claim for a positive observation in ^{76}Ge [34]. In the next years, KamLAND-Zen, EXO and GERDA should independently reach the sensitivity to scrutinize such a claim.

1.3 The search of $0\nu\beta\beta$ decay in ^{76}Ge and the GERDA experiment

The advantages of using high purity Ge (HPGe) detectors for the neutrinoless double beta decay search have been recognized early [46] and, until today, the most stringent experimental limits on $0\nu\beta\beta$ were achieved with this detection technique. Germanium detectors can be

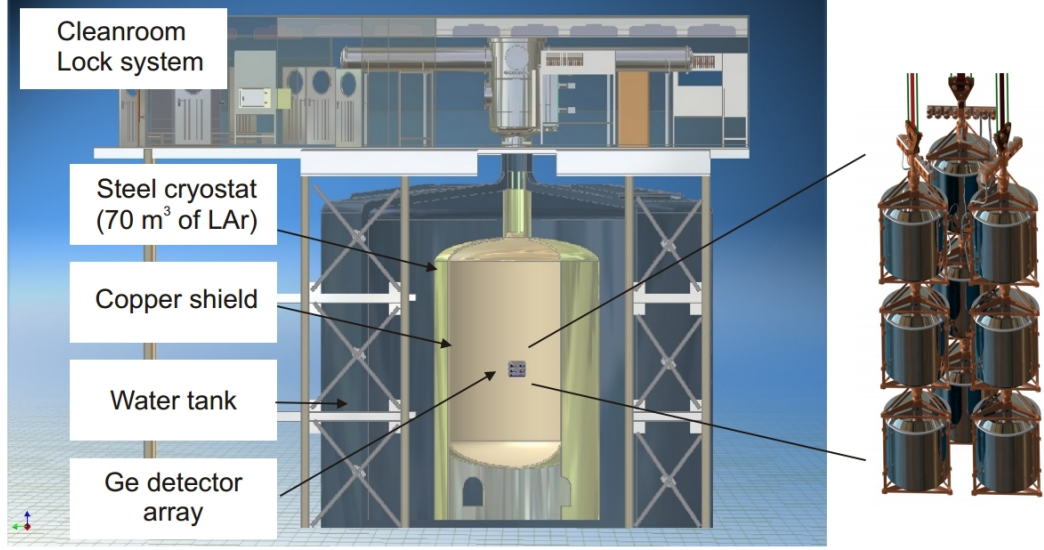


Figure 1.7: (Left) Artist's view of the GERDA setup and (right) of the detector strings. Taken from Ref. [48].

produced from germanium material enriched in ^{76}Ge (typically 87% enrichment). Their main advantages for $0\nu\beta\beta$ search are the intrinsic radio-purity, the excellent spectroscopic performance (0.1% resolution at $Q_{\beta\beta}$) and the high detection efficiency, achievable using the source material as detector medium. In addition, HPGe detectors are a well consolidated technology commonly used for gamma-ray spectroscopy, which proved to be reliable and suitable for long-term experiments. Disadvantages are the relatively low $Q_{\beta\beta}$ (2039 keV), which is lower than some ^{208}Tl and ^{214}Bi gamma-lines, and the challenges to increase the target mass in comparison to experiments using liquids or gases as $0\nu\beta\beta$ sources.

HPGe detectors are typically operated in a vacuum cryostat at cryogenic temperatures. The IGEX and HdM collaborations pursued this standard approach basing their experimental design on ultra-low background cryostats and lead shielding. Both experiments succeeded in reaching a background index of the order of 10^{-1} cts/(keV·kg·yr), while facing contaminations of U and Th daughters in the cryostat material surrounding the detectors as limiting background sources. The new generation of ^{76}Ge experiments is designed to reduce the background by two orders of magnitude. The MAJORANA [47] collaboration will use improved ultra-low background cryostats fabricated with copper electroformed deep-underground in the experimental site. The GERDA collaboration, instead, uses an innovative design approach in which an array of bare HPGe detectors is operated directly in ultra radio-pure liquid argon (LAr), which acts as coolant material, passive shielding against the external radioactivity and active veto-system when its scintillation light is detected.

An artist's view of the GERDA experimental setup is shown in Figure 1.7. The cryogenic

liquid is surrounded by an additional thick layer of ultra-pure water, which is effective in shielding external neutrons and gamma-rays. The water volume is instrumented with photo-multipliers and is operated as a Cherenkov detector to reject events due to high-energy muons. The Ge detectors are mounted in strings and lowered into the LAr using a lock system located on top of the water tank inside a clean room. The experiment is located in the underground national laboratories of Gran Sasso, LNGS/INFN, in Italy (3800 m.w.e.).

The project pursues a staged implementation. In GERDA Phase I, started in November 2011, eight enriched coaxial detectors (~ 15 kg of ^{76}Ge) are deployed aiming at scrutinizing the previously mentioned claim of evidence in about one year of data taking (exposure of 20 kg·yr) and a background index of 10^{-2} cts/(keV·kg·yr). These detectors were originally used in the IGEX and HdM experiment and have been refurbished before the deployment in LAr. In GERDA Phase II, about 30 new custom-made enriched BEGe detectors [49] with a small read-out electrode will be installed (additional 20 kg of ^{76}Ge). The enhanced pulse shape discrimination capabilities featured by BEGe detectors in combination with the detection of the liquid argon scintillation light are expected to reduce the background index below 10^{-3} cts/(keV·kg·yr), allowing to explore half-lives $> 10^{26}$ yr with 100 kg·yr of exposure. Depending on the results of the first two phases, a third phase, in common with the MAJORANA collaboration, is conceived to probe half-lives $> 10^{27}$ yr. To explore this parameter regime, an exposure of several 1000 kg·yr and backgrounds $< 10^{-4}$ cts/(keV·kg·yr) are required.

1.4 Outline of the dissertation

This dissertation is divided into two parts. The first one deals with the processing and analysis of GERDA Phase I data. It contains a detailed description of the data treatment including the digital signal processing, the data selection and the calibration procedure (Chapter 2). In addition, it presents a spectral study of the GERDA background and a quantitative analysis of its components at $Q_{\beta\beta}$ (Chapter 3). The second part focuses on the design and development of custom-made Phase II detectors and the study of background rejection techniques. A brief overview of the detector R&D is given in Chapter 4. In Chapter 5, a comprehensive modeling of the detector response to charged particle or gamma-ray interactions inside the Ge crystal is presented along with its validation against experimental data. The modeling is used to understand the charge collection and signal formation of these new detectors and it is applied in Chapter 6 to study the signals induced by decays occurring inside the detector ($0\nu\beta\beta$ and cosmogenic isotopes). In Chapter 6, the possibility of rejecting surface events with the Phase II detectors is also discussed. Finally, Chapter 7 summarizes the background level expected in GERDA Phase II and the achievable limits on the $0\nu\beta\beta$ half-life.

GERDA Phase I: data processing and background analysis

Chapter 2

Data processing and spectral analysis

This chapter presents the reference processing and analysis of the GERDA data taken in the first six months of Phase I, from November 9, 2011, to May 22, 2012. These results have been published by the collaboration in Refs. [50, 51]. The off-line data treatment has been defined in the context of this thesis work along with the software framework and the algorithms used to perform it [52, 53]. The daily processing of the data has been carried out by the GERDA Analysis team (coordinated by L. Pandola). In the following, we report only the details relevant for the data interpretation and we refer to Appendix A for the full description of the data handling and framework design, and to Appendix B for a summary of the digital filters. After discussing the quality cuts and the calibration procedure, we will describe the main background components inferable from the considered data set by spectral analysis.

2.1 Detector array configuration and signal read-out

The HPGe detector array deployed during this first part of GERDA Phase I contains eleven coaxial detectors, three produced from natural Ge material ($^{\text{nat}}\text{Ge}$) and eight from material enriched in ^{76}Ge ($^{\text{enr}}\text{Ge}$). All the detector crystals have been originally fabricated by ORTEC and previously operated in the Heidelberg-Moscow, IGEX, and GENIUS-TF [54] experiments. Before their operation in GERDA, the detectors have been completely refurbished at Canberra Olen, changing the electrode geometries and using surface treatments optimized for operations in liquid argon [48, 55]. The current detector dimensions, masses and operational parameters are summarized in Table 2.1. Two enriched detectors, ANG1 and RG3, showed unstable performance (high leakage current) early after the deployment and they will not be considered in the following. The total detector mass for physics analysis is hence 14.6 kg of $^{\text{enr}}\text{Ge}$ and 7.6 kg of $^{\text{nat}}\text{Ge}$.

Table 2.1: Features and operational parameters of the detectors deployed in the GERDA array during the first part of the Phase I. The values are taken from Refs. [50, 48]. The total mass is 17.7 kg for the enriched detectors and 7.6 kg for the natural ones.

detector name	total mass [kg]	^{76}Ge fraction [%]	detector diameter/length [mm]	bore hole diameter/length [mm]	string position	bias voltage [kV]
ANG1	0.958	86 (1)	58.5 / 68	13.5 / 51	2 bottom	4.0
ANG2	2.833	87 (2)	80 / 107	14 / 94	2 middle	3.5
ANG3	2.391	88 (3)	78 / 93	15 / 83	4 top	3.5
ANG4	2.372	86 (1)	75 / 100	14 / 89	3 middle	3.5
ANG5	2.746	86 (1)	78.5 / 105	12.5 / 94	4 middle	2.5
RG1	2.110	85 (1)	77.5 / 84	13.5 / 73	3 top	4.5
RG2	2.166	85 (1)	77.5 / 84	13 / 72	3 bottom	4.0
RG3	2.087	85 (1)	79 / 81	13 / 71	4 bottom	3.3
GTF32	2.321	7.8 (1)	89 / 71	12 / 41.5	1 middle	3.0
GTF45	2.312	7.8 (1)	87 / 75	11.5 / 43	1 top	3.0
GTF112	2.965	7.8 (1)	85 / 100	11.5 / 63	2 top	3.0

The detectors are mounted into four strings (see Table 2.1). The three strings containing the enriched detectors are enclosed in a $60\,\mu\text{m}$ cylindrical Cu foil (mini-shroud) as shown in Figure 2.1. The mini-shroud was not present in the original design of the experiment. It has been introduced during the commissioning phase to mitigate an unexpected high background induced by ^{42}K . This isotope is created directly in the liquid argon by the decay of ^{42}Ar ($T_{1/2} = 32.9\text{ yr}$), a cosmogenic-activated isotope of Ar. Its count rate showed a correlation with the electric field generated by the detector array in the liquid argon volume. The mini-shroud has been deployed to separate electrically and physically the inner and outer volume. It is presently operated grounded. This configuration – in which the outer volume is field free – has been found to minimize the ^{42}K background.

The GERDA Phase I detectors are p-type HPGe coaxial detectors. The Ge crystal has a cylindrical shape with a bore hole on one of the flat surfaces as shown in Figure 2.2. The n+ electrode is created on the detector outer surface by Li-diffusion. The read-out p+ electrode is realized by B-implantation on the bore hole surface and it is divided by the n+ electrode with a circular groove. The semiconductor junction is hence located between the Li-diffused layer and the p-type Ge material. The detectors are operated by applying high voltage to the n+ electrode (3-4 kV, see Table 2.1) and grounding the read-out electrode¹.

In this configuration the junction is reverse biased and the detector volume fully depleted. The electric field created by the electrode potential difference is thus able to efficiently collect

¹The string containing only natural detectors (string 1, operated without mini-shroud) has been used to test an alternative read-out scheme (AC coupled). Using this read-out mode, negative high-voltage can be applied to the read-out electrode keeping the outer surface of the detector (n+ electrode) grounded. Similarly to the mini-shroud, this electrode scheme prevents the formation of electric field in the liquid argon volume.

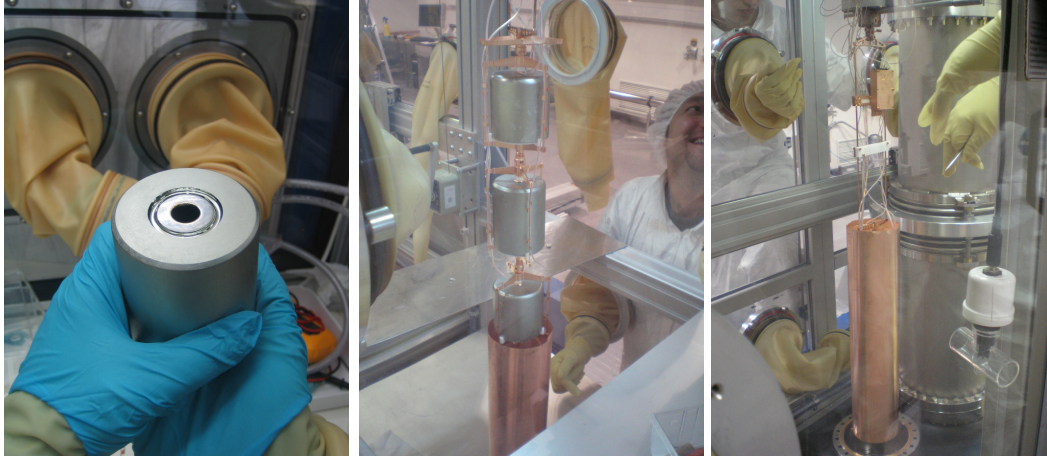


Figure 2.1: (Left) One of the enriched coaxial detectors used in GERDA Phase I after the refurbishment at Canberra Olen. The outer Li-diffused surface is separated by the B-implanted p+ electrode (extending inside the bore-hole) by a circular groove. (Center) The detectors are mounted upside down in low-mass holders and assembled in strings. Each detector string is inserted into a thin Cu cylinder (mini-shroud) designed to screen the electric field generated by the detector bias voltage and to prevent flows in the liquid argon volume around the detectors. (Right) After assembling, the strings are lowered into the cryostat. The Cu box visible on the top of the string is used to enclose the front-end electronics.

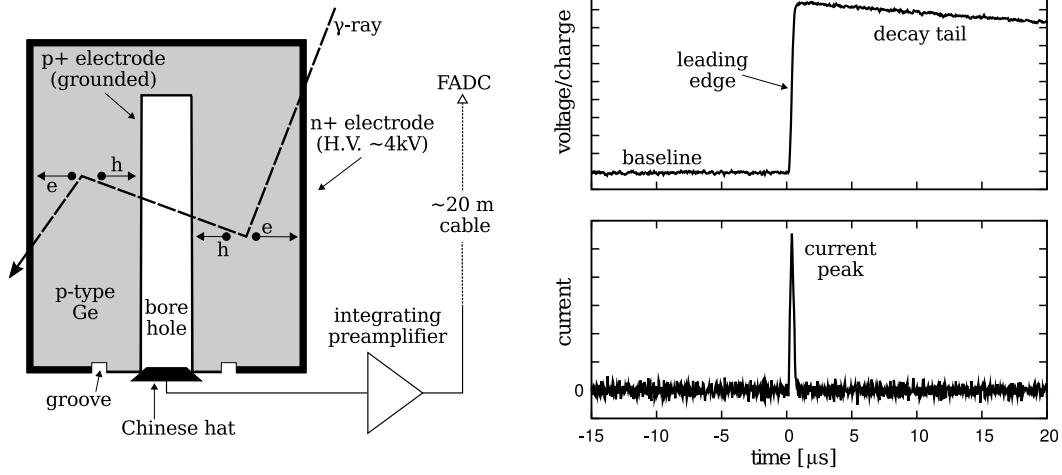


Figure 2.2: (Left) Vertical section of an enriched coaxial detector used in GERDA Phase I showing the electrode scheme and the read-out chain. (Right) Traces containing a characteristic pulse induced by the collection of electron-hole pairs ionized through interactions of gamma-rays or charged particles with the Ge material.

charges generated by interactions of radiation or charged particles with the Ge material. The drift of electron or hole clusters toward the detector electrodes induces a voltage signal on the read-out electrode. The maximum amplitude of the signal is proportional to the total number of electron-hole pairs generated and its time-structure contains information concerning the topology of the interaction sites and the energy released in each of them.

The detectors read-out is performed with custom-made charge sensitive pre-amplifiers [56], realized with low-background components and designed to operate in cryogenic environment. The front-end electronics is placed 30 cm above the top detector of the string (see Figure 2.1, picture on the right), to lower the background count rate induced by the electronic component below the experimental requirements and provide a sufficiently good signal-to-noise ratio. The signals are hence transmitted over 10 m thin coaxial cables outside the cryostat (Habia SM50, $50\ \Omega$) and then over additional ~ 10 m of coaxial cables (RG178) to a linear amplifier. The output of the amplifier is digitized by 14-bit flash-ADCs (FADC), running at 100 MHz sampling frequency and equipped with integrated anti-aliasing bandwidth filters [57, 58, 59]. The FADC traces are finally saved to disk for off-line analysis.

The signals recorded by the FADC are charge pulses composed of a $\sim 1\ \mu\text{s}$ -long rising part (leading edge), produced during the charge collection inside the detector, and an exponential decay tail ($\sim 100\ \mu\text{s}$ decay time) folded in by the charge-sensitive preamplifier. A typical charge pulse is shown in Figure 2.2. The plot shows also the first derivative of the charge pulse which corresponds to the current signal at the input of the FADC. The two signals will be frequently reported together in this thesis since they emphasize different information related to the charge collection inside the detector. The raw data stored by the FADC contain for each event and channel two traces centered on the pulse leading edge. The first trace is sampled at 100 MHz and is $4\ \mu\text{s}$ long (high-frequency-short trace). The second one is sampled at 25 MHz and is $160\ \mu\text{s}$ long (low-frequency-long trace).

2.2 Data processing

The data processing is composed of three main steps. In the first one (discussed in Section 2.2.1) the traces of the FADC are analyzed to obtain information concerning the physical event, e.g. the maximum amplitude of the signal which is proportional to the energy deposited in the detector active volume. The resolution achievable on a particular pulse parameter is usually limited by the electronic noise superimposed to the detector signal. The implementation and tuning of the trace analysis algorithms (digital filters) is hence a critical issue. In addition, these parameters are used in the second step of the data processing (see Section 2.2.2) to identify signals due to non-physical events or particular types of traces (e.g. given by the superposition of multiple physical events). The last step of the processing is the calibration of the energy scale and resolution. The procedure is described in Section 2.2.3 together with the overall performance of the detectors and the

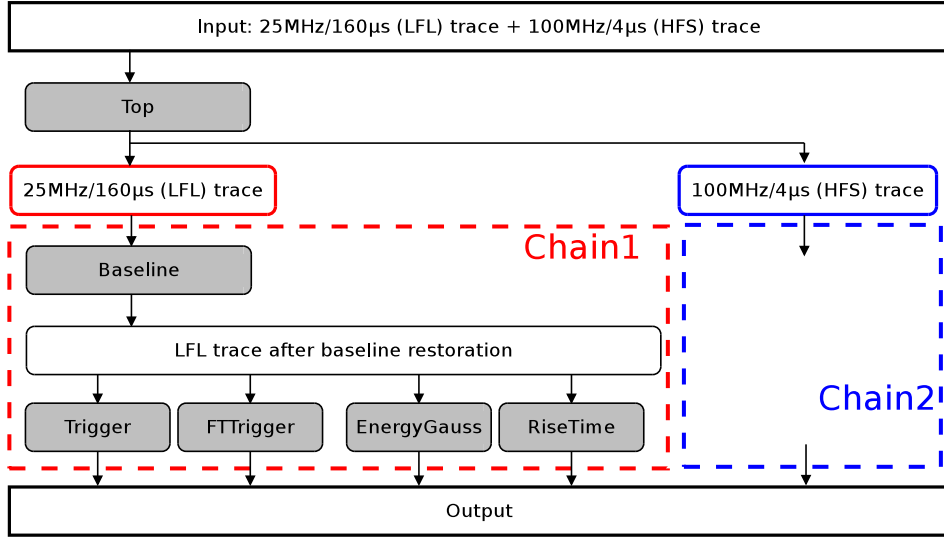


Figure 2.3: Flow chart of the signal processing. The two traces saved by the digitizer are processed along two different chains of analysis modules. The low-frequency-long (LFL) trace is used for reconstructing the energy, the trigger and the rise time. The high-frequency-short (HFS) trace is used to analyze the time-structure of the signals.

signal read-out chain in the considered data set. All the three steps are performed within the GERDA data analysis framework (GELATIO) which is described in Appendix A.

2.2.1 Off-line digital signal processing

The digital signal processing of the GERDA data is organized into chains of modules. The modules and the interface to define the chains are provided by the GELATIO software. Each module is used for a unique and consistent task of the signal processing and contains a sequence of elementary digital filters designed to extract from a trace the information of interest. The output of a module can contain scalar parameters (e.g. the amplitude of the pulse or the average baseline value) as well as new traces obtained applying shaping filters (smoothing, deconvolution, etc.). This information can be used as input for the following modules of the chain. The parameters of the digital filters and the chains of modules can be customized for each channel according to the detector features.

The modular structure of the analysis is shown in Figure 2.3. A first module, *TopModule*, is used to extract from the input file the traces required in the analysis according to the event list and the active channels. It also performs preprocessing operations, e.g. checking, and possibly changing, the pulse polarity (conventionally all the modules work with positive-polarity pulses). The traces retrieved are then processed along two different chains. The high-frequency-short trace is processed along a chain tailored to study the time-structure

of the pulse leading edge. It is highly customized according to the analysis goals and the detector features. Concrete examples are discussed in the following chapters dealing with pulse shape analysis. The low-frequency-long trace is instead used when a high time resolution is not needed or to analyze the signal baseline and the pulse decay tail (e.g. energy reconstruction). The relative module chain provides the parameters which are used for data selection, quality monitoring and spectral analysis. Its modules are summarized in the following.

BaselineModule (baseline analysis and restoration). The module analyzes the baseline of the signal computing the average value, the root-mean-square deviation (RMS) and the linear slope before the leading edge. In addition, it performs a baseline restoration – a subtraction of the average baseline value to the trace – and provides the new signal to the other modules.

TriggerModule and *FTTriggerModule* (localization of the leading edges). *TriggerModule* is tuned to identify the beginning of the pulse leading edge (trigger position) with high precision and stability. It implements a leading-edge discriminator with threshold defined dynamically as three times the RMS of the signal baseline. After the trigger, the signal has to remain above threshold for at least $40\ \mu\text{s}$, otherwise the trigger is rejected. *FTTriggerModule* is instead used to identify events with multiple physical pulses occurring within the same trace. The signal is differentiated and then integrated for noise reduction ($1.5\ \mu\text{s}$ moving differentiation filter and $1\ \mu\text{s}$ moving average filter). The signal shaping is shown in Figure 2.4. The resulting trace has a peak for each sharp variation of the signal (such as the leading edge of a pulse). The peak width is about the size of the moving differentiation. Its value has been chosen to maximize the pile-up identification efficiency and avoid the misidentification of single physical events. The number and the position of the peaks are estimated by applying a leading-edge discriminator, whose threshold is four times the RMS of the baseline. After this condition is met, the signal has to remain above the threshold for at least $1\ \mu\text{s}$.

EnergyGaussModule (energy reconstruction). The amplitude of the signal is extracted with an approximate Gaussian filter [60]. The pulse is differentiated by a moving differentiation filter and then integrated ~ 20 times by a moving average filter to achieve an approximated Gaussian shape. The energy information is eventually stored in the maximum amplitude of the quasi-Gaussian pulse. The width of the moving filters has been set to $5\ \mu\text{s}$, sufficient to avoid losses due to ballistic effects. The intermediate steps of the shaping are shown in Figure 2.5. Historically, the energy reconstruction filters for gamma-ray spectroscopy includes also a deconvolution of the exponential function which is folded in the signal by the charge sensitive preamplifier. However, our algorithm proved to give better results than the usual filters when applied to the GERDA data and to reach the performance of a spectroscopy amplifier [61].

RiseTimeModule (computation of the leading-edge width). The module computes the rise time between 10% and 90% of the maximum amplitude of the pulse. The maximum

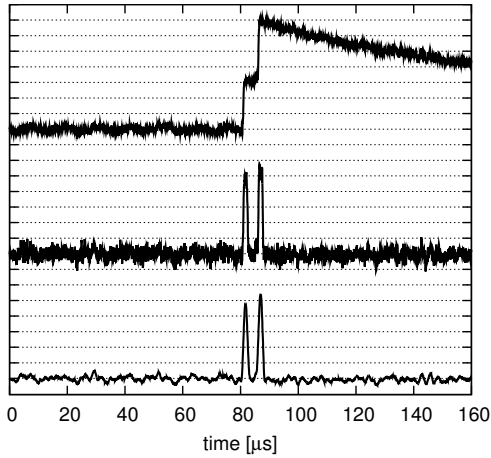


Figure 2.4: Digital signal processing performed by *FTTriggerModule*. The incoming trace (top trace) is differentiated (middle trace) and integrated (bottom). The output trace has a peak for each pulse in the incoming trace. The illustrative input trace contains two physical pulses with leading edge shifted by $\sim 5 \mu\text{s}$.

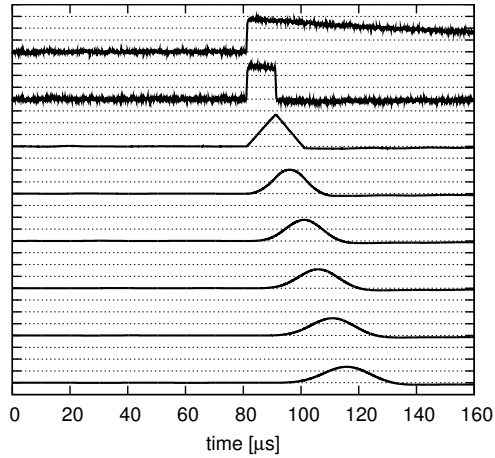


Figure 2.5: Digital signal processing performed by *EnergyGaussModule*. The incoming signal (top trace) is differentiated (second trace) and then integrated several times (following traces) by a moving average filter. The output signal has a Gaussian shape and its maximum is proportional to the event energy.

amplitude is computed as the difference between the maximum of the pulse and the average baseline value. Then, the first samples below the 10% and 90% of the maximum amplitude are found by moving backwards from the position of the maximum.

2.2.2 Signal quality monitoring

The signals that have to be identified and removed from the data set can be divided into two classes: *a)* signals corrupted or produced by non-physical events, i.e. discharges, cross-talk, pick-up noise; *b)* signals which are not properly processed along the analysis pipeline, as pile-ups and accidental coincidences.

The signals in the first class are characterized by anomalous decay tails, leading edges with positions and widths not consistent with well-behaved pulses, or over/under shots. Illustrative non-physical signals are shown in Figure 2.6. The rejection of these events is performed with a sequence of four cuts. The first one is applied on the distribution of the time position of the leading edge (*TriggerModule*) and of the maximum amplitude of the Gaussian pulse (*EnergyGaussModule*). The values of these parameters are in well-defined ranges if the trace contains a proper pulse, with the leading edge at the correct position and followed by an exponential decay tail. The third cut is applied on the distribution of the signal 10-90% rise time (*RiseTimeModule*) and removes pulses inconsistent with the

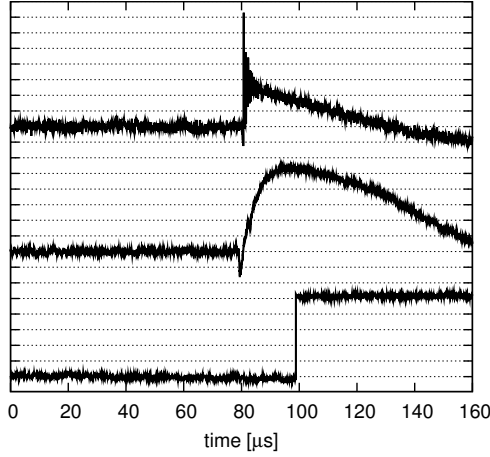


Figure 2.6: Illustrative traces generated by non-physical events. Note that these pulses do not have the typical exponential decay tail after the leading edge.

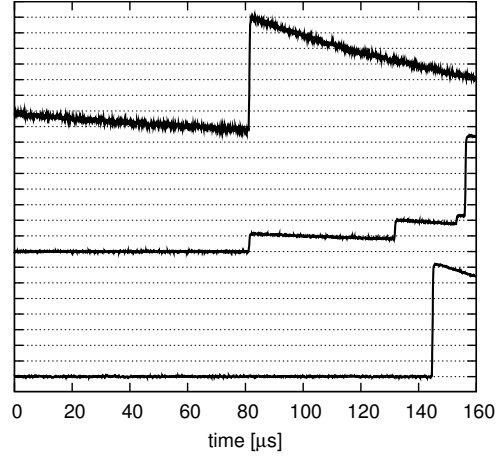


Figure 2.7: Example of traces generated by pile-up events (top-middle trace) and accidental coincidences (bottom).

detector charge collection time. The fourth cut is performed on the maximum value of the trace samples and removes events in which the dynamic range of the FADC is exceeded.

The second class of traces includes signals generated by the superposition of multiple physical pulses, or having the leading edge not aligned with the center of the trace (see Figure 2.7). These events are identified applying a cut on the distribution of the baseline slope (*BaselineModule*), the number of triggers (*FTTriggerModule*) and the position of the main leading edge (*TriggerModule*). The fraction of these traces is proportional to the event rate and can reach up to 15% in the calibration data sets (rate $\gtrsim 10^2$ events/s with 500 keV energy threshold), while it is usually negligible in the physics data sets (rate $\lesssim 10^{-2}$ events/s with ~ 30 keV energy threshold). The identification of this second class of events is of primary importance for GERDA since the background rejection techniques based on the analysis of the signal time-structure are developed and tuned by using calibration data. Therefore the calibration data have to be filtered to extract samples of events as similar as possible to the physics run data and a small inefficiency could bias the following analysis. The pile-up rejection filters have been tuned to reject $\sim 100\%$ of the traces in which the secondary event induces an increase of the signal amplitude larger than 20 keV and the time difference with the main trigger is $\geq 2 \mu\text{s}$ [61].

Besides cuts for removing non-physical signals or pile-up events, several parameters are constantly monitored to check the quality of the data taking and the stability of the setup [62]. In particular, since the baseline is proportional to the detector leakage current, its average value and RMS (*BaselineModule*) are parameters sensitive to variations of the noise and the gain of the read-out chain. Figure 2.8 shows the value of these parameters as

a function of time for a 10 day run. The parameters are stable for most of the data taking and strong fluctuations (as the ones occurring during day 7) indicate hardware operations in the setup or sudden temperature variations. Given the amplitude of the fluctuations (several sigma from the central value), the corresponding data can be removed by reducing the duty cycle but without affecting the live time of the remaining part of the data set.

2.2.3 Calibration

The energy scale and resolution of the HPGe detectors in GERDA is regularly measured performing dedicated calibration runs with ^{228}Th sources (every one or two weeks). The calibration is performed using six prominent gamma-lines of ^{228}Th at the energy of 583, 727, 861, 1620, 2104 and 2615 keV. An example of calibration spectrum is shown in Figure 2.9. The gamma-line peaks are fitted with a Gaussian function, for the signal, sitting over a sigmoid function accounting for the background:

$$f(x) = \frac{A}{\sqrt{2\pi}\sigma} \exp\left[-\frac{(x-\bar{x})^2}{2\sigma^2}\right] + (B_L - B_R) \left[\exp\left(\frac{x-\bar{x}}{2\sigma}\right) + 1 \right]^{-1} + B_R \quad (2.1)$$

where \bar{x} is the centroid of the peak, A the net area and σ the spread. The parameters B_L and B_R indicate the background rate on the left and right side of the peak. The fit performed on the 2615 keV gamma-line is shown in the bottom panels of Figure 2.9, along with the background model. The fit is performed after applying the quality cuts discussed in the previous section. Because of the high count rate during the calibration run, the data contain a large fraction of pile-up events (up to 15%). This contamination is relevant also at the gamma-line energies (up to 10%) where it creates a characteristic tail on the left side of the peaks. The application of the quality cuts does not affect significantly the estimation of the peak centroid but it usually improves remarkably the goodness of the fit. The agreement between the data and the fitting function confirms that the gamma-line signal distribution can be modeled with a Gaussian distribution and it is a strong indication that the energy reconstruction algorithm discussed in the previous section is unbiased.

The energy calibration curves are extracted from the estimated centroid of the gamma-line peaks. The points are fitted using a second order polynomial function ($f(x) = a + bx + cx^2$, with a, b, c scalar parameters). The fit results for a typical calibration run are shown in Figure 2.10. The data point are to first approximation distributed along a linear function and the deviation from linearity is lower than 0.1%. However, the residuals with respect to the linear component of the fitting function (fixing $c = 0$ during the fit) show a clear parabolic distribution which is corrected by the reference quadratic function. This nonlinearity is probably related to the read-out electronic chain or the data acquisition system. The maximum spread of the residuals from the best fit is usually below 1 keV in all the detectors, within the requirements of the experiment.

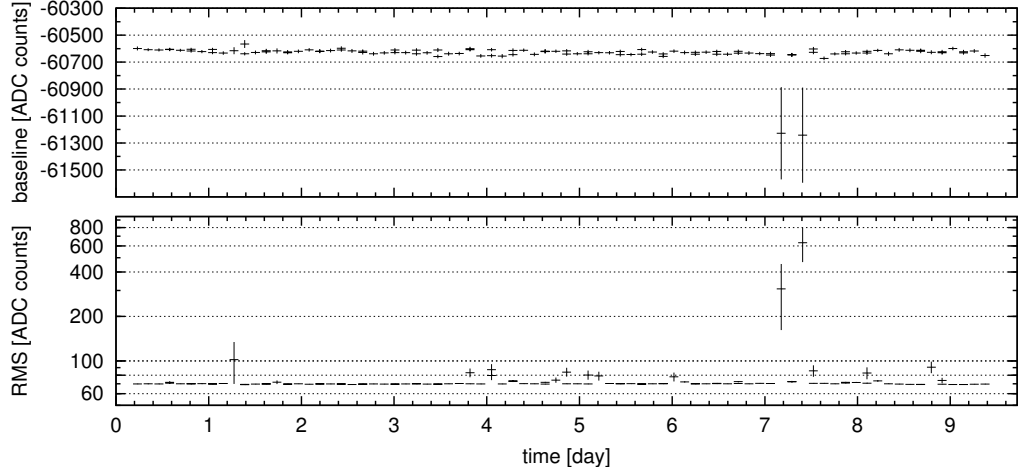


Figure 2.8: Average value (top panel) and RMS (bottom panel) of the signal baseline vs. time for a detector operated in GERDA during a 10-day run. The bin content represents the mean value of the parameter and the error bars are related to the width of the distribution. The bins are 2.4 hours wide.

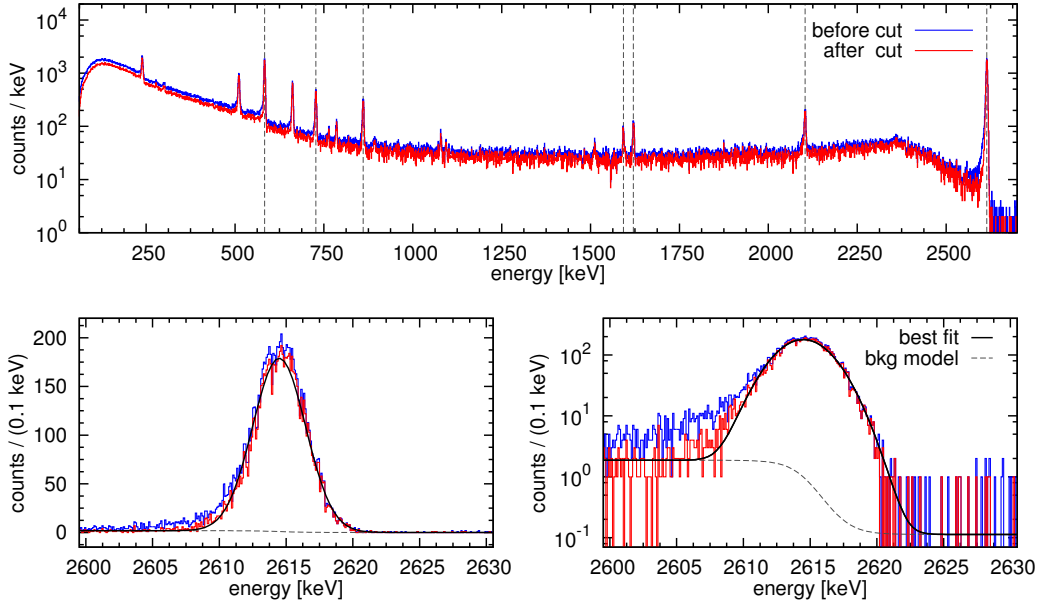


Figure 2.9: Energy spectrum recorded by an enriched detector deployed in the GERDA setup during a calibration run with a ^{228}Th source. The spectrum is shown before and after removing non-physical signals and pile-up events. The bottom panels show the peak of the 2.615 MeV gamma-line in linear and logarithmic scale. The reduction of the left tail due to pile-up events improves the fit with the analytical model (the χ^2 per degree of freedom is reduced from $\chi^2/254 = 1.77$ to 0.99).

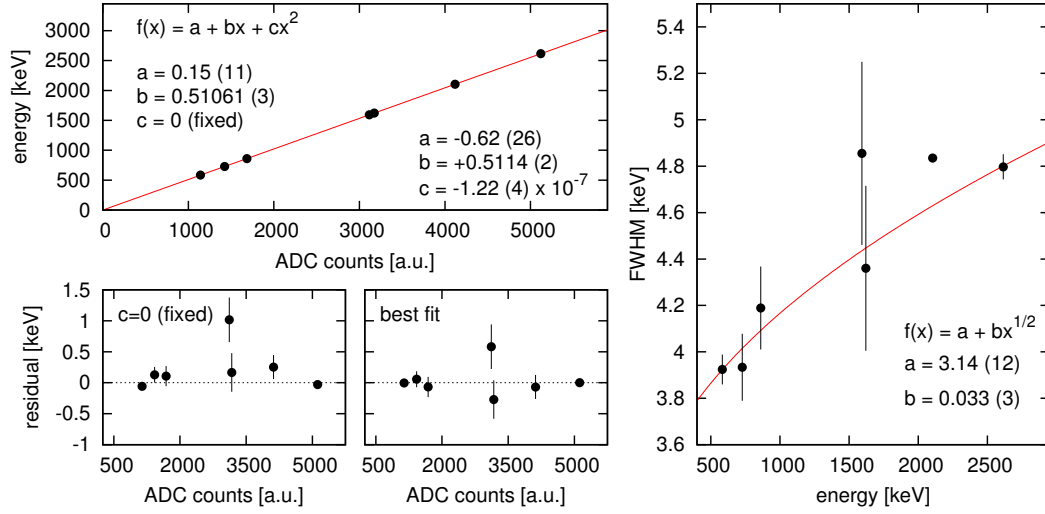


Figure 2.10: (Left) Best fit of the reconstructed ^{228}Th gamma-line positions (in ADC channel) with respect to the theoretical energy. The fit is performed with a second order polynomial function. The residuals are plotted for the best fit (quadratic fit) and, illustratively, for a fit in which the second order term is fixed to zero. (Right) Best fit of the FWHM as a function of energy performed using the resolution of the ^{228}Th gamma-lines. The point at 2103 keV is not included in the fit.

The estimation of the energy resolution as a function of energy is performed fitting the best values of the gamma-line widths (σ) with the function $\sigma(x) = a + b \cdot \sqrt{x}$, where a and b are two scalar parameters. A representative fit is shown in Figure 2.10 (right panel). The resolution is quoted in terms of the full width at half of the maximum of the Gaussian function ($\text{FWHM} = 2.355\sigma$), as conventionally done in gamma-ray spectroscopy. The extrapolation of the function at energy equal to zero, $\sigma(0) = a$, gives the best energy resolution achievable with the intrinsic noise of the present read-out chain and data acquisition system. Its value in the considered data set and with the present energy reconstruction filter is of ~ 3 keV. The second term of the function ($b \cdot \sqrt{x}$) is used to account for the statistical uncertainty of the number of electron-hole pairs generated in an event². The 2103.5 keV gamma-line is not included in the fit because it is widened by Doppler effect [63].

The variation of the energy scale in the considered data set is shown in Figure 2.11 using the shift of the 2615 keV gamma-line of ^{208}Tl over consecutive calibration runs. The energy drifts are correlated among the channels and part of the variations is expected to be related to temperature changes in the GERDA clean-room and lock-system. The shifts are generally $\lesssim 1$ keV with a maximum of ~ 2 keV. The figure shows also the energy resolution extracted

²The energy threshold to create an electron-hole pair in Ge is ~ 3 eV. The conversion between energy loss inside the detector and number of charge pairs produced is thus affected by statistical fluctuations. Note that the coefficient b includes also the Fano factor which accounts for statistically correlated processes involved in the transportation of radiation and charged particles through matter.

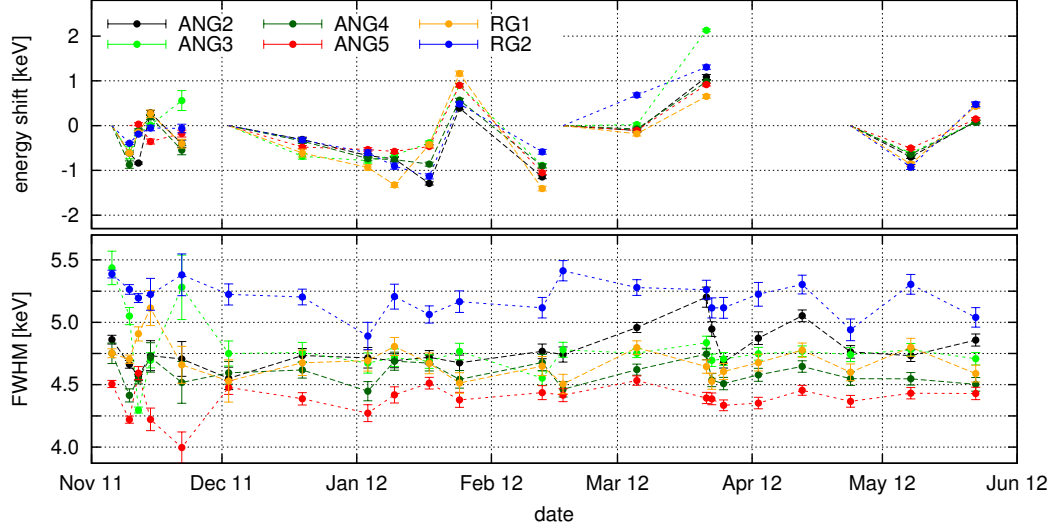


Figure 2.11: (Top) Shift of the 2615 keV ^{208}Tl gamma-line between successive calibrations as a function of time. The shift is computed with respect to the ADC channels and converted in energy using the new calibration function. The data points are grouped into sequences (connected by lines) during which no hardware operations were performed. The lines start from zero at the time of the first calibration of the sequence. The first point is shown at the time of the second calibration. (Bottom) Resolution measured on the 2615 keV ^{208}Tl gamma-line peak for each calibration run as a function of time.

by each calibration run for the 2615 keV ^{208}Tl gamma-line. The values are stable over the full data set and the energy resolution is below 5 keV for most of the detectors. Considering these results, we do not expect a strong deterioration of the energy resolution in the full physics data set with respect to the calibration runs. A quantitative analysis of these effects will be performed in the next feature before the physics analysis of the $0\nu\beta\beta$ signal.

2.3 Spectral analysis

The data set considered in this thesis includes the GERDA runs from 25 to 32, taken between November 9, 2011, and May 22, 2012. The period between March 22 and April 23 (run 31) is not considered because of instabilities in the setup. The duty cycle, excluding run 31, has been of 92.6%, equivalent to 165 live days. As previously mentioned, two enriched detectors developed high leakage current and are not considered in this analysis. The residual six enriched detectors have a total mass of 14.63 kg. The total mass of the three natural detectors is instead 7.59 kg.

The processing of the HPGe signals, the monitoring of the data quality and the energy calibration have been performed according to the analysis flow discussed in the previous

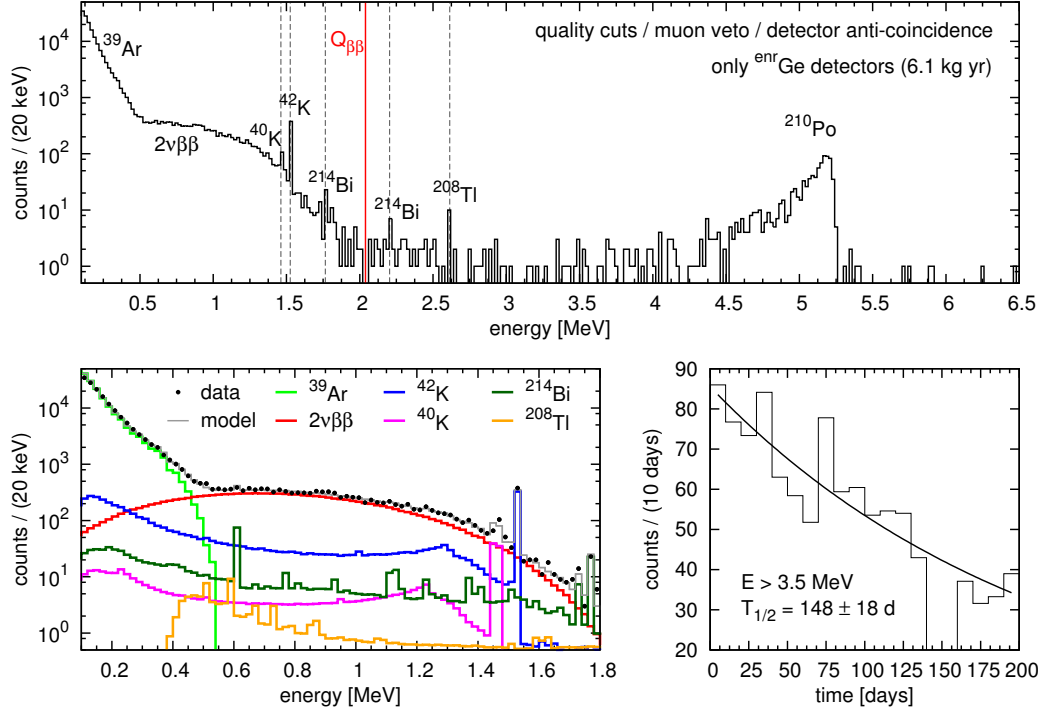


Figure 2.12: (Top) Energy spectrum measured by the enriched detectors deployed in the GERDA setup. The total exposure is 6.1 kg·yr. (Bottom left) Best background fit in the energy region below $Q_{\beta\beta}$. The plot is adapted from Ref. [64]. (Bottom right) Exponential fit of the count-rate dependence from time in the energy region above 3.5 MeV. The number of counts is corrected for the live time. The 30 days period with no counts corresponds to run 31 (not included in the data set) and is not considered in the fit. The extracted decay time is compatible within the uncertainties to the half-life of ^{210}Po (138 d).

section. The events above a few hundred keV that are discharged by the quality cuts have been visually inspected and found to be all traceable back to non-physical events or corrupted signals. Similarly, no undesired events have been found in the physical data set. The combined efficiency of the trigger system and of the off-line data processing can hence be approximate to 100% above 100 keV. In the following analysis, events occurring in coincidence with a muon-veto signal or with a trigger in multiple detectors are not considered.

The total exposure of the data set is hence 6.10 kg·yr for the enriched detectors and 3.17 kg·yr for the natural ones. The energy spectrum reconstructed using the data of the enriched detectors is shown in Figure 2.12 (top panel). The events in an energy window of 40 keV centered at $Q_{\beta\beta}$ (2039 keV) are not available for analysis. The GERDA collaboration plans to perform a blind analysis of the $0\nu\beta\beta$ signal and the events in this energy window will be studied only after fixing the analysis procedure and its parameters. The background

index, computed using a 200 keV window around $Q_{\beta\beta}$ (effective width 160 keV), is equal to $2.0^{+0.6}_{-0.4} \cdot 10^{-2}$ cts/(keV·kg·yr). This result is about an order of magnitude lower than the background level achieved in the previous ^{76}Ge -based experiments and it proves the validity of the GERDA innovative concept of deploying HPGe detectors bare in liquid argon. The spectrum shows various prominent structures in the energy region below $Q_{\beta\beta}$ and at higher energy around 5 MeV. Most of them were expected according to the design of the experiment, although their relative contributions were not known with accuracy. The features of the spectrum can be traced back to the following sources:

- **^{39}Ar :** this nuclide is the longest-lived isotope of Ar and its activity in liquid argon is expected to be 1.01 ± 0.08 Bq/kg [65]. ^{39}Ar is a beta-emitting isotope with $T_{1/2} = 269$ d and Q -value = 565 keV. Its decay in proximity of the detector array can induce background via direct interaction of the beta-ray or through secondary bremsstrahlung gammas. Its continuum spectrum dominates the background data in the low energy region.
- **$2\nu\beta\beta$:** the spectrum of the two-neutrino double beta decay is the main component in the energy region between 600 and 1400 keV and it extends up to $Q_{\beta\beta}$ (see Figure 1.5). The shape can be described using the Primakoff-Rosen approximation [66].
- **^{40}K :** this isotope is one of the rare example of nuclide that can decay at the same time by beta minus emission (Q -value = 1311 keV), beta plus emission and electron capture (Q -value = 1505 keV). It has extremely long life-time ($T_{1/2} = 1.3 \cdot 10^9$ yr) and it is expected in small concentration in the material surrounding the detectors, mainly in the PTFE parts of the detector mounting, cables and front-end electronics. Because of the location, its contribution is expected to be limited to the gamma-line at 1462 keV (emitted with $\sim 10\%$ probability) and the relative Compton continuum spectrum extending down to lower energies.
- **^{42}K :** ^{42}K is a short-lived beta-emitting nuclide (Q -value = 3525 keV, $T_{1/2} = 12.6$ h). It is produced homogeneously in liquid argon by the decay of the long-lived ^{42}Ar (Q -value = 599 keV, $T_{1/2} = 32.9$ yr), a natural isotope of argon created by cosmic-ray activation. Its concentration measured in GERDA is about a factor 2 higher [67] than the limits available in literature ($< 41 \mu\text{Bq/kg}$ at 90% C.L. [68]). After the production, ^{42}K ions are transported throughout the liquid argon volume by electric fields and convective flows. It is thus difficult to predict their location at the time of the decay. Its most visible contribution is the prominent gamma-line at 1525 keV (emitted with 18% probability).
- **^{214}Bi and ^{208}Tl :** these isotopes occur in the radioactive decay chain of ^{238}U and ^{232}Th . They both undergo beta-decay with a Q -value of 3.27 and 5 MeV, respectively,

and their contribution is clearly inferable from their gamma-lines. ^{214}Bi has multiple gamma-lines with a good signal-to-background ratio (e.g. 609, 1120, 1764, 2204 keV). ^{208}Tl has a characteristic gamma-line at 2615 keV. Both the isotopes can hence induce background in the $Q_{\beta\beta}$ region via gamma-ray interaction.

- **^{210}Po :** ^{210}Po is an alpha-emitting isotope with $Q\text{-value} = 5.41\text{ MeV}$ and $T_{1/2} = 138\text{ d}$ occurring in the decay chain of ^{222}Rn . The ^{210}Po signal is the dominant features of the high energy part of the spectrum, creating a prominent peak at the $Q\text{-value}$ of the decay and a tail on its left side extending to lower energies. The genuineness of the ^{210}Po signal has been confirmed by a time analysis of the event count rate above 3.5 MeV. The count-rate variation in time has been fitted with an exponential function, obtaining a decay time coherent with the ^{210}Po half-life (see Figure 2.12, bottom left panel). Consequently, there are no indications within the current statistics for a ^{210}Pb supported ^{210}Po contamination.

The best fit model in the energy region below $Q_{\beta\beta}$ is shown in Figure 2.12 (bottom left panel, taken from Ref. [64]). The probability distribution functions of each component have been generated by Monte Carlo simulations assuming specific source locations. The goodness of the fit indicates that the aforementioned background components are sufficient to accurately describe the data set with the present statistics. Thanks to the extremely low background level reached in the GERDA setup, the energy range between 600 and 1400 keV is dominated by the $2\nu\beta\beta$ spectrum. The extremely high signal-to-background ratio ($\sim 10 : 1$) allows to measure the $2\nu\beta\beta$ half-life with a drastic reduction of the systematic uncertainties with respect to the previous experiments. The best estimate of the $2\nu\beta\beta$ half-life is $T_{1/2}^{2\nu} = (1.84^{+0.14}_{-0.10}) \cdot 10^{21}\text{ yr}$ [51], summing in quadrature systematic and statistical uncertainties.

The intensity of the visible or expected gamma-lines have been estimated using the statistical analysis described in Appendix C.1. The results are reported in Table 2.2, separately for the natural and enriched detectors, and have been published in Ref. [50]. The table lists also the values measured in the Heidelberg-Moscow experiment, showing that the gamma-induced background achieved in GERDA is an order of magnitude lower than in the previous experiments. The intensity of the gamma-lines measured by the enriched detectors is systematically lower than for the natural ones. This issue is not fully understood and possible explanations include the different position of the natural detector string and the absence of the mini-shroud.

In addition to the contributions previously discussed, the gamma-lines due to ^{214}Pb (352 keV) and ^{228}Ac (911 and 969 keV) have been identified (^{214}Pb occurs in the U decay chain, ^{228}Ac in the Th decay chain). In particular, the ^{214}Pb signal has a strong statistical significance. The intensity of other expected gamma-lines, still not visible with the present exposure, has been constrained, i.e. ^{137}Cs , ^{212}Bi . The rate estimate of the ^{60}Co gamma-lines

Table 2.2: Intensity of the gamma-lines measured by the natural and enriched detectors deployed in the GERDA setup. The results are quoted with respect to the best fit value and the 68% probability. When the intensity of the gamma-line is compatible with zero, the 90% C.I. is quoted. The intensity measured in the Heidelberg-Moscow (HdM) experiment is also reported (computed on the full exposure of 71.7 kg·yr [35]). The gamma-line nominal energies are taken from Ref. [69].

isotope	energy [keV]	^{nat} Ge (3.2 kg·yr)		^{enr} Ge (6.1 kg·yr)		HdM
		tot/bck [cts]	rate [cts/(kg·yr)]	tot/bck [cts]	rate [cts/(kg·yr)]	rate [cts/(kg·yr)]
⁴⁰ K	1460.8	85 / 15	21.7 ^{+3.4} _{-3.0}	125 / 42	13.5 ^{+2.2} _{-2.1}	181 ± 2
⁴² K	1524.7	266 / 36	72.4 ^{+5.7} _{-5.4}	372 / 31	55.8 ^{+3.4} _{-3.3}	
⁶⁰ Co	1173.2	43 / 38	< 5.8	182 / 152	4.8 ^{+2.8} _{-2.8}	55 ± 1
	1332.5	31 / 33	< 3.8	93 / 101	< 3.1	51 ± 1
¹³⁷ Cs	661.7	46 / 62	< 3.2	335 / 348	< 5.9	282 ± 2
²¹⁴ Pb	351.9	740 / 630	34.1 ^{+12.4} _{-11.0}	1770 / 1688	12.5 ^{+9.5} _{-7.7}	138.7 ± 4.8
²¹⁴ Bi	609.3	99 / 51	15.1 ^{+3.9} _{-3.9}	351 / 311	6.8 ^{+3.7} _{-4.1}	105 ± 1
	1120.3	71 / 44	8.4 ^{+3.5} _{-3.3}	194 / 186	< 6.1	26.9 ± 1.2
	1764.5	23 / 5	5.4 ^{+1.9} _{-1.5}	24 / 1	3.6 ^{+0.9} _{-0.8}	30.7 ± 0.7
	2204.5	5 / 2	0.8 ^{+0.8} _{-0.7}	6 / 3	0.4 ^{+0.4} _{-0.4}	8.1 ± 0.5
²²⁸ Ac	911.2	54 / 38	5.1 ^{+2.8} _{-2.9}	294 / 303	< 5.8	29.8 ± 1.6
	969.0	64 / 42	6.9 ^{+3.2} _{-3.2}	247 / 230	2.7 ^{+2.8} _{-2.5}	17.6 ± 1.1
²¹² Bi	727.3	41 / 45	< 4.2	293 / 310	< 5.2	8.1 ± 1.2
²⁰⁸ Tl	583.2	56 / 51	< 6.5	333 / 327	< 7.6	36 ± 3
	2614.5	9 / 2	2.1 ^{+1.1} _{-1.1}	10 / 0	1.5 ^{+0.6} _{-0.5}	16.5 ± 0.5
e ⁺ annh	511	108 / 76	9.9 ^{+4.4} _{-4.1}	416 / 367	15.3 ^{+8.7} _{-8.1}	30 ± 3

is limited by the available statistics (the two gamma-emissions occur in cascade and should have almost the same count rate). Also, a gamma-line at 511 keV (labelled as “ e^+ annh” in Table 2.2) is clearly visible in the spectrum. The intensity of this line is likely due to various sources. In general, any mechanism creating a positron and hence a pair of 511 keV annihilation gammas – e.g. gamma-ray pair production and beta plus decay – can contribute to it.

The count distribution in the energy regions of the gamma-lines for the enriched detectors is shown in Figure 2.13. The smaller energy scale of this plot allows to appreciate the low background counting statistics achieved in the GERDA setup, especially in the $Q_{\beta\beta}$ region. Given the background index of $2.0^{+0.6}_{-0.4} \cdot 10^{-2}$ cts/(keV·kg·yr), we would expect less than 5 background counts homogeneously distributed in the 40 keV blinded window around $Q_{\beta\beta}$. In comparison, assuming the $0\nu\beta\beta$ half-life computed in Ref. [34], an excess of ~ 2 counts is expected in the central ~ 8 keV ($Q_{\beta\beta} \pm 2\sigma$).

2.4 Conclusions

The GERDA experiment started the data taking of Phase I in November 2011. The off-line analysis of the HPGe detector signals is performed using a new software framework, specifically developed for GERDA in the context of this thesis. The framework handles the full data streaming of the experiment and supports a multi-channel customizable analysis. The algorithms used to process the digitized signals, as well as the analysis flow, have been defined and optimized. In addition, we identified a set of parameters to discriminate signals induced by non-physical events and to monitor the data quality.

The overall performance of the GERDA apparatus was closely monitored during this first part of data taking and found to meet the experimental requirements. The energy scale and resolution of the HPGe detectors are measured regularly (every one/two weeks) with dedicated calibration runs and fluctuations are generally $\lesssim 1$ keV. Compared to the Heidelberg-Moscow experiment, the background level reached by GERDA is almost an order of magnitude lower. The main features of the background spectrum can be traced back to sources already considered in the design phase of the experiment, although their relative contributions were not known with accuracy. The main candidates to explain the background count rate at $Q_{\beta\beta}$ seem to be the isotopes occurring in the ^{238}U and ^{232}Th decay chains.

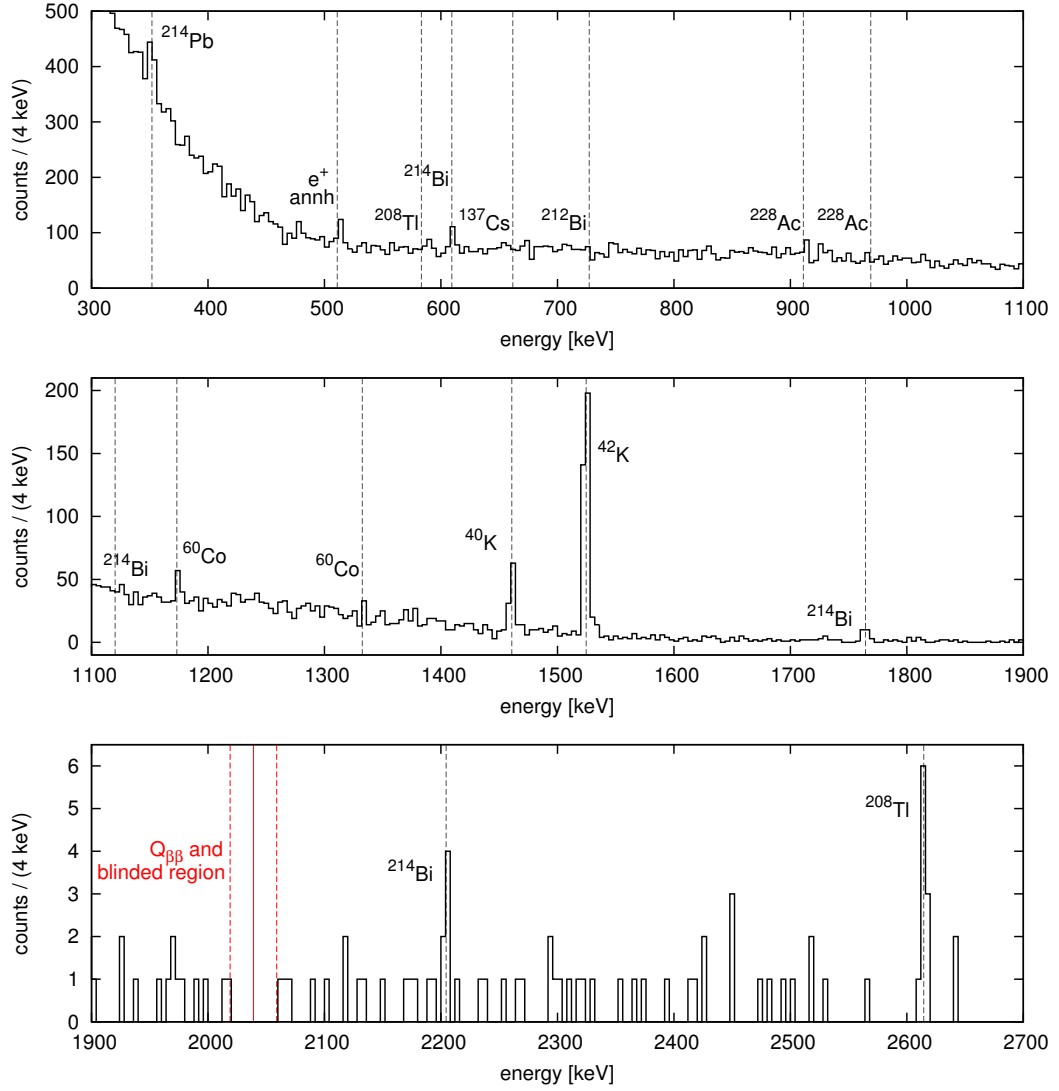


Figure 2.13: Spectrum measured by the enriched detectors deployed in the GERDA setup (6.1 kg-yr). The energy of gamma-lines analyzed in table 2.2 is marked with a dotted line. The events in a 40 keV region around $Q_{\beta\beta}$ are not accessible because of the data blinding.

Chapter 3

Background decomposition at $Q_{\beta\beta}$

This chapter presents a decomposition of the GERDA-Phase I background in the $Q_{\beta\beta}$ region. The analysis relies on a pulse shape discrimination technique for the identification of interactions on the surface of the p+ electrode or groove, typically due to alpha and beta emitting isotopes. This tool, described in Section 3.2, is used in combination with Monte Carlo simulations and spectral fitting to evaluate the count rate of each background component (Section 3.3). The background model developed is hence used in Section 3.4 to quantify the improvements in the experimental sensitivity expected by the use of pulse shape discrimination techniques for surface or multiple-site event rejection.

The analysis is applied to the enriched coaxial detectors. The data set includes the GERDA runs from 25 to 32 (excluding run 31). The data set, the quality cuts and the calibrations are discussed in the previous chapter. The total exposure of the data set is 6.1 kg·yr with a background index of $20^{+6}_{-4} \cdot 10^{-3}$ cts/(keV·kg·yr).

3.1 Considered background sources

In this analysis we will consider only the background sources that can generate events with energy deposition at or above $Q_{\beta\beta}$ and whose presence is deducible from, and compatible with, the spectral analysis presented in Section 2.3. The radioactive elements whose signal is directly visible in the background spectrum are: ^{214}Bi and ^{210}Po (^{238}U decay chain), ^{228}Ac and ^{208}Tl (^{232}Th decay chain), and ^{42}K (progeny of the cosmogenically-activated ^{42}Ar). The background due to other gamma-emitting elements, neutrons, cosmogenic isotopes inside the detectors¹, and non-vetoed muons is negligible. All decays are assumed to occur outside or on the surface of the detectors given the absence of sharp peaks at the energies of the alpha-emissions, which would show up in case of bulk contaminations.

¹The present background index due to cosmogenic ^{68}Ge and ^{60}Co decaying inside the enriched detectors is expected to be $< 1.3 \cdot 10^{-3}$ cts/(keV·kg·yr) assuming the values given in Ref. [48]

Table 3.1: ^{238}U and ^{232}Th decay chains. The long-lived isotopes ($T_{1/2}$ longer than one year) are highlighted to ease the identification of the sub-chains (indented elements). The isotopes identified through spectral analysis are marked with a star. In alpha decays, the energy of the emitted particle is close to the Q-value of the reaction (the kinetic energy of the recoiling nucleus is of the order of 100 keV). In beta-decays, the electron energy is usually lower than the Q-value and the decay is followed by the emission of de-excitation gamma-rays. The values are taken from Ref. [69].

Isotope	decay	$T_{1/2}$	Q-value [MeV]	Isotope	decay	$T_{1/2}$	Q-value [MeV]
$^{238}_{92}\text{U}$	α	10^9 yr	4.27	$^{232}_{90}\text{Th}$	α	10^{10} yr	4.08
$^{234}_{90}\text{Th}$	β/γ	24 d	0.27	$^{228}_{88}\text{Ra}$	β/γ	6 yr	0.05
$^{234}_{91}\text{Pa}$	β/γ	1 m	2.20	$^{228}_{89}\text{Ac}^*$	β/γ	6 h	2.13
$^{234}_{92}\text{U}$	α	10^5 yr	4.86	$^{228}_{90}\text{Th}$	α	2 yr	5.52
$^{230}_{90}\text{Th}$	α	10^5 yr	4.77	$^{224}_{88}\text{Ra}$	α	4 d	5.79
$^{226}_{88}\text{Ra}$	α	10^3 yr	4.87	$^{220}_{86}\text{Rn}$	α	56 s	6.40
$^{222}_{86}\text{Rn}$	α	4 d	5.59	$^{216}_{84}\text{Po}$	α	145 ms	6.91
$^{218}_{84}\text{Po}$	α	3 m	6.11	$^{212}_{82}\text{Pb}$	β/γ	11 h	0.57
$^{214}_{82}\text{Pb}^*$	β/γ	27 m	1.02	$^{212}_{83}\text{Bi}$	α	61 m	6.21
$^{214}_{83}\text{Bi}^*$	β/γ	20 m	3.27	$^{212}_{83}\text{Bi}$	β/γ	25 m	2.25
$^{214}_{84}\text{Po}$	α	164 μs	7.83	$^{212}_{84}\text{Po}$	α	299 ms	8.95
$^{210}_{82}\text{Pb}$	β/γ	22 yr	0.06	$^{208}_{81}\text{Tl}^*$	β/γ	3 m	5.00
$^{210}_{83}\text{Bi}$	β/γ	5 d	1.16				
$^{210}_{84}\text{Po}^*$	α	138 d	5.41				

The identification of several elements occurring in the U and Th decay chain lead us to take into consideration the other elements produced in the same decay chain, despite the absence of a clear signal in the spectrum. We split the decay chain into sub-chains every time a long-lived isotope is produced and, as secular equilibrium is often broken, only the elements in the same sub-chains of the aforementioned isotopes are considered (the sub-chains are quoted in Table 3.1, each starting with a bold-faced element and including all the isotopes indented). The contribution of these additional elements is however strongly constrained by the data. Most of the candidate isotopes undergo alpha-decay and would generate a signal in the high-energy part of the spectrum in case of contaminations on the detector surface. In the considered data set, however, the events above 3.5 MeV cluster at the ^{210}Po alpha-emission energy (5.3 MeV) and their decay rate is decreasing with half-life compatible with ^{210}Po (138 days). Only a few events are energetically not compatible with ^{210}Po (9 events above 5.4 MeV). Concerning beta-emitting isotopes, the only new candidate is ^{212}Bi . The absence of its characteristic gamma-line at 727 keV indicates that its contribution is negligible.

The analysis here presented aims at decomposing the background according to the isotope responsible and the type of primary particle depositing energy inside the detector

(alpha-, beta- or gamma-ray). The particle type determines the locations from which an isotope can contribute to the background and the distribution of the energy deposition inside the detector (topology and location).

Alpha-rays have an attenuation length in liquid argon (LAr) or Ge of the order of tens of μm . Consequently, alpha-emitting isotopes can create background only when the decay occurs a few μm close to the detector surface. In particular, only decays close to the boron-implanted p+ electrode or groove surface can release energy in the detector active volume. The dead layer thickness in this regions is $\lesssim 1\ \mu\text{m}$, while the rest of the detector outer surface is covered by a thick Li-diffused n+ electrode creating a dead layer between 1 and 3 mm in the Phase I detectors. The energy deposition of an alpha particle inside the detector is always on the surface and point-like.

Beta-rays have instead an attenuation length of the order of millimeters and they can reach the detector active volume when the decay happens in proximity of both the p+ and the n+ electrode. The energy deposition is well localized (within a few millimeters) and in proximity of the detector surface. Bremsstrahlung-gammas emitted by the electron can however create secondary interaction sites spread across the full detector volume.

Gamma-rays at high energy have high penetrating power and can deposit energy inside the detector even when the decaying isotope is far from the detector array. The topology of a gamma-induced energy deposition is characterized by a single or multiple interaction sites spread across the full detector volume.

In the following, we will refer to the three event topologies as *alpha-events*, *beta-events* and *gamma-events*. Events generated by the combined interaction of a beta- and gamma-rays will be defined as beta-events when most of the energy is released by the beta-rays. The isotopes considered in this analysis can induce all three types of events. Alpha-events are expected mainly by ^{210}Po . Other potential alpha-emitting elements are listed in Table 3.1, in the sub-chains sustained by ^{226}Ra , ^{210}Pb and ^{228}Th . Beta-events at $Q_{\beta\beta}$ can be produced by ^{42}K , ^{214}Bi and ^{228}Ac . Finally, the isotopes able to create gamma-events above 2 MeV are ^{208}Tl (gamma-line at 2614.5 keV with 99% probability), ^{214}Bi (gamma-line at 2204.5 keV with 5% probability) and ^{42}K (gamma-line at 2224 keV with 0.02% probability).

The contribution of ^{228}Ac will not be considered in this chapter because it is expected to be below the sensitivity of the analysis. As previously discussed, beta-events are induced only when the decay occurs in proximity of the detector surface. In this location the detection efficiency for gamma-line is very high. The total number of counts in the ^{228}Ac 911 and 969 keV gamma-lines (emitted with 16% and 27% probability) is however $\lesssim 20$ in 6.1 kg·yr. The only electron emission of ^{228}Ac with energy above $Q_{\beta\beta}$ occurs with 10% probability. The beta-emission occurs at 2066 keV and the probability for the electron to deposit more than 2 MeV inside the detector active volume is very low. The ^{228}Ac contribution is hence expected to be $< 10^{-3}$ cts/(keV·kg·yr). However, its potential contribution should not be neglected in future analyses based on larger data sets.

3.2 Pulse shape analysis

This section describes the design of the pulse shape analysis and its application to physics and calibration data. First, the detector response as a function of the interaction location is investigated using pulse shape simulations. The information is then used to identify a good parameter for discriminating surface events on the p+ electrode and groove. The central part of the section describes the calibration of the parameter and the resulting classification of the event in the GERDA background data. Finally, the energy dependence of the cut is discussed using calibration data.

3.2.1 Signal modeling of coaxial detectors

The development of the pulse shape analysis and the interpretation of its results have been supported by dedicated pulse shape simulations. The calculation of the electric field inside the Ge crystal and of the charge transportation has been performed with an enhanced version of the MGS software [70, 71]. The code has been validated in Ref. [71] for the specific case of BEGe detector geometries and has been successfully used in Ref. [72] for qualitative simulations of a coaxial detector (GTF44 deployed in the GERDA setup during the commissioning phase).

The geometry of an enriched detector, ANG3, has been implemented over a 0.5 mm-step grid² using the technical drawings provided by the manufacturer. The only unavailable parameter was the impurity concentration of the Ge crystal. Its value has been determined by comparing the experimentally-measured depletion voltage with the simulated value for different impurity concentrations (similarly to the method proposed in Ref. [73]). The experimental value has been taken from a measurement of the detector capacitance as a function of the HV carried out by the manufacturer after the detector refurbishment. Assuming a depletion voltage of $\sim 3000\text{V}$, the average impurity concentration has been estimated to be $\sim 0.9 \cdot 10^{10} \text{ atoms/cm}^3$. The distribution is assumed to be uniform for the lack of additional information. The electrode scheme, the dimensions of the crystal and the simulated electric potential and field of ANG3 are shown in Figure 3.1.

To study the correlation between signal shape and interaction position, the detector active volume has been sampled simulating mono-energetic point-like interactions. A representative selection of signals is shown in Figure 3.2. According to the simulation, most of the detector active volume produces signals characterized by a fast leading edge at the end of the charge collection. Conversely, the volume surrounding the bore-hole generates charge signals with a fast rising part at the beginning of the charge collection. Finally, the regions in proximity of the groove and at the bottom of the bore-hole create signals with a steeper leading edge

²The detector geometry is defined over a three dimensional grid with spatial distance between two consecutive vertexes of 0.5 mm. The subsequent computation of the electric potential and field is also performed over the grid. The charge carrier transportation is instead calculated interpolating the values of the field in the grid vertexes.

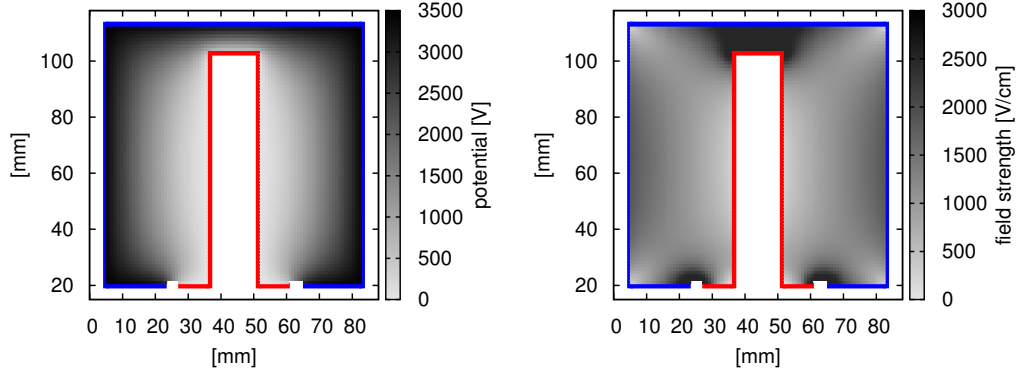


Figure 3.1: Simulated electrical potential (left) and field strength (right) for a vertical section of the detector passing through the symmetry axis. The n+ and p+ electrode are indicated with a blue and red line respectively. The two electrodes are divided by a groove visible in the bottom part of the plots.

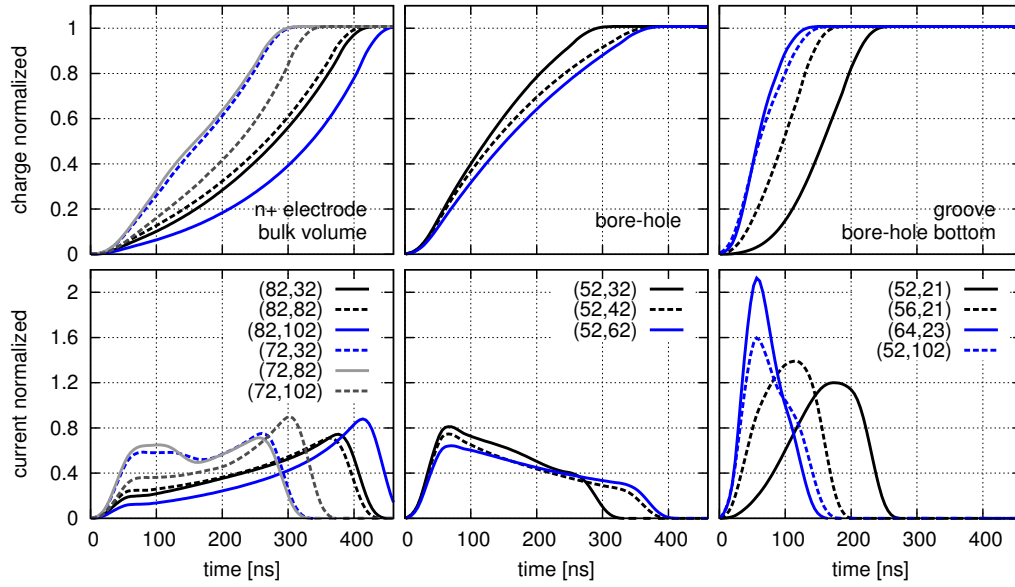


Figure 3.2: Simulated signals for point-like energy depositions occurring close to the detector surface or in the bulk-volume. The coordinate frame is the same of Figure 3.1. The charge pulses are integrated with a three-fold 30 ns moving average to reproduce the effect of the preamplifier, the cables and the anti-aliasing filter of the FADC. The current signals are computed by differentiating the charge signals.

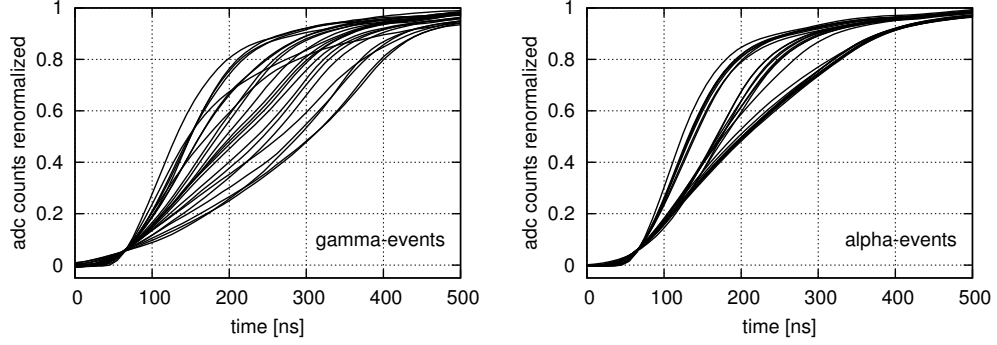


Figure 3.3: Traces recorded by ANG3 during calibration (left plot) and physics (right) runs. The signals are extracted in the energy regions 2000-2100 keV and 5200-5500 keV respectively. The pulses are renormalized according to the reconstructed event energy and aligned in time using a leading-edge trigger with threshold equal to the 5% of the maximum signal amplitude.

(at the limit of the electronic bandwidth). In these volumes the charge collection is faster than in the rest of the crystal because of the reduced distance between the electrodes and the consequently stronger electric field (see Figure 3.1). The features of the three types of signals are related to the basic charge collection mechanism of coaxial detectors and, as shown in Ref. [72], are expected to be valid over a wide range of geometrical parameters (including all enriched detectors deployed in GERDA Phase I) and to be independent of the event energy.

The simulation predictions have been compared with the GERDA experimental data and found to be consistent. Figure 3.3 shows illustrative traces extracted from a pure sample of gamma- and alpha-events. The gamma-events are taken from calibration runs selecting data in the SSE-rich Compton continuum of the ^{208}Tl 2.6 MeV gamma-line. The alpha-events are instead extracted from the ^{210}Po alpha peak visible in the physics runs. As discussed in Section 3.1, gamma-events generate interactions spread across the whole detector active volume while alpha-events are expected only on the surface of the p+ electrode and groove. Under this assumption, the simulated signals shown in Figure 3.2 reproduce qualitatively all the features of the experimental traces.

3.2.2 Discrimination method and application

The method developed to identify events on the p+ electrode or groove surfaces is a mono-parametric pulse shape analysis of the charge signals. The parameter chosen is the rise time between 5% and 50% of the maximum pulse amplitude (rt_{5-50}). It is extracted after integrating the traces with a three-fold 30 ns moving average to reduce the noise and improve

the parameter evaluation at low energies. The pulses are also interpolated down to 1 ns sampling period to increase the time resolution³.

The pulse shape discrimination capability of the rt_{5-50} was firstly postulated comparing the simulated signals in Figure 3.2 and then tested on the experimental data. The rt_{5-50} parameter was preferred over alternative solutions because of its relatively good efficiency and simplicity. Parameters based on the relative position of the stationary and inflection points of the charge signal, able to distinguish concave and convex shapes, have been tested and found to provide similar performances despite their increased complexity. Moreover, the performance of the rt_{5-50} parameter has been found to be stable within the statistical uncertainty for small variation of the lower bound (1-10%) and upper bound (30-60%). Outside this range, the discrimination capability of the parameter deteriorates significantly.

The event classification is performed using a simple cut on the rt_{5-50} parameter. The cut is performed at a fixed threshold and is calibrated separately for each detector using the rt_{5-50} distribution of the pure sample of alpha-events in the ^{210}Po peak. In this analysis, the threshold is defined as the minimum rt_{5-50} value below which 95% of the events between 4.8 and 6 MeV lie. Since the rise time is expected to be energy independent, the efficiency of the cut in identifying alpha-events is tuned by definition to 95%.

Figure 3.4 shows the distribution of the events as a function of rt_{5-50} and energy. The horizontal line in the plots indicates the cut threshold. Most of the high-energy events used to calibrate the cut cluster at the energy of the ^{210}Po peak and their rise time is fully compatible with decays on the bore-hole surface (Figure 3.2, middle panels). From the peak, a tail of degraded alpha-events extends to lower energies with constant rt_{5-50} , confirming the expectation that this parameter is energy independent. An additional component of alpha events with a faster rise time is present in all detectors. This component is compatible with interactions close to the groove or the bottom part of the bore-hole (Figure 3.2, right panels). Below the 2.6 MeV gamma line, we observe a large number of events above the threshold expected to be induced by gamma-interactions in the bulk volume or beta-interactions in the n+ electrode region (Figure 3.2, left panels).

The value of the rt_{5-50} cut threshold in the detectors with a high count rate in the ^{210}Po peak (ANG2, ANG3, ANG5) is defined with low statistical uncertainty. The spread of its values, between 125 and 150 ns, can be explained by differences in the crystal geometries and the impurity concentration profiles. In the other detectors, the accuracy of the cut threshold calibration is limited by the low counting statistics in ^{210}Po peak. However, the derived cut value is justified as the thresholds are within 10% equal to that obtained for ANG3 and ANG5.

A proper validation of the pulse shape analysis and a quantitative study of its systematics can be achieved only performing a set of dedicated measurements on the enriched detectors

³The processing has been performed with a chain of GELATIO modules composed of *MWAverageModule*, *InterpolationModule* and *RiseTimeModule*.

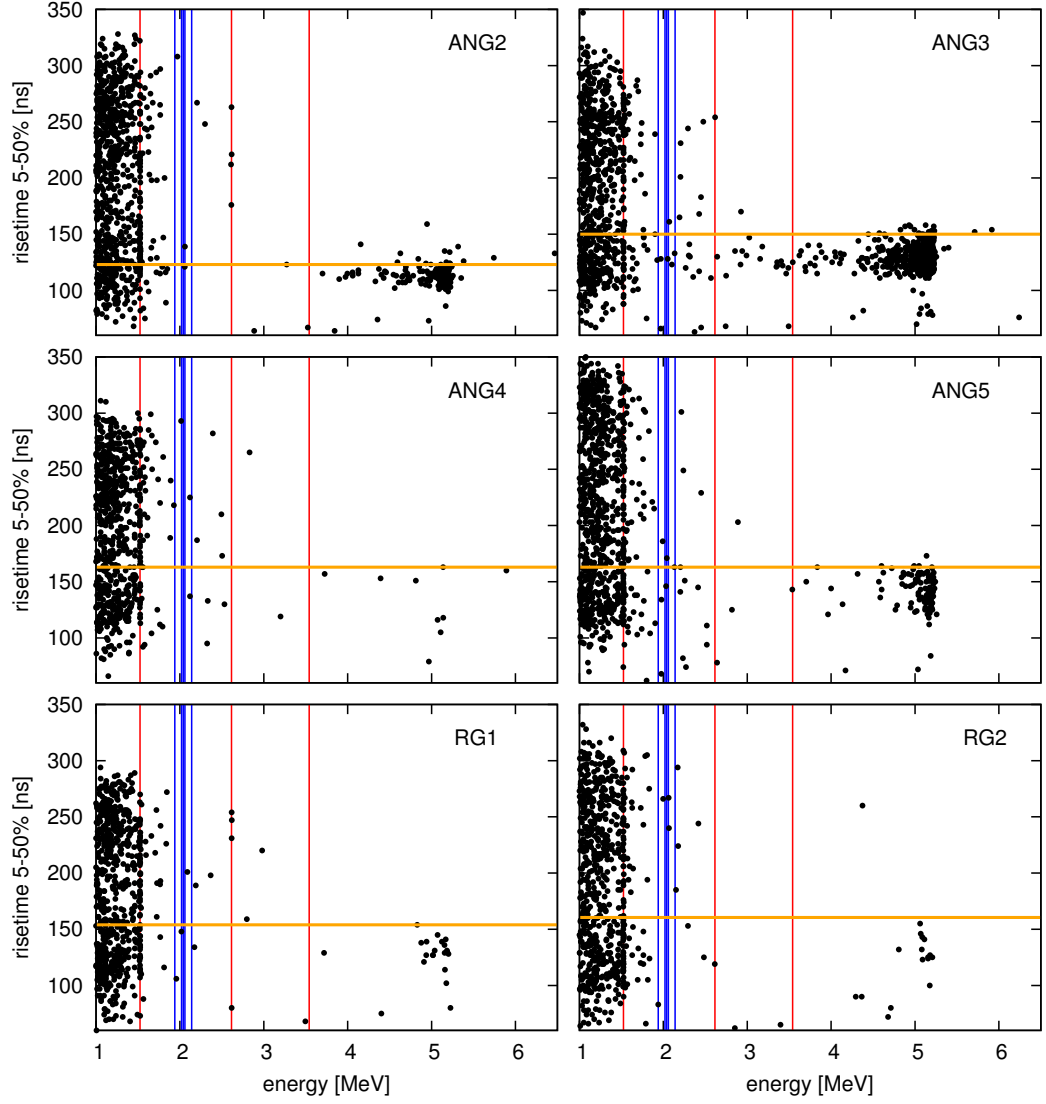


Figure 3.4: Event distribution in the rt_{5-50} vs energy space. The horizontal orange lines show the cut threshold. The following energy values has been highlighted: 1525 keV (K-42 gamma-line), $Q_{\beta\beta} \pm 100$ keV (region used to estimate the BI), $Q_{\beta\beta} \pm 20$ keV (blinded region), 2614 keV (^{208}Tl gamma-line), 3540 keV (^{42}K end point).

(with collimated alpha and beta sources). It would require the removal of the detectors from the GERDA setup and hence an interruption of the data taking. Presently we do not plan to perform such a set of measurements as the main goal of the collaboration is to maximize the sensitivity for the neutrinoless double beta decay half-life. However, the pulse shape analysis results and the simulations are in good agreement, supporting the validity of the analysis.

In the following, we will use the working hypothesis that alpha- and beta-events on the p+ electrode and groove surfaces are reconstructed below the cut threshold with 95% probability. The rt_{5-50} cut is interpreted as a pure volume cut. This assumption will be corroborated in the following sections by analyzing the survival probability of the cut for ^{228}Th calibration data. The fraction of volume affected by the cut is estimated in Section 3.3 using the $2\nu\beta\beta$ -dominated region of the background spectrum.

3.2.3 Energy dependence of the cut acceptance

The energy dependence of the rt_{5-50} cut acceptance has been qualitatively studied using calibration data. The Compton continuum (CC) created by the ^{208}Tl 2.6 MeV gamma-line provides samples of data at different energies with similar topologies and spatial distribution inside the detector.

Figure 3.5 shows the energy distribution of calibration data recorded by ANG3 and their classification with respect to the rt_{5-50} threshold. Selecting the events above or below the cut threshold does not change visually the shape of the spectrum. The only significant difference concerns the count rate in the double and single escape peaks of the 2.6 MeV gamma-line (peaks at 1592 and 2103 keV). Their count rate compared to the other gamma-lines – e.g. compared to the gamma-line at 1620 keV – increases when only the events above the band are selected. These features support the assumption that the rt_{5-50} cut is a volume cut. The events in the full absorption gamma-lines or in the CC are distributed uniformly inside the detector to first approximation. The single/double escape events have instead higher probability to occur near the detector n+ surface than close to the bore-hole, because of the geometrical efficiency for the escape of the 511 keV gammas.

Figure 3.6 shows a quantitative comparison of the percentage of events below the cut threshold for different energy region and detectors. While the acceptance of the cut seems to be energy independent within the statistical uncertainty, the average value changes significantly among the detectors (from 14% of ANG2 to 35% of RG2). The spread can be attributed to the different crystal geometries, resulting in different electric field configurations, and to the spatial distribution of the ^{210}Po contamination, which affects the pulse shapes and hence the calibration of the cut threshold. The particular low cut value of ANG2 could, for instance, be explained by a ^{210}Po decays localized on the groove of the detector (Figure 3.2, right panels).

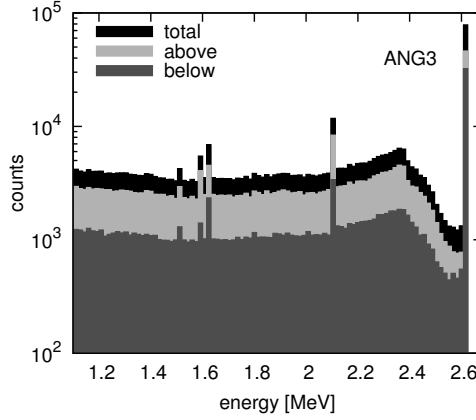


Figure 3.5: Classification of ^{228}Th calibration data in ANG3 with respect to the rt_{5-50} threshold.

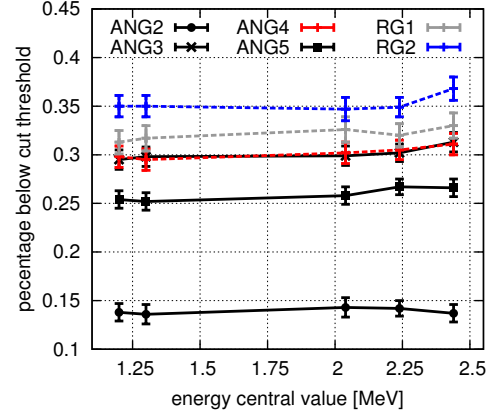


Figure 3.6: Percentage of gamma-events below the rt_{5-50} threshold in 100 keV energy windows and statistical uncertainty. Note that ANG3 and ANG4 data overlap.

3.3 Background decomposition at $Q_{\beta\beta}$

In this section, the event classification performed by the pulse shape analysis (PSA) is used together with Monte Carlo simulations (MC) and spectral analysis to decompose the background in the $Q_{\beta\beta}$ region. The analysis relies on the assumptions regarding the background components discussed in Section 3.1. In addition, we use the working hypothesis discussed in Section 3.2.2, according to which alpha- and beta-events on the p+ electrode and groove surfaces are reconstructed below the cut with 95% probability. The small cut inefficiency will be neglected in the region of interest because of the low counting statistics.

Under these assumptions, the events reconstructed above the threshold in the $Q_{\beta\beta}$ region are: beta-events close to the n+ electrode (due to ^{42}K and ^{214}Bi) or gamma-events spread across the detector bulk volume or in proximity of n+ electrode (generated by ^{208}Tl , ^{214}Bi and ^{42}K). The events reconstructed below the cut threshold are: beta-events located in proximity of the p+ electrode and groove (due to ^{42}K and ^{214}Bi); gamma-events close to the bore hole (induced by ^{208}Tl , ^{214}Bi and ^{42}K) or alpha-events on the surface of the p+ electrode or groove (mainly ^{210}Po).

The structure of the analysis is shown in Table 3.2. The logical flow can be divided into four steps:

- 1) **Beta-events.** The beta-events count rate at $Q_{\beta\beta}$ (from ^{42}K and ^{214}Bi) is estimated using MC simulations. The simulations are performed placing the isotopes in different locations. In particular, decays close to the p+ electrode or n+ electrode are simulated individually, to estimate separately the count rate in the two regions. The scenarios

providing the highest beta-event count rate compatible with the data are used to set upper limits.

- 2) **Gamma-events.** The amount of gamma-events above the rt_{5-50} cut threshold is estimated by removing from the total count rate above the threshold the expected number of n+ electrode beta-events derived previously. The total number of gamma-events at $Q_{\beta\beta}$, including both the ones above and below the cut threshold, is then computed using the probability for gamma-events of being reconstructed above the cut threshold (73%, computed in Section 3.2.3 using calibration data).
- 3) **Alpha-events.** The high-energy part of the alpha-event distribution is fitted with simulated ^{210}Po spectra to extrapolate the expected amount of degraded alpha-events at $Q_{\beta\beta}$.
- 4) **Consistency check.** The sum of the three contributions expected below the cut threshold is compared with the experimental data to check the consistency of the analysis.

The event classification used for the analysis is summarized in Table 3.3. The reference region for the analysis ($Q_{\beta\beta}^{160}$) is defined as a 200 keV window centered at the $Q_{\beta\beta}$ energy. The events in the central 40 keV region are not considered in the analysis because of the data blinding. The total size of the region is thus 160 keV. The table includes also the acceptance of gamma-events in the $Q_{\beta\beta}^{160}$ window, computed from the calibration data, and of the two neutrino double-beta decay ($2\nu\beta\beta$) events, extracted from the background data in the region between 600 and 1400 keV, where the $2\nu\beta\beta$ signal is the dominant component of the spectrum. The $2\nu\beta\beta$ events provide a sample of single-site events homogeneously distributed in the crystal. Since the event classification corresponds to a volume cut, their acceptance is proportional to the fraction of the detector active volume generating events above or below the cut threshold.

Table 3.2: Summary of the background components in different detector volumes and of the analysis methods used to estimate their count rate.

	beta-events ^{42}K ^{214}Bi	gamma-events ^{42}K ^{214}Bi ^{208}Tl	alpha-events ^{210}Po
n+ electrode	MC	PSA	
bulk volume			
p+ electrode	MC		MC/fit

Table 3.3: Background event classification according to the rt_{5-50} cut threshold in the $Q_{\beta\beta}^{160}$ window. The table shows also the percentage of $2\nu\beta\beta$ and Compton continuum (CC) events from ^{228}Th calibration above and below the cut threshold (with statistical uncertainties).

detector	mass [kg]	$Q_{\beta\beta}^{160}$		$2\nu\beta\beta$ (600-1400 keV)		CC ($Q_{\beta\beta}^{160}$)	
		above	below	above	below	above	below
ANG2	2.77	2	0	0.81 (4)	0.19 (6)	0.86 (1)	0.14 (1)
ANG3	2.34	1	4	0.63 (4)	0.38 (5)	0.70 (1)	0.30 (1)
ANG4	2.30	2	1	0.66 (4)	0.34 (5)	0.70 (1)	0.30 (1)
ANG5	2.67	2	2	0.70 (4)	0.30 (5)	0.75 (1)	0.25 (1)
RG1	2.04	1	2	0.65 (4)	0.35 (5)	0.68 (1)	0.32 (1)
RG2	2.08	3	0	0.64 (4)	0.37 (5)	0.65 (1)	0.35 (1)
Total	14.2	11	9	0.68 (2)	0.32 (2)	0.73 (1)	0.27 (1)

3.3.1 Monte Carlo simulation of beta-emitting isotopes

The amount of beta-events in the GERDA data has been studied simulating ^{42}K and ^{214}Bi decays nearby the detectors. The attenuation length for beta-rays in liquid argon and germanium is of the order of millimeters and only decays in the bore-hole or close to the groove surface can produce high-energy beta-events. Decays on the n+ electrode surface can also yield events at $Q_{\beta\beta}$ but their probability is suppressed with respect to the p+ electrode because of the thick n+ dead layer. Since the distribution and concentration of ^{42}K and ^{214}Bi is not known with accuracy, multiple scenarios have been simulated assuming conservatively the highest activity compatible with the data.

To reduce the computation time, a simple geometry of a coaxial detector immersed in a liquid argon volume has been implemented in the MaGe framework [74]. The detector geometrical parameters are the average of the Phase I detector ones: the diameter/height of the crystal and the bore-hole are respectively 78/90 mm and 13/80 mm; the p+ and n+ electrode dead layers are 300 nm and 2 mm thick. The values are taken from the technical drawings provided by the manufacturer and the characterization measurements of Ref. [48].

The simulations have been performed tracking the particle interactions to distinguish localized beta-events on the detector surface from events with primary high-energy gamma-rays producing interactions spread across the whole detector volume. The event classification is done applying a cut on the distributions of two parameters: the radius of the spherical volume containing 90% of the total energy released in the active volume (R_{90}), and the distance between the R_{90} centroid and the decay position (R_{90}^d). The two parameters work in combination. R_{90} is used to identify single-site interactions which can be due both to beta- or gamma-events. Then R_{90}^d is used to reject gamma-events that occur far from the decay vertex. The values of these parameters for a typical high-energy beta-event are of the order of millimeters and can reach a few centimeters in case of hard-bremsstrahlung. To

maximize the acceptance of beta-events, the cut threshold has been conservatively set to:

$$R_{90} < 1 \text{ cm} \quad \text{and} \quad R_{90}^d < 2.5 \text{ cm}$$

The cut acceptance has been estimated using pure samples of beta- and gamma-events, generated with specific simulations in which only one type of primary particle is propagated (or beta- or gamma-rays respectively). The beta-event acceptance is to good approximation independent of the event energy and $\geq 95\%$ in the whole energy range considered (only hard-bremsstrahlung events are discarded). The acceptance of gamma-events varies significantly with the energy and its value at $Q_{\beta\beta}$ is 10-15%.

^{42}K beta-induced background

^{42}K is a short-lived beta-emitting nuclide ($Q\text{-value} = 3525 \text{ keV}$, $T_{1/2} = 12.6 \text{ h}$) produced homogeneously in liquid argon by the decay of the long-lived ^{42}Ar ($Q\text{-value} = 599 \text{ keV}$, $T_{1/2} = 32.9 \text{ yr}$), a natural isotope of argon created by cosmic-ray activation. After the production, ^{42}K ions drift in presence of electric fields and are transported by convective flows of the LAr. Their location at the time of the decay is thus difficult to predict. In the present GERDA configuration we can divide the liquid argon into three physically separated volumes: *a)* inside the detector bore-holes; *b)* between the mini-shrouds and the germanium crystals; and *c)* outside the mini-shrouds. Decays in the last volume cannot generate beta-events because the distance from the detector is much larger than the attenuation length of beta-rays. Only the first two volumes are thus considered in this analysis.

The region inside the bore-hole is field-free since all the surrounding surfaces are on a equal potential, i.e. the p+ electrode and Chinese-hat (see Figure 2.2). The ^{42}K distribution is expected to be homogeneous in this LAr volume, although van der Waals forces could in principle collect part of the ions on the detector surface. To scrutinize both options, we first simulated decays uniformly distributed in the LAr, and then confined on the p+ electrode surface. The simulation has been normalized using the ^{42}K activity given in Ref. [75] ($92.8_{-5.1}^{+5.3} \pm 4.5 \mu\text{Bq/kg}$), the total volume of LAr present in the bore-hole of the six detectors ($\sim 7.45 \cdot 10^{-2} \text{ l}$) and the experimental life time (165 days). The total number of expected decays is 127.

The space between the detector n+ electrodes (HV electrode) and the grounded surface of the mini-shrouds is instead characterized by a strong electric field (order of kV/cm). The maximal number of beta-events from the n+ electrode has been computed assuming that all the ^{42}K present in the mini-shrouds is collected by the electric field on the n+ electrode surface of the detectors. Also in this case the activity is normalized according to the life time and the total volume of LAr in the three mini-shrouds ($\sim 7.63 \text{ l}$), giving an expectation of 8643 decays. The number of ^{42}K beta-events close to the groove is assumed to be negligible

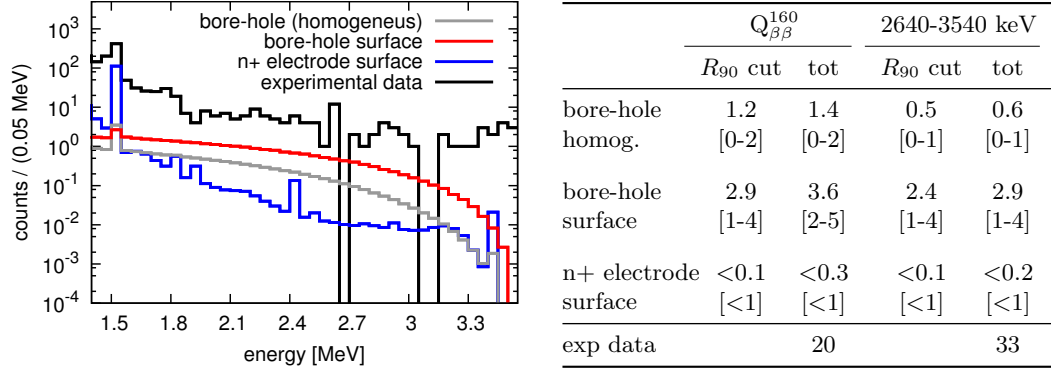


Figure 3.7: (Left) Experimental energy spectrum and simulated ^{42}K contributions for different decaying locations. The 1525 keV gamma-line of ^{42}K in the experimental data is dominated by the decays outside the mini-shroud. (Right) Expected number of counts in the $Q_{\beta\beta}^{160}$ and 2640-3540 keV regions. The values are provided for the total number of counts and the beta-events surviving the R_{90}/R_{90}^d cut. The smallest integer interval containing $\geq 68\%$ probability is reported in square brackets (the first and last integers of the interval are quoted). The interval is computed assuming Poisson statistics and following the procedure discussed in Ref. [76]. Upper limits are provided when the interval contains only 0.

according to the experimental hints collected from GERDA during the commissioning phase and from the LArGe setup.

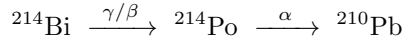
The plot in Figure 3.7 shows the experimental data and the ^{42}K simulated spectra normalized to the exposure of 6.1 kg·yr. The table summarizes the expected rates in the $Q_{\beta\beta}^{160}$ window and for the high-energy region between 2640 and 3540 keV in which only alpha- and beta-events are energetically allowed. The values are provided before and after applying the R_{90}/R_{90}^d cut. The events rejected by the cut are potential gamma-events. Their amount is smaller than one count in all the scenarios simulated, indicating that the contribution due to gamma-rays is not dominant when the decay occurs near the detector. The events surviving the cut are hence beta-induced events. The estimated count rate of beta-events from ^{42}K decaying in the bore-hole is a significant fraction of the total GERDA background, 6% or 15% according to the scenario considered (1.1 or 2.9 over 20 counts). Conversely, the contribution of ^{42}K decaying on the n+ electrode from the mini-shroud volume (beta- and gamma-events) is constrained to $< 1/20$ ($< 5\%$) and it will be neglected in the following discussion. These results cannot be extended directly to Phase II detectors, because of the different electrode geometry and dead layer thicknesses.

^{214}Bi beta-induced background

^{214}Bi is a short-lived beta-emitting isotope (Q-value = 3270 keV, $T_{1/2} = 19.8$ m) occurring in the radioactive decay chains of ^{226}Ra ($T_{1/2} = 1622$ yr). ^{214}Bi decays can occur either inside the materials, where the primary ^{226}Ra contamination is located, or in the liquid argon. In

fact, an intermediate isotope of the decay chain is ^{222}Rn , a noble gas with $Q\text{-value} = 5590\text{ keV}$ and $T_{1/2} = 3.8\text{ days}$. ^{222}Rn is a mobile element and its decay location can be distant from the production site. In particular, it can be transported throughout the GERDA liquid argon volume by convection flows. The location of the ^{214}Bi decays in the GERDA setup has been studied in Ref. [77] comparing the relative intensity of its gamma-lines with Monte Carlo simulations. The present data favor scenarios in which ^{214}Bi decays occur close to the detector array (mini-shroud, LAr, holders/cables or n+ electrode), but the precise location cannot be conclusively determined with the present exposure.

In this analysis two ^{214}Bi distributions have been considered: on the n+ electrode and on the p+ electrode surface. The scenarios considered provide the highest beta-event count rate and, consequently, can be used to set upper limits. The activity on the n+ electrode surface has been normalized to match the measured intensity of the 1764 keV gamma-line (equivalent to 2934 decays). This specific gamma-line has been chosen because of its vicinity to $Q_{\beta\beta}$ and highest signal to background ratio (24 counts in the region of interest with 1 background event expected, see Table 2.2). The activity on the p+ electrode has been instead estimated using the number of events above 6.2 MeV expected by the decays of ^{214}Po , daughter of ^{214}Bi . The application of the previous approach to this scenario provides a simulated spectrum which is incompatible with the experimental count rate in several energy regions, in particular the peak-to-continuum ratio is significantly smaller for several gamma-lines. ^{214}Bi on the p+ electrode can hence only marginally contribute to the intensity of the 1764 keV gamma-line. ^{214}Po undergoes alpha-decay shortly after the ^{214}Bi decay ($T_{1/2} = 164.3\text{ }\mu\text{s}$ [69]), generating the characteristic cascade:



Its signal should hence be present in case of a ^{214}Bi contamination on the p+ electrode surface. Because of its high $Q\text{-value}$ (7.8 MeV), ^{214}Po is the only element in the ^{238}U decay chain that can create events above 6.2 MeV. In the present data set, 4 counts exceed this energy threshold and only one of them occurs $\lesssim 1\text{ ms}$ after a lower-energy signal in the same detector (compatible with a Bi-Po coincidence). The normalization of the ^{214}Bi activity on the p+ electrode has been conservatively performed with respect to the four events, resulting in an expectation of 8.9 decays in 6.1 kg·yr.

The simulated spectra are shown in the plot of Figure 3.8 along with a table summarizing the upper limits on the total number of counts and on the amount of beta-events computed applying the R_{90}/R_{90}^d cut. The beta-event count rate on the p+ electrode is negligible and the upper limit is < 1 count in the $Q_{\beta\beta}^{160}$ window assuming Poisson statistics and 68% probability interval. The expected number of n+ electrode beta-events – computed for the scenario providing the highest count rate – is 2.1 ($\sim 10\%$ of the total) and the upper limit

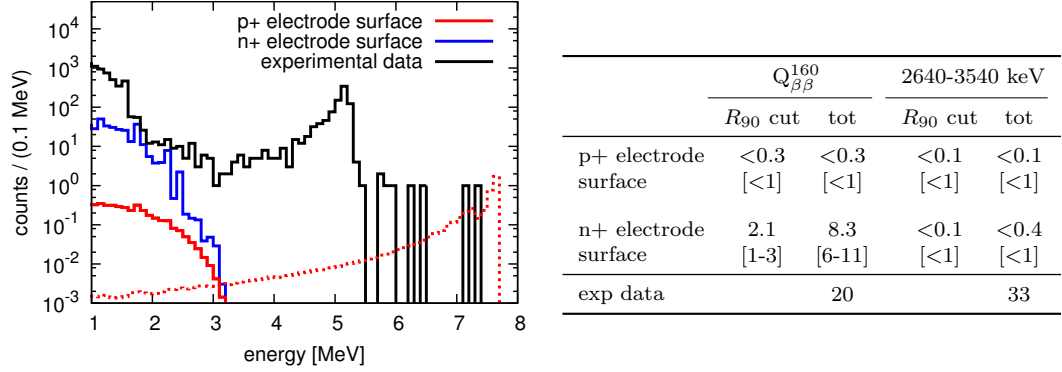


Figure 3.8: (Left) Experimental energy spectrum and simulated ^{214}Bi contributions for different decaying locations. The dotted line shows the energy distribution of ^{214}Po used to normalize the ^{214}Bi activity on the p+ electrode. (Right) Expected number of counts in the $Q_{\beta\beta}^{160}$ and 2640-3540 keV regions. The values are provided for the total number of counts and the beta-events surviving the R_{90}/R_{90}^d cut. The smallest integer interval containing $\geq 68\%$ probability is reported in square brackets (the first and last integers of the interval are quoted). The interval is computed assuming Poisson statistics and following the procedure discussed in Ref. [76]. Upper limits are provided when the interval contains only 0.

is < 4 counts. However, the real value is likely to be lower also because the R_{90} cut accepts 10-15% of the gamma-events.

3.3.2 Statistical analysis of the gamma-induced background

The total gamma-event count rate at $Q_{\beta\beta}$ has been evaluated using the amount of gamma-events above the rt_{5-50} threshold and applying a correction based on their cut acceptance derived from ^{228}Th calibration data (see Section 3.2.3). Given the results of the previous sections, we expect that the number of counts above the rt_{5-50} threshold (11 counts, see Table 3.3) is mainly due to gamma-events. The other potential contributions are n+ electrode beta-events (< 1 counts for ^{42}K and < 4 counts for ^{214}Bi) and alpha- and beta-events on the p+ electrode and groove surface (0.45 counts considering that the cut efficiency is 95% and the number of events below the cut threshold is 9).

The statistical model used for this analysis assumes that the amount of counts above the threshold is given by the sum of two contributions. The first one is a Poisson distribution with expectation equal to the total number of gamma-events, corrected for the mass-weighted acceptance of gamma-events above the rt_{5-50} cut threshold (73%). The second contribution is a Poisson distribution with expectation 0.5 counts (sum of the expectation for alpha- and ^{42}K events). The model has been implemented as a dedicated application based on the BAT [78] toolkit and solved using a Bayesian approach. The most likely value and the

corresponding 68% probability interval is:

$$N_{\gamma\text{-events}} = 14.7^{+4.8}_{-4.4}$$

The computation has been repeated assuming that ^{214}Bi decays are concentrated on the detector n+ surface (2.1 beta-events in $Q_{\beta\beta}^{160}$). In this case, the Poisson distribution accounting for the background components has an expectation of 2.6 counts (0.5 from alpha and ^{42}K events plus 2.1 counts from ^{214}Bi) and the result is $N_{\gamma\text{-events}} = 11.0^{+5.6}_{-3.6}$.

The gamma-induced background in the region of interest is due to the combined contribution of ^{208}Tl , ^{214}Bi and ^{42}K . The fraction of gamma-events induced by ^{42}K decays in the mini-shroud is negligible according to the simulations presented in Section 3.3.1. The count rate expected by decays outside the mini-shroud is also very low ($\lesssim 1$ count according to the analysis discussed in Ref. [75]). ^{214}Bi gamma-rays are instead expected to account for 50-60% of the events for decays nearby the detectors. As discussed in Ref. [77], the count rate in the $Q_{\beta\beta}^{160}$ region is weakly dependent on the scenario simulated when the spectra are normalized to match the intensity of the high-energy gamma-lines (1764 and 2204 keV). Given the low expectation for ^{42}K gamma-events and the absence of other candidates, we assign the remaining counts (40-50% of the total) to ^{208}Tl decays. This number of counts has been compared with the expectations for far and close sources. The former was extracted from the ^{228}Th spectra measured in calibration runs. The latter from simulations of ^{208}Tl decays in the top part of the cryostat (taken from Ref. [79]). Both values were taken normalizing the 2615 keV gamma-line intensity. Our result was found to lie between the count-rate expectations of the two scenarios and, within the uncertainties, to be compatible with ^{208}Tl decays in proximity of the detector array.

3.3.3 Spectral fitting of ^{210}Po degraded alpha-events

In the considered data set, the high-energy part of the GERDA background spectrum is dominated by a peak at 5.3 MeV which is traceable back to ^{210}Po decaying on the detector p+ electrode or groove surfaces (the data match both the Q-value and the half-life). The left side of the peak shows a strong tail extending to lower energies due to degraded ^{210}Po alpha-events. The contribution of other alpha-emitting isotopes seems to be negligible given the low count rate above 5.4 MeV and the lack of other structures in the energy spectrum that would be expected in case of decays on the detector surface. However, a contamination of ^{222}Rn in liquid argon would generate an almost uniform distribution of events below 5.5 MeV, extending with a reduced count rate up to 7.7 MeV. This potentially relevant background component cannot be assessed with the present data set because of the high ^{210}Po count rate below 5.3 MeV and the low counting statistics at higher energies. The study of this component will be possible in the next future thanks to the increment of

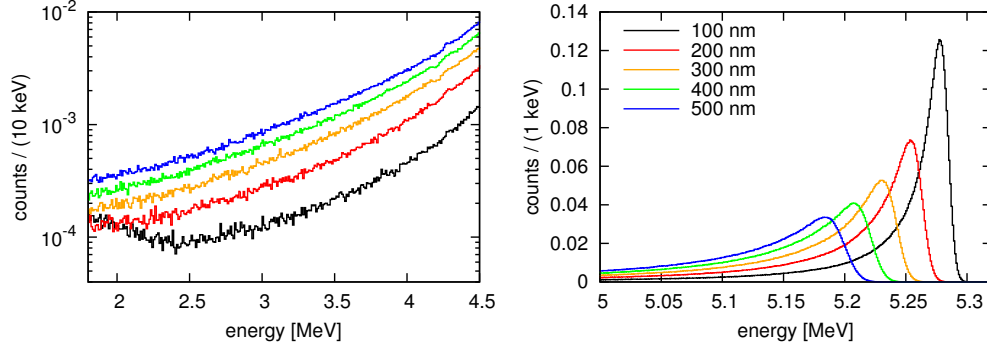


Figure 3.9: Simulated energy distributions of ^{210}Po decaying on the surface of the p+ electrode for different values of the dead layer thickness. The nominal value is 300 nm for the GERDA coaxial detectors.

exposure and reduction of the ^{210}Po activity expected by its relatively short half-life (138 days).

The shape of the energy spectrum induced by a pure alpha-emitting isotope decaying on a detector surface is influenced only by two parameters: the thickness of the dead layer and the implantation profile. Their impact has been investigated in Ref. [80] for ^{210}Po using MC simulations. A selection of the simulated spectra for different dead layer thicknesses is shown in Figure 3.9. In general, the energy distributions differ significantly in the peak region while, at lower energies (2 – 4.5 MeV), the shape is almost indistinguishable for dead layer thicknesses in the range 200-400 nm around the nominal value provided by the manufacturer (300 nm). The possibility of comparing the simulated spectra with the experimental data in the peak region and constrain the parameter values has been considered in Ref. [80]. However, the energy calibration is performed according to second order polynomial functions whose parameters are defined using the ^{208}Tl gamma-lines (highest energy gamma-line at 2.6 MeV). In the alpha range, the calibration is an extrapolation and the systematics uncertainties can reach a few tens of keV. In comparison, changing the dead layer of 100 nm results in a shift of the spectrum maximum equal to 20-30 keV.

For this reason, the approach pursued in this analysis focuses on the tail of degraded alpha-events exploiting its feature of being weakly dependent of the dead layer thickness and implantation profile. The experimental spectrum is fitted with the simulated ones in the energy range between 3.5 and 4.2 MeV. The lower edge corresponds to the ^{42}K beta-spectrum end point ensuring that no beta- or gamma-events are present in the fit region. The upper edge is chosen to maximize the statistics while staying in the energy range where the shape of the energy distributions is similar. The fit has been performed in BAT using a binned maximum likelihood approach. The number of events in each bin are assumed to fluctuate independently according to a Poisson distribution. The reference bin

width used in the following analysis is 100 keV, however the fit proved to be stable against changes in this parameter. The fit is performed using only the events below the rt_{5-50} cut threshold for a direct comparison with the results of the pulse shape analysis.

Figure 3.10 shows the experimental data superimposed to the spectra simulated assuming the dead layer thickness provided by the manufacturer (300 nm). The decay distribution is assumed for simplicity to be homogeneous on the p+ electrode surface. This parameterization is taken as reference in the analysis and proved to describe accurately the data (p-value of 0.6 in the fit range 3.5-4.2 MeV). The normalized MC spectrum is thus used to extrapolate the alpha-induced background in the region of interest and in a control region between 2640 and 3540 keV. According to the results of Section 3.3.1, the background in the control region is expected to be dominated by degraded alpha-events with a small contamination of ^{42}K and ^{42}Bi . Figure 3.11 shows a table summarizing the extrapolation results and a graphical comparison of the values. The uncertainties are provided summing in quadrature the contributions due to:

- Model parameterization. The fit has been repeated using the simulated spectra obtained for dead layer thickness between 100 and 500 nm and different implantation profiles (step functions and exponential distribution penetrating up to a few hundred nm inside the p+ electrode surface). Each parameterization has been used to extrapolate the count rate in the two regions and the maximum deviation is used as uncertainty. The uncertainty is dominated by the parameterization with 100 nm dead layer whose spectrum has a bump at $Q_{\beta\beta}$ (see Figure 3.9).
- Fit range. The fit has been repeated shifting the energy window of ± 100 keV and the uncertainty is given as the maximum spread between the extrapolated count-rate values.
- Statistical fluctuations. The upper and lower bounds of the 68% probability band around the global fit have been propagated to the count-rate extrapolations and used as statistical uncertainties.

In addition to the fit extrapolations, Figure 3.11 shows the experimental count rate below the rt_{5-50} cut. The values in the $Q_{\beta\beta}^{160}$ window are corrected for the expected amount of gamma-events using a statistical model similar to the one discussed in Section 3.3.2 (the gamma-events are now subtracted from the amount of counts below the cut threshold instead of summed up). The model is described in detail in Appendix C.1.2.

The total number of events observed in the control region (2640-3540 keV) for ANG2 and ANG5 is well reproduced by the ^{210}Po tail, coherently with the limits set on the ^{42}K and ^{214}Bi count rate. The experimental count rate of ANG3 is higher than the fit extrapolation, but still compatible within the uncertainties. This supports the validity of the fitting approach applied in this analysis. The expected rate at $Q_{\beta\beta}$ is however systematically

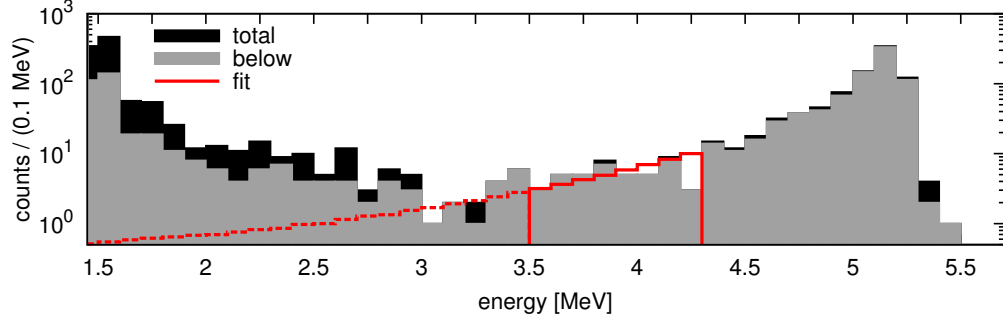


Figure 3.10: Experimental energy spectrum and distribution of the events reconstructed below the rt_{5-50} cut threshold. The best fit with a simulated spectrum (computed in the region 3.5-4.2 MeV) is superimposed to the data.

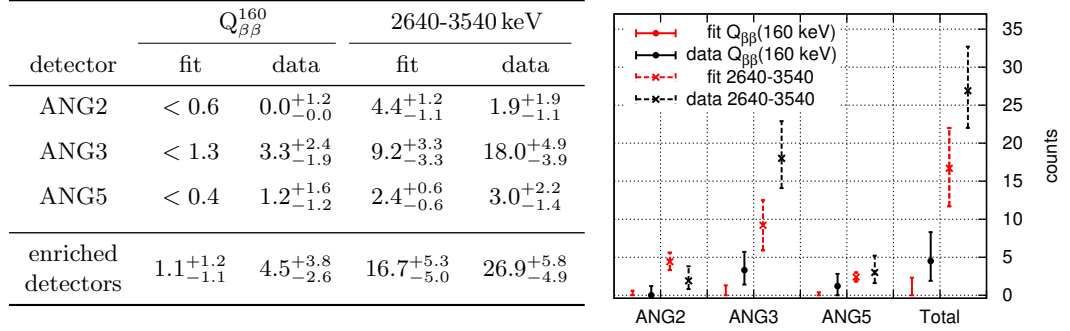


Figure 3.11: Number of events below the rt_{5-50} cut threshold in the $Q_{\beta\beta}^{160}$ and 2640-3540 keV regions. The values in the $Q_{\beta\beta}^{160}$ window are corrected assuming that 27% of the total number of gamma-events is reconstructed below the cut threshold. The experimental value is compared with the expected ^{210}Po background extrapolated by the fit. The values are provided for the detectors with high count rate in the ^{210}Po peak and for the sum of all the six enriched detectors. The results are given quoting the most likely value and the smallest interval containing 68% probability.

lower than the measured one in all the detectors. The total number of events expected by ^{210}Po ($1.1^{+1.2}_{-1.1}$ counts) is 25% of the observed amount ($4.5^{+3.8}_{-2.6}$). The values are not incompatible considering the uncertainties, but the results suggest that the ^{210}Po peak tail cannot account for the total number of p+ electrode and groove surface interactions. The observed background count rate is well explainable considering also the expectation for ^{42}K beta-events on the p+ electrode (between 0 and 4 counts according to the scenario considered). This results are consistent with the limits set on ^{214}Bi p+ beta-events (< 1 counts).

Table 3.4: Decomposition of the GERDA Phase I background. Each radioactive isotope contribution is separated according to the decay position and type of particle emitted. The uncertainties are given for the 68% probability interval. Given the width of the $Q_{\beta\beta}$ window (160 keV) and the exposure of the data set (6.1 kg · yr), the number of counts is practically equal to the background index expressed in units of 10^{-3} cts/(keV · kg · yr) (conversion factor 1.02).

Event	Type	Event Location	Method	cts in $Q_{\beta\beta}^{160}$		Notes
^{42}K	β	bore-hole homog.	MC	1.2	[0-2]	
		bore-hole surface		2.9	[1-4]	
		n+ surface		<0.1	[<1]	
^{214}Bi	β	p+ surface	MC	<0.3	[<1]	overestimated
		n+ surface		2.1	[1-3]	overestimated
^{214}Bi						$\sim 50\text{-}60\%$
^{208}Tl	γ	full volume	PSA	$14.7^{+4.8}_{-4.4}$ ($11.1^{+5.6}_{-3.6}$)		$(\sim 40\text{-}50\%)$
^{42}K						
^{210}Po	α	p+ surface	MC+fit	$1.1^{+1.2}_{-1.1}$		$T_{1/2} = 138$ d
<i>sum of the best values</i>				17.2 (15.5)		^{42}K bore-hole hom.
				18.9 (17.4)		^{42}K bore-hole surf.
<i>experimental counts</i>				20		

3.3.4 Overview

The combined results presented in the previous sections provide a first decomposition of the GERDA Phase I background. The number of background counts assigned to each component is summarized in Table 3.4. The high-energy gamma-rays produced in the decay of ^{214}Bi , ^{208}Tl and ^{42}K have been identified as the major component of the background at $Q_{\beta\beta}$. Their combined count rate accounts for $\sim 70\%$ of the background in the region of interest ($\sim 56\%$ assuming a strong ^{214}Bi contamination on the detector n+ surface). The remaining counts are shared between ^{42}K beta-events (10-20%) and ^{210}Po degraded alpha-events (5%). These three components can explain the measured background at $Q_{\beta\beta}$, limiting the room for additional sources, including ^{214}Bi n+ beta-events.

Assuming a negligible contamination of ^{214}Bi on the n+ surface, the sum of the best values estimated for each component is 17.2 or 18.9 (according to the ^{42}K distribution inside the bore-hole). For a maximal ^{214}Bi contamination on the detector n+ surface, the sum is 15.5 and 17.4 (depending on the ^{42}K distribution).

It should be mentioned that, according to new results obtained after this work, ^{222}Rn daughters decaying in LAr would contribute to the background at $Q_{\beta\beta}$ with a total count rate of $\sim 1.5 \cdot 10^{-3}$ cts/(keV · kg · yr) [81]. Such contribution does not affect the results reported in this chapter. The total number of counts expected by the background model

of Table 3.4, with the additional contribution of ^{222}Rn daughters (~ 1.5 counts), is well compatible with the data within the uncertainties.

3.4 GERDA Phase I sensitivity

In the previous sections, the GERDA Phase I background has been studied using the rt_{5-50} pulse shape analysis and Monte Carlo simulations. The total background count rate at $Q_{\beta\beta}$ has been quantitatively decomposed according to the background source and interaction location inside the detectors. In this section, we estimate the average $0\nu\beta\beta$ life time limit achievable by GERDA as a function of exposure, assuming different background indices and $0\nu\beta\beta$ detection efficiencies. Besides computing the sensitivity for the current background index ($\text{BI} = 20^{+6}_{-4} \cdot 10^{-3} \text{ cts}/(\text{keV} \cdot \text{kg} \cdot \text{yr})$), we investigate the potential improvements deriving from the reduction of specific background components through pulse shape analysis. The expected variations of the background index are computed using the background model summarized in Table 3.4.

The background rejection through pulse shape analysis can be obtained in two ways: *a)* discriminating single-site interactions (expected by the $0\nu\beta\beta$ signals) from multiple-site interactions (due to gamma-rays); *b)* identifying the interaction-site location and applying a fiducial-volume cut inside the detector (e.g. the rt_{5-50} method).

The former approach has been already used in the Heidelberg-Moscow and IGEX experiments. The best performance achieved with HPGe detectors corresponds to a survival probability at $Q_{\beta\beta}$ of 30% for gamma-events and 90% for $0\nu\beta\beta$ -like events [71, 82]. These values, which can be considered as theoretical limits for GERDA Phase I detectors, would reduce the BI to $\sim 10 \cdot 10^{-3} \text{ cts}/(\text{keV} \cdot \text{kg} \cdot \text{yr})$ (see Table 3.5, *cut a*).

The second approach can be used if the background count rate is not distributed homogeneously within the detector. In the present data set, for instance, we identified several background components creating localized interactions on the p+ electrode and groove surface. An ideal volume cut around the p+ electrode could reduce the BI to $\sim 16 \cdot 10^{-3} \text{ cts}/(\text{keV} \cdot \text{kg} \cdot \text{yr})$ (see Table 3.5, *cut b1*) discarding a negligible fraction of the volume. An other illustrative volume cut is the rt_{5-50} method previously discussed. The fiducial volume defined accepting only the events above the cut threshold is, with the present calibration, 68% of the total. The volume discarded is the region close to the bore-hole and groove. The $0\nu\beta\beta$ detection efficiency is also decreased to 68% after the cut, coherently with the fraction of volume loss. The cut rejects 95% of the alpha- and beta-events on the p+ electrode and groove surface as well as a fraction of the gamma-events. On the present data set, the cut reduces the total background index to $11 \cdot 10^{-3} \text{ cts}/(\text{keV} \cdot \text{kg} \cdot \text{yr})$ (*cut b2* in Table 3.5). It should be noted the rt_{5-50} parameter was originally developed as a tool to study the various background components and aims at being simple and robust rather than minimizing the volume loss.

Table 3.5: Decomposition of the GERDA Phase I background according to the topology and location of the interaction sites and BI expected when a specific background component is suppressed by pulse shape analysis. The total BI of the data set is $20_{-4}^{+6} \cdot 10^{-3}$ cts/(keV·kg·yr).

Event Location	Event Type		cts in $Q_{\beta\beta}^{160}$	survival probability		
				<i>cut a</i>	<i>cut b1</i>	<i>cut b2</i>
n+ surface	^{42}K	β	<0.1	100%	100%	100%
	^{214}Bi	β	2.1			
p+ electrode or groove surface	^{42}K	β	1.2 / 2.9	100%	0%	5%
	^{214}Bi	β	<0.3			
	^{210}Po	α	$1.1_{-1.1}^{+1.2}$			
full volume	^{214}Bi			30%	100%	73%
	^{208}Tl	γ	14.7 / 11.1			
	^{42}K					
<i>total BI assumed after cut</i> [10^{-3} cts/(keV·kg·yr)]				10	16	11
<i>$0\nu\beta\beta$ signal survival probability</i>				90%	100%	68%

Figure 3.12 shows the sensitivity curves of the average $0\nu\beta\beta$ half-life ($T_{1/2}^{0\nu}$) as a function of the exposure computed for the background indices and cut efficiencies discussed above and summarized at the bottom of Table 3.5. The computation has been performed using the software developed by A. Caldwell and assuming: 87% ^{76}Ge enrichment, 85% detector active volume and 4.6 keV resolution at $Q_{\beta\beta}$. The limits are provided at 90% probability. The dimensions of the energy window used to search for an excess of events are optimized with respect to the sensitivity.

The average limit expected with an exposure of 20 kg·yr (foreseen for spring 2012) without the application of any cut is $T_{1/2}^{0\nu} > 1.9 \cdot 10^{25}$ yr. At the background level of GERDA Phase I, the sensitivity is not significantly improved by the BI reduction achievable by pulse shape analyses, especially if this is obtained at the cost of reducing the $0\nu\beta\beta$ detection efficiency. The average half-life limit after applying *cut a* and *b1* is $T_{1/2}^{0\nu} > 2.0 \cdot 10^{25}$ yr and $T_{1/2}^{0\nu} > 2.1 \cdot 10^{25}$ yr respectively, only $\sim 6\%$ higher than before. The sensitivity curve for *cut b2* (*rt₅₋₅₀* cut) is considerable lower than the others, indicating that the sensitivity is strongly affected by the $0\nu\beta\beta$ detection efficiency: the reduction of the signal acceptance to 68% is not compensated by a BI improvement of a factor 2.

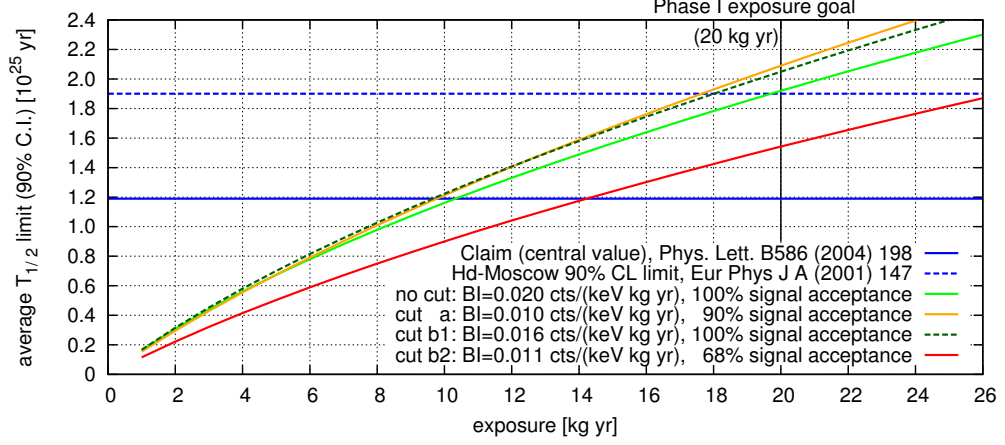


Figure 3.12: GERDA Phase I sensitivity for the $0\nu\beta\beta$ half-life as a function of the exposure. The sensitivity curves are drawn for various values of the background index and of the $0\nu\beta\beta$ detection efficiency.

3.5 Conclusions

A new pulse shape analysis method for the identification of alpha- and beta-induced interactions on the surface of the p+ electrode or groove region was developed. The method is based on the rise time of the charge pulses between 5% and 50% of the maximum amplitude and is tuned using the pure sample of high-energy alpha-induced events. The method has been designed and benchmarked using both simulated and experimental data and proved to be robust and efficient on the GERDA Phase I detector signals.

The pulse shape analysis was used along with Monte Carlo simulations to decompose the GERDA background in the region of interest. The considered data set includes the run from 25 to 32 (total exposure of 6.1 kg·yr) and has an average background index of $20^{+6}_{-4} \cdot 10^{-3}$ cts/(keV·kg·yr). High-energy gamma-rays produced in the decay of ^{214}Bi , ^{208}Tl and ^{42}K were identified as the major component of the background at $Q_{\beta\beta}$. The estimated total count rate is $14.7^{+4.8}_{-4.4} \cdot 10^{-3}$ cts/(keV·kg·yr), equally shared between ^{214}Bi and ^{208}Tl with a small contribution from ^{42}K . The gamma-ray count-rate estimate is reduced to $11.1^{+5.6}_{-3.6} \cdot 10^{-3}$ cts/(keV·kg·yr) in case of a strong ^{214}Bi contamination on the detector n+ surface. Secondary background components are ^{210}Po alpha-decays, $1.1^{+1.2}_{-1.1} \cdot 10^{-3}$ cts/(keV·kg·yr), and ^{42}K beta-induced interactions, expected value 1.2 or $2.9 \cdot 10^{-3}$ cts/(keV·kg·yr) according to the scenario considered. The ^{214}Bi beta-induced background is constrained to $< 4 \cdot 10^{-3}$ cts/(keV·kg·yr).

Given the obtained background decomposition, we estimated the impact of pulse shape discrimination techniques on the $0\nu\beta\beta$ average half-life limits achievable by GERDA Phase I. The improvement expected for an optimal rejection of multiple-site events with an exposure

of 20 kg·yr is of 6%, from $T_{1/2}^{0\nu} > 1.9 \cdot 10^{25}$ yr to $T_{1/2}^{0\nu} > 2.1 \cdot 10^{25}$ yr. The rejection of surface alpha- and beta-events on the p+ electrode and groove surface could provide similar results if the $0\nu\beta\beta$ detection efficiency is extremely close to 100%.

**GERDA Phase II: detector
development and off-line background
reduction techniques**

Chapter 4

Overview of the Phase II HPGe detector design and development

The GERDA experiment pursues a staged implementation. The goal of the current phase – scheduled for spring 2013 – is to scrutinize the claim for a positive $0\nu\beta\beta$ detection of Ref. [34] with a total exposure of 20 kg·yr. The following phase (GERDA Phase II) aims at exploring half-lives $> 10^{26}$ yr, accumulating 100 kg·yr of exposure with a background index $\lesssim 10^{-3}$ cts/(keV·kg·yr). To reach such background levels – which are more than an order of magnitude below the current value – the collaboration plans to operate ~ 30 additional custom-made detectors (~ 20 kg of ^{76}Ge) with a new electrode geometry, providing superior pulse shape discrimination performances. In addition, new devices will be installed to identify energy depositions in the liquid argon surrounding the detector array, through the detection of the induced Ar scintillation light. These events are due to background sources and their detection, in coincidence with a Ge detector signal, can be used as anti-Compton or anti-coincidence veto.

The detector design adopted for GERDA Phase II is based on a commercial product offered by Canberra Semiconductor [83], referred to as Broad Energy Germanium (BEGe) detectors [49]. BEGe detectors are p-type HPGe detectors with a cylindrical shape and a small B-implanted p+ read-out electrode located on one of the flat surfaces. Typically, the Ge crystal has a diameter between 65 and 80 mm and a thickness between 25 and 40 mm. A Li-diffused n+ electrode – between 0.4 mm and 0.8 mm in the “thick window” modification used by GERDA – covers the rest of the outer surface and is separated from the p+ electrode by a circular groove. The positive high voltage is applied to the n+ electrode (operational voltage between 3 and 4 kV) while the read-out electrode is grounded. A schematic drawing of a typical BEGe detector is shown in Figure 4.1.

This electrode geometry results in a peculiar charge collection mechanism that allows to distinguish between single-site events ($0\nu\beta\beta$ like) and multiple-site events (typical of

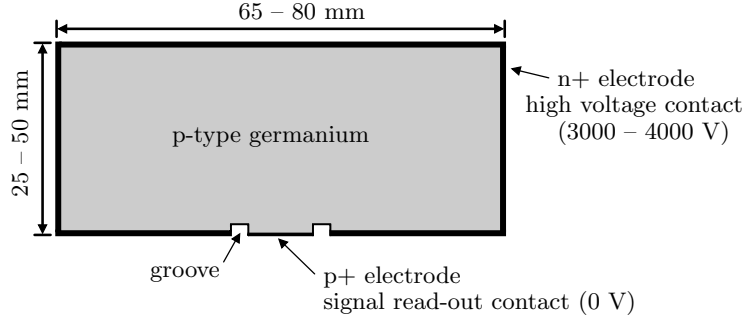


Figure 4.1: Vertical section of a BEGe detector showing the electrode scheme and the standard crystal dimensions. The signal read-out electrode and the groove geometry are proprietary information of Canberra Semiconductor and are not drawn to scale.

gamma-ray induced backgrounds) through the analysis of the signal time structure. Recent results – achieved in the framework of this dissertation and discussed in Chapter 6 – showed that also events on the surface of BEGe detectors can be efficiently rejected using pulse shape analysis techniques. An additional benefit of the small size of the read-out electrode is the low capacitance of the detector. This yields a lower noise and, consequently, a superior resolution and a lower threshold compared to other types of large-volume HPGe detectors.

Historically, the advantages of a reduced electrode size were recognized already in the 1980s [84]. In 2005, a p-type HPGe detector with a point-like read-out electrode was built by Canberra Industries and its performances (published in 2007 in Ref. [85]) drew new attention on this electrode geometry and on its suitability for $0\nu\beta\beta$ experiments. These results triggered discussions between S. Schönert (GERDA collaboration) and J. Verplancke (Canberra Semiconductor N.V. Olen) leading to the idea that commercial BEGe detectors should have an electric field – and hence pulse shape features – similar to the prototype of Ref. [85]. A first custom BEGe detector (“thick window” modification) was ordered in fall 2007 to study its pulse shape discrimination capability and the first promising results were already presented in 2008 [86]. The encouraging results achieved during the following study of several prototype BEGe detectors and pulse shape simulations – to which the author contributed at various steps – brought the GERDA collaboration to adopt in 2011 the BEGe detector design as baseline for the second phase of the experiment. Meanwhile, also the MAJORANA collaboration investigated a variety of detector geometries including the BEGe detector design offered by Canberra, finally adopted as baseline design for their demonstrator [87]. The milestones achieved during the GERDA BEGe detector R&D are summarized in the following.

- The characterization of two commercial BEGe detectors confirmed the expected optimal spectroscopic performances (energy resolution, energy threshold and stability). The author participated in the characterization of the second detector. The results

have been published in Refs. [88, 89, 90, 91, 92]. Both the detectors were characterized in vacuum-cryostat using the integrated charge sensitive preamplifier provided by the manufacturer. The deviation from linearity measured using commercial analogue and digital data acquisition systems were found to be below 0.1% in the energy range from zero up to 3 MeV. The measured energy resolutions are very close to the physical limits of HPGe detectors and are among the best values reported in literature for this kind of detection technology. The resolution as a function of the energy deposition measured with the detector tested by the author is shown in Figure 4.2, using the gamma-lines of several calibration sources (^{241}Am , ^{60}Co , ^{228}Th)

- The feasibility of distinguishing single-site from multiple-site events through pulse shape analysis has been proved by D. Budjáš and co-workers using a novel and efficient pulse shape analysis technique (A/E method) [88, 89]. The reported survival probabilities in the $Q_{\beta\beta}$ region are 0.93% for ^{60}Co background, 21% for ^{226}Ra and $\sim 40\%$ for ^{228}Th . These results are achieved for a $\sim 90\%$ acceptance of $0\nu\beta\beta$ -like events (determined using the double escape events of the 2.6 MeV gamma-line of ^{208}Tl).
- The surface treatment developed for Phase I detectors showed to be suitable also for long-term operations of BEGe detectors in liquid argon [93, 94, 95].
- A full and comprehensive modeling of the BEGe detector response to charged particle and gamma-ray interactions has been developed by the author and co-workers to study in detail the charge collection mechanism. The modeling has been validated and then used to investigate pulse shape discrimination performances for decays occurring inside the detector volume and difficult to assess experimentally ($0\nu\beta\beta$ and cosmogenic ^{60}Co and ^{68}Ge). The topic is presented in Chapter 5 and Section 6.1. These results have also been published in Ref. [71].
- The viability of producing BEGe detectors from isotopically modified Ge has been demonstrated using germanium material depleted in ^{76}Ge . This material was left over by the production of the enriched germanium that, subsequently, has been used to produce the Phase II detectors. The production of BEGe detectors from depleted Ge served as a test for Phase II detectors (the depleted material has the same chemical history of the enriched one) and as R&D for maximizing the mass yield in various production steps, e.g. zone refinement and crystal pulling. In total five BEGe detectors were produced and none of them showed deteriorated performances compared to detectors from standard Ge material. Part of this work has been published in Refs. [96, 97, 98]. This production campaign has been also used to study the impact of the electrode geometry on the detector performances and to define the best configuration for the Phase II enriched detectors. The author contributed to the optimization of the electrode design using simulations of the electric fields and

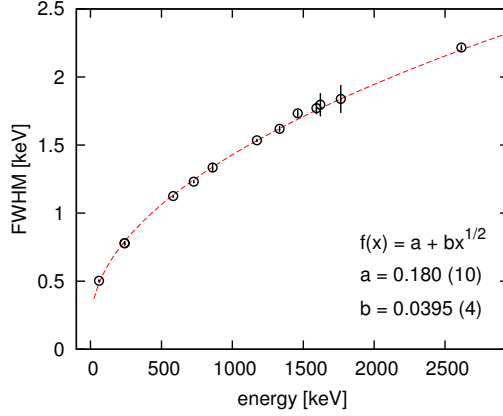


Figure 4.2: Energy resolution (full width half maximum, FWHM) as a function of the energy measured for a $^{\text{nat}}\text{Ge}$ BEGe detectors with an analogue data acquisition system. The data point are fitted with the parametrization discussed in Section 2.2.3. The characterization of this detector is discussed in Refs. [90, 92].

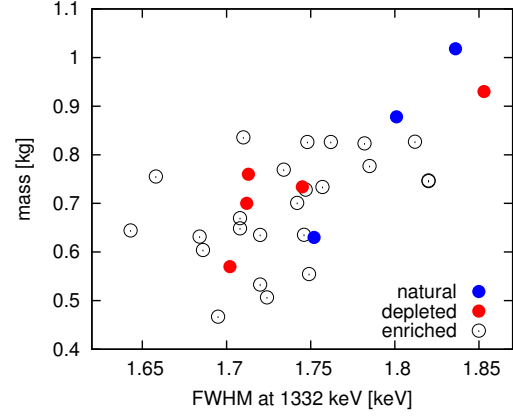


Figure 4.3: Resolution and mass of the BEGe detectors tested within the GERDA collaboration. The resolution is quoted with respect to the conventional 1332 keV gamma-line of ^{60}Co . The values are reported according to the manufacturer's specifications. Our measurements generally give values improved by $\gtrsim 0.1$ keV.

of the charge transportation. This topic is not discussed in this thesis because of a non-disclosure agreement with the manufacturer.

- The crystal pulling for Phase II detectors started in 2011 and the detector production in 2012. In total, 30 crystal slices have been produced and 29 were converted in diodes. Up to now, 27 of them have been operated as detectors showing performances within the specifications. One diode shows high leakage current and cannot be operated as a detector. The issue is still under investigation.
- The first prototype string with five enriched BEGe detectors was deployed in the GERDA setup in June 2012.

The reliability of an industrial large-scale production is shown in Figure 4.3, which reports the resolution as a function of the mass for all the detectors tested within the collaboration. It is remarkable that the detectors made from enriched and depleted material have the same performance of the detectors from natural Ge material. Note that the $^{\text{nat}}\text{Ge}$ detector with a $\gtrsim 1$ kg mass is a prototype specifically produced for GERDA to investigate the possibility of increasing the detector mass.

The second part of this dissertation focuses on the study of BEGe detectors and the development of off-line analysis techniques for background rejection. In the next chapter we will discuss the modeling of this detector and the correlation between charge collection and

pulse shapes. Chapter 6 covers the background rejection studies carried out in the framework of this thesis work. Finally, in Chapter 7, we will discuss the background expectation for GERDA Phase II combining the background modeling of Phase I discussed in the previous chapter and the performance of the background rejection techniques estimated in Chapter 6.

Chapter 5

Signal modeling

In this chapter we present a modeling of the signal formation in BEGe detectors. The simulation software developed to study the detector response to charged particle and gamma-ray interactions is described in Section 5.1. This tool is used in Section 5.2 to study the electric field and the consequent charge collection properties of the BEGe detector geometry. In particular, the detector response as a function of the interaction position and the number of interaction sites is investigated in detail. The comparison of the simulation results with experimental data is finally described in Section 5.3. The content of this chapter has been published in Ref. [71].

5.1 Overview of the simulation

The simulation discussed in this chapter aims at replicating all the physical processes involved in the formation and development of HPGe detector signals. It can be divided into three logical blocks (shown in Figure 5.1). The first one consists of a Monte Carlo simulation describing the transportation of gamma-rays and charged particles through matter. It provides the interaction points and the corresponding energy losses within the Ge crystal. This part of the simulation is performed with the MAGE framework [74], which is based on the GEANT4 simulation package [99, 100]. The second block describes the dynamics of the charge carriers generated in the interaction sites inside the detector and provides the signal induced on the read-out electrode by the charge drift towards the electrodes. It is calculated by using an enhanced version of the Multi Geometry Simulation (MGS) software [70]. The last block of the simulation accounts for the signal shaping of the read-out electronic devices and the electronic noise. The output signals of the simulation are hence directly comparable to the measured ones. In the following two subsections the second and the third block of the simulation are explained in detail.

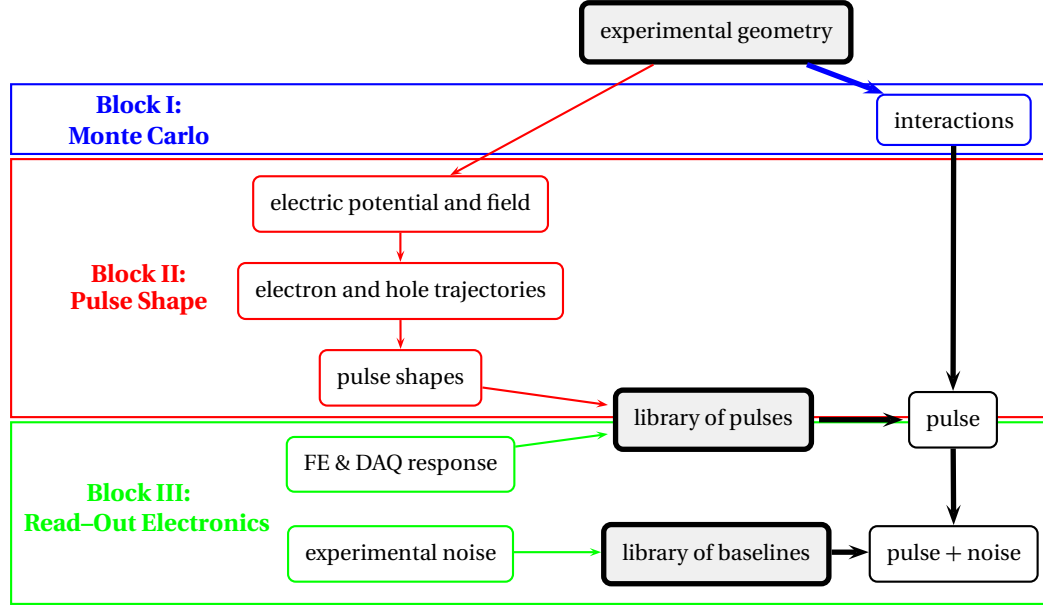


Figure 5.1: Data flow of the simulation organized into three logical blocks. The data flow includes a first phase (thin arrows) in which a library of pulses and baselines is created and a second phase (thick arrows) in which the libraries are used to generate the detector signals. In block III, FE & DAQ refers to the preamplifier and the sampling device.

5.1.1 Charge collection and signal formation

The pulse simulation performed with the MGS-based software (Block II in Figure 5.1) includes the following steps: *a)* computation of the electric field inside the detector at defined potentials of the electrodes; *b)* transport of charge carriers toward the electrodes; and *c)* time evolution of the signal induced at the read-out electrode by the moving charges.

Since a semiconductor detector can be considered as an electrostatic system, the electric field can be computed by solving the Maxwell equations or, equivalently, by solving the Poisson equation with a set of boundary conditions for the potential. In p-type HPGe detectors, the p–n junction forms between the p-type material (bulk volume) and the n+ electrode (~ 1 mm thick donor-doped surface layer). At operational bias voltages the p-type volume is fully depleted of free charges (active volume), while most of the n+ layer retains electrons in the conduction band (anode, forming a dead layer). This configuration is approximated in the simulation by defining in the active volume a negative space charge distribution ρ , proportional to the net p-type impurity concentration. The n+ electrode on which the bias voltage is applied is considered as a dead layer¹. The boundary conditions

¹Since the field calculation is performed on a 0.5 mm step grid, it can not describe the thin part of the n+ volume in which the conduction-band electrons are depleted (the n-side of the p–n junction, with positive space charge).

are then provided by the value of the potential on the conductive surfaces: V_{cathode} and V_{anode} . The system of equations to solve is:

$$\begin{cases} \nabla^2 \phi(\vec{r}) &= -\rho(\vec{r})/(\varepsilon_0 \varepsilon_r) \\ \phi|_{S_{\text{cathode}}} &= V_{\text{cathode}} \\ \phi|_{S_{\text{anode}}} &= V_{\text{anode}} \end{cases} \quad (5.1)$$

where \vec{r} is the position, $\phi(\vec{r})$ is the electric potential, $\rho(\vec{r})$ is the charge density distribution, ε_0 is the vacuum electrical permittivity, $\varepsilon_r \sim 16$ is the relative permittivity of Ge, $\phi|_S$ is the potential at the surface S surrounding the electrode under consideration.

The movement of charge carriers within the active volume is computed by using two phenomenological models [101, 102] which provide the drift velocity as a function of the electric field magnitude and direction relative to the crystallographic axes. We assume that each transfer of energy to the Ge crystal lattice results in the generation of a cloud of free electrons and holes, which subsequently drift as two independent clusters. The clusters are approximated in the simulation by two point-like charges with opposite sign. The trajectories are calculated with a fourth order Runge-Kutta method with 1 ns time step.

Using the simulated trajectories of charge carriers and the weighting potential² distribution inside the detector, the charge signal $Q(\vec{r}(t))$ induced on the electrodes is computed by using the Shockley-Ramo theorem [103]:

$$Q(\vec{r}(t)) = -q_{\text{tot}} \phi_w(\vec{r}(t)) \quad (5.2)$$

where $\vec{r}(t)$ is the position of the charge cluster at the time t , q_{tot} the total charge of the cluster and $\phi_w(\vec{r}(t))$ is the weighting potential.

The total signal of a simulated particle event composed of several interactions is calculated as a sum of pulses from each hit, whose position and energy deposition are provided beforehand with the MAGE Monte Carlo simulation. To reduce the computation time, the generation of the signals corresponding to the individual hits is performed using a library of pre-calculated pulses. The library is generated by dividing the detector active volume in 1 mm cubic cells, and simulating a mono-energetic point-like interaction at each corner. The library must be generated only once for each simulated detector geometry and bias voltage setting. Then, each Monte Carlo generated interaction is associated to one of the cubic cells in the pulse library. The signal is computed as the weighted average of the eight pulses associated to the cubic cell corners, where the weight is given by the inverse of the cubic euclidean distance between the interaction point and the considered corner. The amplitudes of the individual interaction pulses are then normalized according to the energy depositions

²The *weighting potential* is a dimension-less quantity defined as the electric potential calculated when the considered electrode is kept at a unit potential, all other electrodes are grounded and all charges inside the device are removed.

in the hits and all the pulses of the event are added up to one combined signal. The use of a pulse library decreases significantly the processing time of the simulation in such a way that the pulse computation time is comparable with that of the Monte Carlo simulation.

5.1.2 Read-out electronics response and noise

The read-out electronics includes the preamplifier and the digital sampling device. The response function was determined by providing the preamplifier input with an impulse generated by a high-precision pulser, and then by deconvolving the digitally sampled signal with the input signal. The simulated detector signals are convolved with this response function. This operation is performed for each pulse during the construction of the library. This computation is thus performed only once for each simulated experimental setup (see Block III in Figure 5.1).

To reproduce the electronic noise present in the experimental data, samples are taken from a library of experimentally recorded baselines. The amplitude of the noise is normalized according to the experimental signal-to-noise ratio, and the noise sample is then linearly added to the calculated full event signal.

The output of the simulation is a file resembling those recorded experimentally with a digital data acquisition system. It is hence possible to apply the same analysis tools to both experimental and simulated data.

5.2 Modeling of BEGe detectors

In this section, we first discuss the electric field features of BEGe detectors (Section 5.2.1) and then their correlation to the charge collection and the signal formation (Section 5.2.2). The results of the simulation are finally used in Section 5.2.3 to explain why single-site and multiple-site events can be discriminated analyzing the signal time structure.

The detector used for this study is a modified thick-window BEGe detector (BE3830/S model). The detector has the standard geometry and electrode scheme described in the previous chapter (see Figure 4.1). The Ge crystal has a diameter of 71 mm and a thickness of 32 mm. The experimental characterization of this detector is discussed in Refs. [90, 92].

5.2.1 The electric field inside BEGe detectors

The pulse shape discrimination properties of BEGe detectors have been attributed to the peculiar internal electric field which is created by the small size of the read-out electrode. In Section 5.1.1 the space charge distribution inside the active volume (equivalent to the net distribution of acceptor impurities) was identified along with the electrode potentials as a source of electric field inside the detector. To better understand the two contributions, the

linear superposition principle can be used to separate the potential into the two individual components:

$$\phi(\vec{r}) = \phi_0(\vec{r}) + \phi_\rho(\vec{r}) \quad (5.3)$$

where ϕ_0 is the potential calculated considering only the electrode potentials ($\rho(\vec{r}) = 0 \quad \forall \vec{r}$) and ϕ_ρ is the potential generated by the impurity charge distribution when grounding all the electrodes. We can thus solve the following two problems and then add up the solutions:

$$\begin{cases} \nabla^2 \phi_0(\vec{r}) &= 0 \\ \phi_0|_{S_{\text{cathode}}} &= V_{\text{cathode}} \\ \phi_0|_{S_{\text{anode}}} &= V_{\text{anode}} \end{cases} \quad \begin{cases} \nabla^2 \phi_\rho(\vec{r}) &= -\rho(\vec{r})/(\epsilon_0 \epsilon_r) \\ \phi_\rho|_{S_{\text{cathode}}} &= 0 \\ \phi_\rho|_{S_{\text{anode}}} &= 0 \end{cases} \quad (5.4)$$

Similarly, since the electric field is determined by the linear relation $\vec{E} = -\nabla\phi$, it can be also separated into two components:

$$\vec{E}(\vec{r}) = \vec{E}_0(\vec{r}) + \vec{E}_\rho(\vec{r}) \quad (5.5)$$

where $\vec{E}_0(\vec{r}) = -\nabla\phi_0(\vec{r})$ and $\vec{E}_\rho(\vec{r}) = -\nabla\phi_\rho(\vec{r})$.

Figure 5.2 shows the electric potential and the electric field strength of the two contributions and their sum for the BE3830/s detector operated in its nominal configuration, i.e. cathode grounded, anode set at 3500 V and $\rho \sim 10^{10}$ impurity atoms/cm³.

Figure 5.2.a and 5.2.b show the electric potential and field strength generated only by the electrodes ($\phi_0(\vec{r})$ and $||\vec{E}_0(\vec{r})||$). The potential and the field show a sharp variation in the region close to the small-size p+ electrode. The field in the rest of the volume is so weak that, without additional contributions, the charge collection time would be longer than the characteristic recombination time. Consequently, most of the charges would be lost.

Figure 5.2.c and 5.2.d show the electric potential and field strength provided only by the impurity charge distribution ($\phi_\rho(\vec{r})$ and $||\vec{E}_\rho(\vec{r})||$). For the considered BEGe detector the charge concentration can be approximated by a uniform distribution [104]. The resulting negative electric potential reaches its peak value in the middle of the detector. The direction of the electric field in the region close to the small cathode is opposite to that of \vec{E}_0 , whereas in the rest of the detector the field helps to move the charges produced close to the outer n+ electrode towards the central slice of the detector.

Figure 5.2.e and 5.2.f show the total electric potential and field strength ($\phi(\vec{r})$ and $||\vec{E}(\vec{r})||$). The potential close to the small p+ electrode is dominated by the electrodes contribution smoothed out by the opposite contribution of the impurity charge distribution field. In the rest of the volume the dominant contribution is provided by E_ρ . The effect of the E_ρ field is to bring the holes in the center of the detector while the field E_0 subsequently

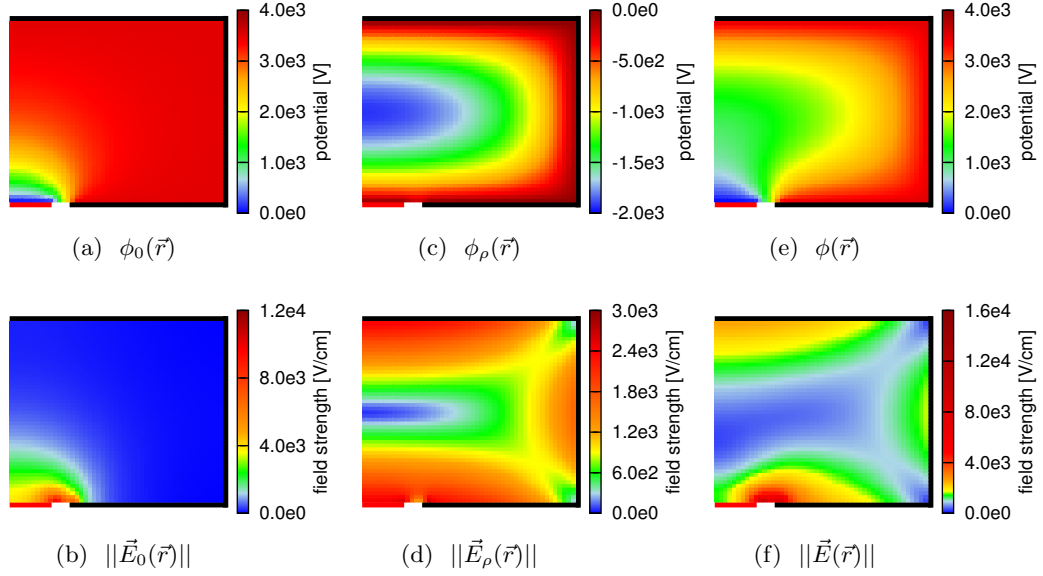


Figure 5.2: Simulated electric potential and electric field strength for different configurations of a BEGe detector. In (a) and (b) the electrode potential is considered, in (c) and (d) the charge distribution, and in (e) and (f) the sum of the two contributions. The plots show half of a vertical section of the detector passing through the symmetry axis. The cathode is drawn in red and the anode in black.

collects them to the read-out electrode. This peculiar way of charge transportation in BEGe detectors leads to a favorable signal shape, as it will be discussed in the next sections.

5.2.2 Signal development in dependence of the interaction position

According to equation (5.2), the charge signal induced on the read-out electrode by a cluster of charges drifting inside the detector is given by the cluster trajectory – determined by the electric field – and the weighting potential. Figure 5.3 shows the weighting potential $\phi_w(\vec{r})$ and the strength of the weighting field $\|\vec{E}_w(\vec{r})\| = \|\nabla\phi_w(\vec{r})\|$ of the cathode in a BEGe detector. The weighting potential (similarly to ϕ_0 in Figure 5.2.a) has a sharp variation in the region close to the small-size p+ electrode and it is very weak in the rest of the detector volume (blue area in Figure 5.3).

If an interaction occurs in the volume of weak ϕ_w , the signal, induced by the holes drifting towards the small cathode, remains small until the charges arrive at about 1 cm away from the electrode and then rapidly grows until the holes are collected. Conversely, the electron contribution is expected to be present only at the beginning of the pulse and to have a negligible amplitude for most of the interaction positions. Electrons are collected to the n+ electrode. The portion of the detector volume that is close to this electrode is

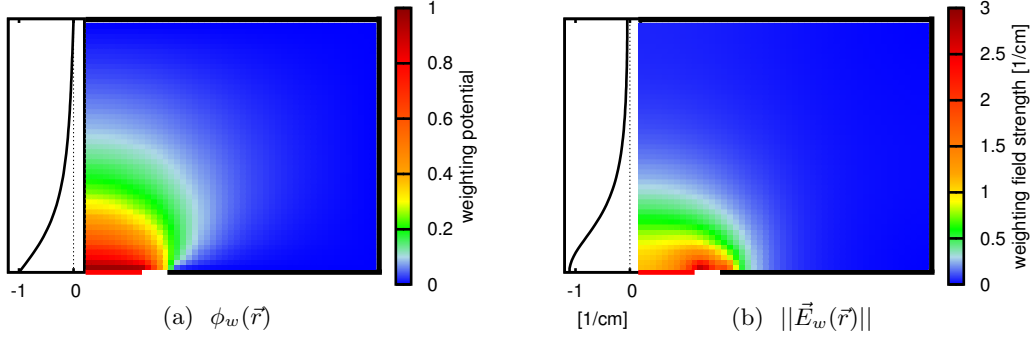


Figure 5.3: (a) Weighting potential and (b) weighting field strength of the small read-out electrode (cathode) computed for half of a vertical section of the BEGe detector passing through the detector symmetry axis (density maps) and for the symmetry axis (black lines in the side plots). The cathode is drawn in red and the anode in black.

much larger than the portion close to the p+ electrode. The electron collection is hence very quick, and further shortened as their velocities is roughly two times higher than for the holes. The signal induced on the read-out electrode is expected to be negligible compared to the one resulting from the last part of the hole collection, since the electron movement can occur entirely in the region of weak ϕ_w .

Figure 5.4.a shows the electron and hole trajectories for three interactions in the “bulk” detector volume far from the p+ electrode. The holes follow the electric field (Figure 5.2.f) and are first transported into the middle slice of the detector, then drift towards the center of the detector and finally their trajectory bends in the direction of the read-out electrode. In the following we will refer to this feature as “funnel effect”.

Because of the funnel effect, the last part of the hole collection happens along a common path which is independent of the starting position. Accordingly, the last part of the induced signal is identical for the different events. Since the first part of the signal, induced by the holes and electrons in weak ϕ_w regions, is comparatively small, the signal shapes are essentially independent of the interaction position. This can be clearly seen in Figure 5.4.b, which shows the charge and current pulses corresponding to the trajectories from Figure 5.4.a. The only visible difference is the time shift of the rising part, which depends on the length of the charge carrier path to reach the strong ϕ_w region. It is important to stress that this type of almost indistinguishable signals originates from interactions in most of the detector volume, including corner regions. For further discussion we will refer to such signals as “type I” trajectories.

The shape of the current signals in Figure 5.4.b can be understood by differentiating the function in equation (5.2). The current induced at the cathode by a charge carrier cluster is

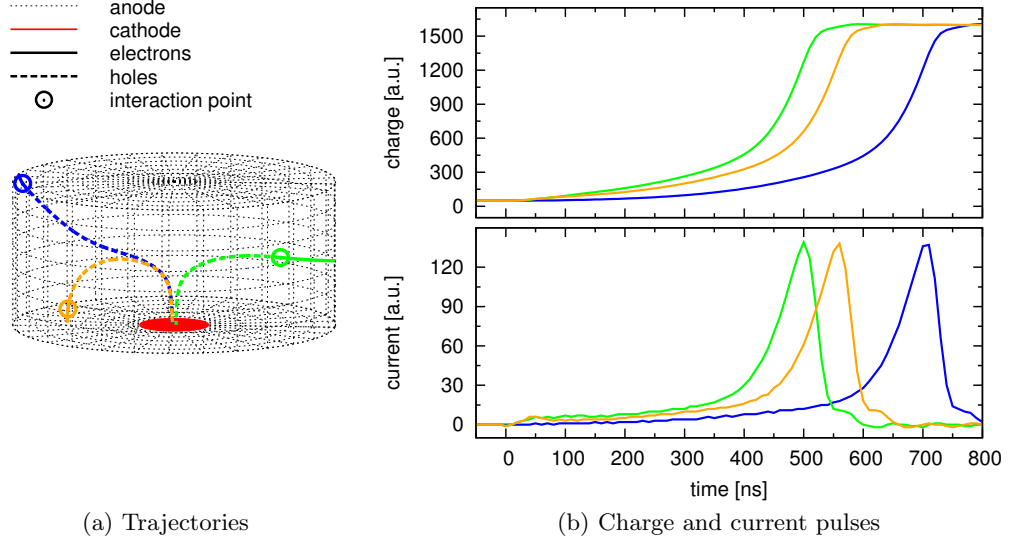


Figure 5.4: (a) Simulated electron-hole trajectories and (b) corresponding charge and current pulses for three events occurring in different places in the bulk detector volume far from the p+ electrode (“type I” trajectories). The small oscillation in the current signals after the peak originates from the experimentally measured FE and DAQ response the pulses are convolved with.

then given by:

$$I(\vec{r}(t)) = \frac{dQ(\vec{r}(t))}{dt} = q_{\text{tot}} \vec{v}(\vec{r}(t)) \cdot \vec{E}_w(\vec{r}(t)) \quad (5.6)$$

From this equation we can see that the induced current $I(\vec{r}(t))$ depends on the velocity $\vec{v}(\vec{r}(t))$ and the weighting field $\vec{E}_w(\vec{r}(t))$ at the position $\vec{r}(t)$ of the charge cluster. The charge carrier velocity can vary roughly between $0.5 \cdot 10^7$ cm/s and $1.2 \cdot 10^7$ cm/s [90, 102], while E_w can increase by more than a factor of 20 close to the read-out electrode (see Figure 5.3.b). Since E_w has a dominant effect, the signals induced by “type I” trajectories in Figure 5.4.b feature only one current peak at the end of the hole collection.

Two other types of less common trajectories, due to interactions in proximity of the groove and the small p+ electrode, have been identified. Examples of this kind of events are displayed in Figure 5.5. The “type II” trajectories originate close to the p+ electrode (green and black color). In these cases, the holes are directly and quickly collected at the cathode. Also the electrons drifting in the opposite direction provide a significant contribution to the signal, since they are now moving in a region of strong ϕ_w . The closer the interaction occurs to the cathode, the more important the signal induced by electrons becomes. The signal is fully dominated by the electron contribution for interactions within ~ 2 mm from the p+ electrode (black example in Figure 5.5). The induced charge signal rises quickly at

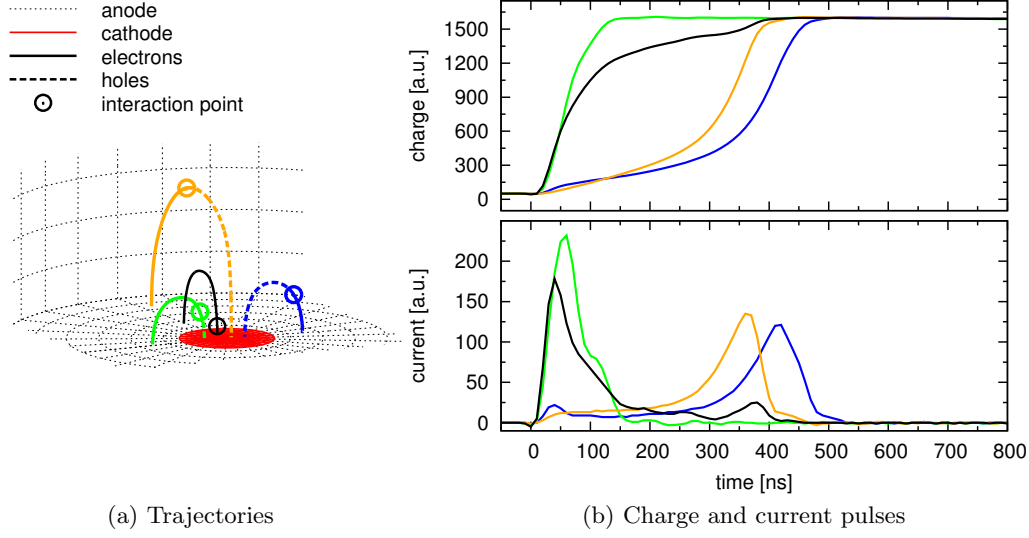


Figure 5.5: (a) Simulated electron-hole trajectories and (b) corresponding charge and current pulses for three events occurring next to the cathode and a “type I” event (orange line). For the green and black events (“type II” trajectories) both the electron and hole contribution are present at the very beginning of the signal. In the blue event (“type III”) the electron collection is quick and provides a characteristic kink in the first part of the signal.

the beginning and then, as the electrons drift away from the cathode into the weaker ϕ_w regions, the signal growth slows down. The current peak appears at the very beginning of the collection time. For events occurring few mm to ~ 1 cm from the p+ electrode (green example in Figure 5.5) neither electrons nor holes traverse the full thickness of the strong ϕ_w region. The main part of the signal is induced in a relatively short time and the rise time is thus faster. The current peak is amplified because contributions from both charge carrier types add up. The current amplification can be further enhanced if the interaction happens close to the inner edge of the groove, because here E_w is strongest (Figure 5.3.b).

Interactions in the zone close to the anode, ~ 1.5 cm from the detector symmetry axis, result in “type III” trajectories (shown in blue in Figure 5.5). The electrons are collected quickly in these events and, since ϕ_w is still noticeable in this region, they create a characteristic kink in the first part of the signal. This quick increase at the beginning causes the 10% to 90% rise time measurement to give higher values for these events than for the “standard” type I trajectory events.

The three types of signals and the extent of the volumes from which they originate can be better understood from the plots shown in Figure 5.6. The figure shows the rise times in the 10% to 30% and 10% to 90% intervals of the signal maximum amplitude, as a function of the interaction position. The type II trajectories originate in the volume close to the p+

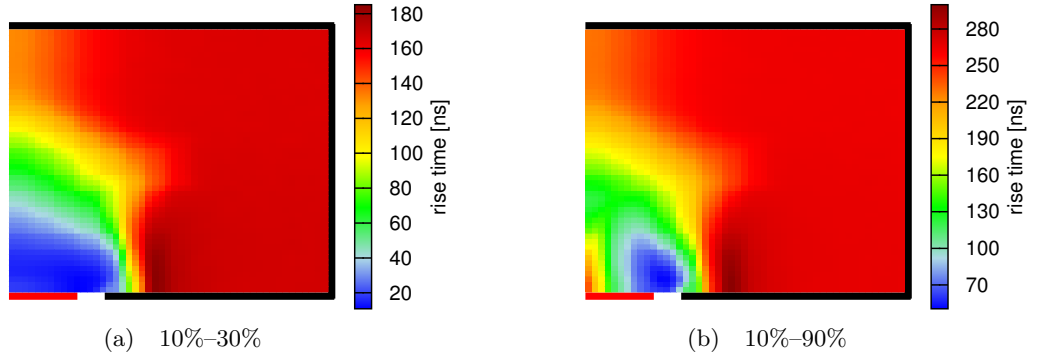


Figure 5.6: Signal rise times 10–30% (a) and 10–90% (b) as a function of the interaction position for a BEGe detector.

electrode ($\sim 6\%$ of the active volume), distinguished by short rise times plus a small zone of longer rise times few mm away from the center of the electrode. The type III trajectory starting points can be identified in the area of increased rise time beyond the outer diameter of the groove ($\sim 1\%$ of the total active volume). Interactions in the rest of the detector volume result in the most common type I trajectories.

5.2.3 Discrimination between single-site and multiple-site events

As explained in the previous subsection, single energy depositions in BEGe detectors have high probability of producing signals with a well defined shape (type I trajectories), differing only in the total charge collection time. The relative current signals have a simple shape with only a single narrow peak at the end of the charge collection. These features can be exploited for a powerful discrimination of single-site events ($0\nu\beta\beta$ like) and multiple-site events (typical of gamma-induced background). A discrimination method based on the current signal amplitude was introduced in Ref. [89] and explained by using an empirical estimate of the weighting fields in BEGe detectors [88]. Here we recall the basic idea of the method and refine the discussion using the additional information available with a comprehensive signal modeling.

Because of the funnel effect created by the peculiar electrode geometry, the part of the hole trajectory that passes through strong E_w is the same for most of the interaction locations inside the Ge crystal. As a consequence, the amplitude of the induced current signal depends only on the total charge of the considered hole cluster (see equation (5.6)). Figure 5.7 shows the value of the maximum current pulse amplitude A as a function of the interaction position, for simulated single interactions with normalized energy deposition in a vertical section of a BEGe detector. The parameter A is constant in most of the detector

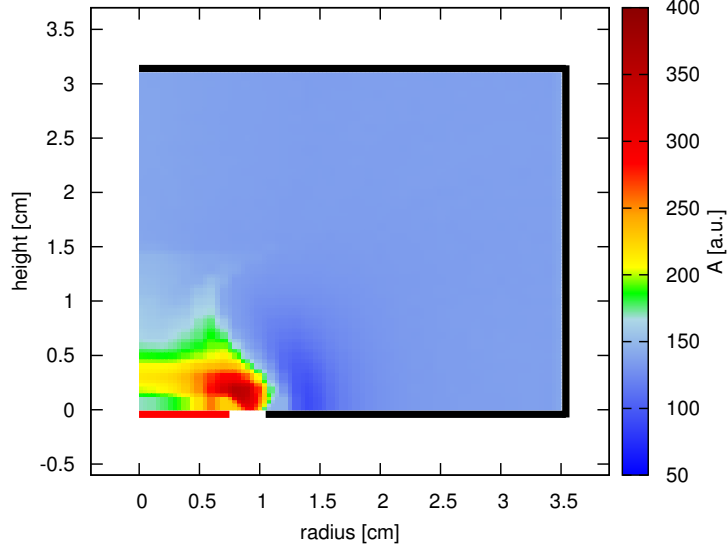


Figure 5.7: Distribution of the maximum current pulse amplitude A for simulated single interactions with unit energy as a function of the interaction point. A is constant in most of the detector volume (type I trajectories), but it is amplified in the region close to the cathode (type II trajectories). The region of lower A values close to the outer radius of the groove is an artifact due to the use of the pulse shape library with 1 mm step size. Here the charge collection time varies on scales smaller than the library grid with the effect that the averaging of library pulses leads to a reduction in current-peak amplitude. The effect is not present when the signals are generated directly without the use of the library.

volume (corresponding to the typical type I trajectories) except for the region close to the p+ electrode, where the type II trajectories with amplified current signals originate (Figure 5.5).

The Pulse Shape Discrimination (PSD) method uses the parameter A normalized to the total event energy E : the A/E ratio. The concept is depicted in Figure 5.8. In single-site events (SSE), all the energy is transferred to a single charge cluster and the A/E parameter assumes a constant value. In multiple-site events (MSE), the total event energy is shared between several spatially-separated charge clusters (Figure 5.8 illustrates the case of three clusters). Since the current peaks are narrow and the charge collection time is position-dependent, the A/E ratio is smaller than the constant value assumed in SSE.

The region of amplified current signals (approximately a hemisphere of a ~ 13 mm radius from the center of the p+ electrode in Figure 5.7, corresponding to $\sim 5\%$ of the detector active volume) was already identified in Refs. [89, 88]. It limits the efficiency of the PSD method, since interactions from MSE occurring in this volume can have their A/E ratio amplified above the SSE discrimination threshold. However, this effect can be used to identify surface events occurring on the p+ electrode and groove surfaces. This topic is discussed in Section 6.2.

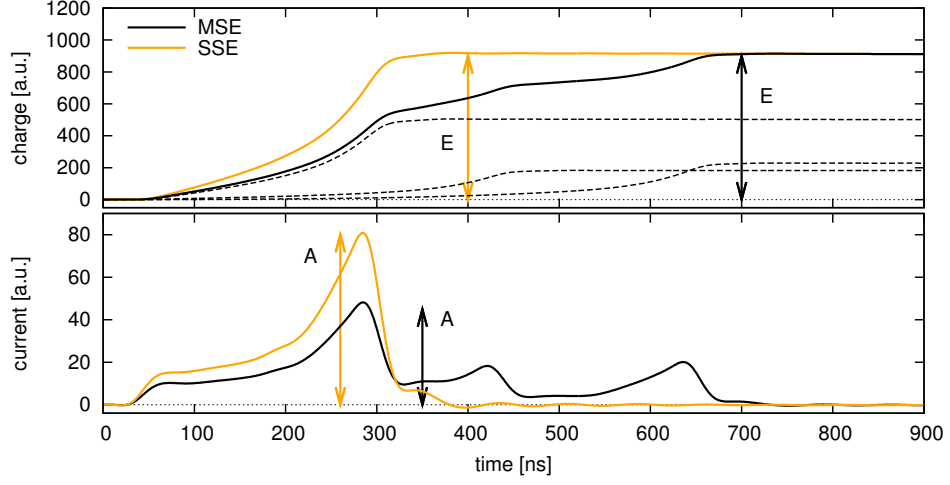


Figure 5.8: The upper panel shows typical charge pulses for SSE and MSE while the lower panel shows the corresponding current pulses obtained as the derivatives of the charge signals. The dashed lines in the top panel show the contributions of the individual single interactions to the total charge pulse in the MSE.

5.3 Validation of the simulation

The results of Monte Carlo simulations with BEGe geometries using the MAGE framework – accurately reproducing their radiation detection efficiency – were presented in Refs. [88, 89, 90, 92]. In this section we report only the measurements carried out to validate the pulse shape simulation (Block II and III). Two sets of measurements were performed for this purpose. First we used a collimated ^{241}Am source to generate well-localized interactions and to compare the pulse shapes for various interaction positions close to the surface of the detector. Then, a ^{228}Th source was used to investigate the distribution of the pulse rise times and of the parameter A/E as a function of energy, for events in the whole detector volume. Preliminary results of the comparison with ^{241}Am measurements – obtained with different data sets and using only the Block II of the simulation – have been published by the author in Refs. [90, 91].

5.3.1 Experimental setup and data processing

The detector used for the validation measurements was the BE3830/s BEGe detector described in Section 5.2. The front-end read-out of the signals was performed with the Canberra charge sensitive preamplifier 2002CSL [49], integrated in the housing of the detector. The preamplifier output was digitally recorded with a 4 channel N1728B CAEN NIM flash analogue-digital converter [105] running at 100 MHz sampling frequency with a

precision of 14 bits. This module is fitted with a USB connection for communication with a PC. To control the digitizer setup, the acquisition parameters and the storage of the data, the PC was interfaced to the NIM module by using the TUC software [106]. We recorded pulse shapes with a total length of $40\text{ }\mu\text{s}$ including a baseline before the signal of $\sim 10\text{ }\mu\text{s}$.

The off-line analysis of the signals has been performed using the GELATIO software. The chains of modules and the data selection were similar to the ones discussed in Section 2.2.1 and Section 2.2.2. In particular, the energy has been reconstructed using the *Moving Window Deconvolution* approach [107] (*EnergyGastModule*, see Appendix B) and several digital filters were applied to the data to reject pile-up and noise events. Before extracting the maximum current pulse amplitude A , the signals – sampled at 100 MHz – are integrated with a three-folded 50 ns moving average (*MWAverageModule*), differentiated and finally interpolated down to 1 ns sampling period (*CurrentPSAModule*). This filtering was found to provide the optimal resolution for the parameter A .

To perform the ^{241}Am measurements, a mechanical device was built to allow the movement of collimated sources with sufficient accuracy along the diameter of the front face and circularly around the symmetry axis of the detector. The collimator had a hole of 1 mm diameter and a length of 34 mm. These ^{241}Am collimated measurements were accurately simulated by using a conical beam of 59.5 keV photons.

5.3.2 Pulse shape comparison with low energy gamma-ray beams

Using a collimated beam of low energy gamma-rays (59.5 keV) from an ^{241}Am source allows to obtain pulse shape data with well defined interaction coordinates. The 59.5 keV photons penetrate only a few millimeters underneath the Ge crystal surface and the volume spread of their energy deposition is of similar size. As the topologies of the individual photon interactions are statistically variable, we selected events with energy deposition corresponding to the 59.5 keV peak and calculated the average signals for each position of the collimated source³. This averaging procedure also reduced significantly the electronic noise.

The pulse shape comparison included a scan along the diameter of the detector and a circular scan at a fixed distance from the symmetry axis of the Ge crystal. The radial scan was used to study the pulse shapes as a function of the distance from the center. The circular scan allowed to investigate the rise time variations due to the drift velocity anisotropy caused by the crystal lattice structure.

The radial scan was performed by moving the collimated ^{241}Am source along the radius of the detector on the top surface of the end-cap in steps of 0.5 cm. The simulated hole

³The calculation has been performed by using the *AveragePulseModule* implemented in GELATIO. The algorithm, described in detail in Appendix B, is designed to ensure the convergence of the average to the most frequent pulse shape of the sample.

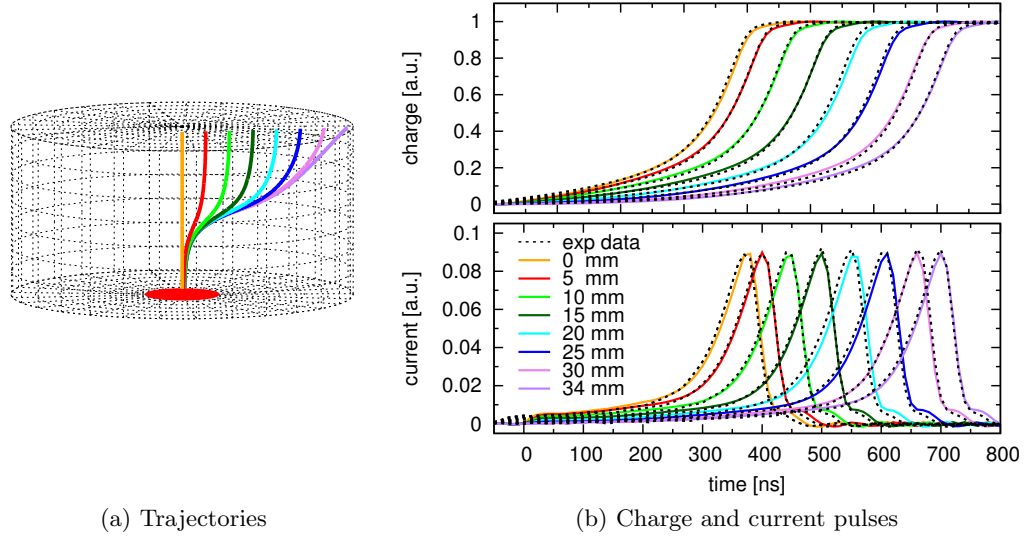


Figure 5.9: (a) Simulated hole trajectories and (b) average signals computed for several interaction points at different radii on the detector top surface. The interactions were obtained by moving a 1 mm collimated ^{241}Am source on the top surface of the end-cap along the radial direction. As the absolute start time of the experimental signals was not measured, the experimental pulses are aligned to the simulated ones by fitting. The small deviation present at the very beginning of the signals can be related to the fixed grid width used for defining the library of pulses.

trajectories for each collimator position and the average signals are shown in Figure 5.9. The simulated and experimental pulses are in good visual agreement.

A quantitative comparison has been done using the pulse rise time. As an increase of the radius value corresponds to an increment of the hole collection time, the total rise time should increase as the interaction point moves away from the symmetry axis. However, according to the discussion in Section 5.2.2, the pulse shapes for interactions far from the p+ electrode are expected to be different only at the very beginning. In Figure 5.6.b, the BEGe signals along the top surface show only a minimal variation of the 10%–90% rise time. In order to observe a significant effect, the rise time between 1% and 90% has to be considered. This can be clearly seen in Figure 5.10.a for both the experimental and simulated data.

The circular scan has been performed by moving the collimated ^{241}Am source along a circle with a radius of 34 mm centered on the detector symmetry axis, on the top surface of the end-cap with $\sim 10^\circ$ steps. The drift velocity anisotropy is due to the charge carriers moving at different angles relative to the detector crystallographic axes. Similarly to the radial scanning, also in this case the differences occur only in the first part of the charge collection, and the 1%–90% rise time has to be used. The comparison of circular-scan rise times as a function of the circumference angle from the simulation and the experiment is shown in Figure 5.10.b.

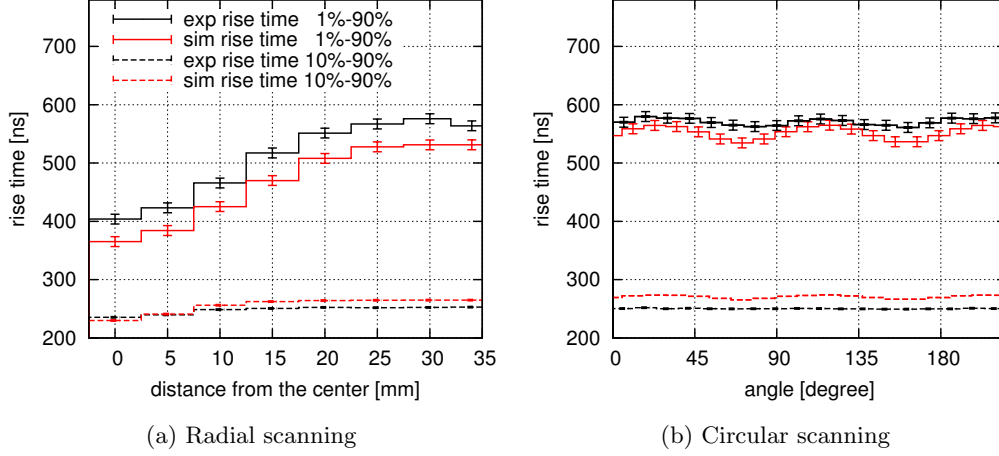


Figure 5.10: 1%–90% and 10%–90% rise time values reconstructed from the simulated and experimental average pulses for different interaction points. The interactions were obtained by moving a 1 mm collimated ^{241}Am source on the top surface of the end-cap, along the radial direction (a) and around a part of a circle centered on the detector symmetry axis (b). The rise time uncertainty was estimated by determining the spread of rise time values computed from several measurements at one source position.

Although the experimental data show a behavior coherent with the simulation in both the radial and circular scans, the agreement is only qualitative. The 1%–90% rise times of the simulated data are systematically shifted by 20–40 ns (5%–10% of the total rise time) to lower values than the experimental data. In contrast, the 10%–90% rise times of the simulated data are shifted by ~ 20 ns to higher values than the experimental data. The change in the sign of the discrepancy is due to differences in the shape of the average pulses. Furthermore, the oscillation amplitude due to crystal anisotropy in Figure 5.10.b is higher in the simulation than in the experimental data by 30%. Unlike the experimental data, the simulation shows a residual oscillation of about 5 ns also in the 10%–90% rise time plot. From these comparisons we can conclude that the simulation overestimates the drift velocity anisotropy and probably further small discrepancies in the signal calculation are present.

According to these results, we identified several areas of possible improvements of the simulation, including the accuracy in the geometry definition (especially important in case of the p+ electrode), the finite grid width used for defining the library of pulses and the charge carrier mobility model parameterizations (the parameters could in principle change among different detectors according to the properties of the germanium material and the crystal pulling technique used). Also further measurements could be performed to characterize the position dependence of the BEGe detector signals, e.g. scanning the side and back surfaces of the detector with a collimated ^{241}Am source or sampling its internal volume by means of single-Compton scattering measurements with high-energy sources.

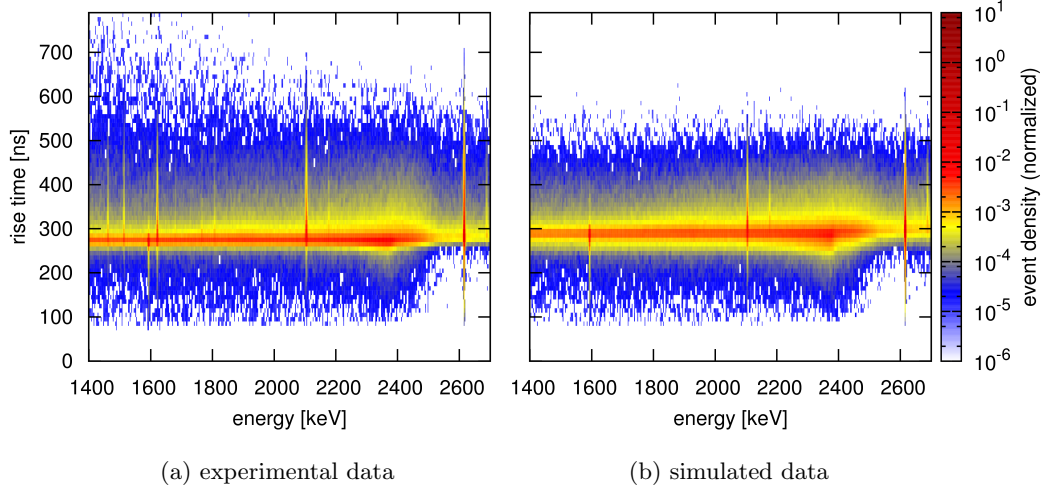


Figure 5.11: Experimental and simulated distributions of the 10%–90% rise time values as a function of energy from the ^{228}Th measurements. In the simulation only ^{208}Tl is considered. The density plots are normalized according to the number of events in the 2.6 MeV FEP.

5.3.3 Rise time and A/E distribution studies

To validate the pulse shape simulation for interactions in the detector bulk volume, we compared the rise time and the A/E distributions as a function of the event energy for ^{228}Th isotropic interactions. Unlike the ^{241}Am measurements, which create interactions restricted to a region close to the detector surface, 2.6 MeV gamma-rays from a ^{228}Th source interact in the whole detector volume and can deposit energy at several sites before escaping or being absorbed. Under these circumstances, the distributions of the rise times and of the parameter A/E are sensitive to the electric and weighting potential in the whole detector and thus are useful for testing the accuracy of the simulation. For this study a long measurement was performed with a ^{228}Th source⁴. The detector was located in the LNGS underground laboratory and surrounded by a lead shielding in order to reduce the background due to cosmic rays and natural radioactivity.

Figure 5.11 shows the distribution of the 10%–90% rise time as a function of the energy in the range including the full energy absorption peak (FEP) at 2614.5 keV of ^{208}Tl , and the relative double escape peak (DEP) at 1592.5 keV. Both the experimental and simulated data show a similar structure of the distribution, with a high density band at rise time values around ~ 270 ns. The region below the band contains the fast pulses resulting from events with type II charge collection trajectories described in Section 5.2.2, generated by interactions

⁴In the simulation only the ^{208}Tl isotope was considered resulting in some missing gamma-ray interactions at energies below ~ 1.8 MeV as compared to the experimentally measured spectrum. Also, the simulation does not include the SEP Doppler broadening of the positron annihilation energy which is determined by the electron momentum distribution in Ge [63].

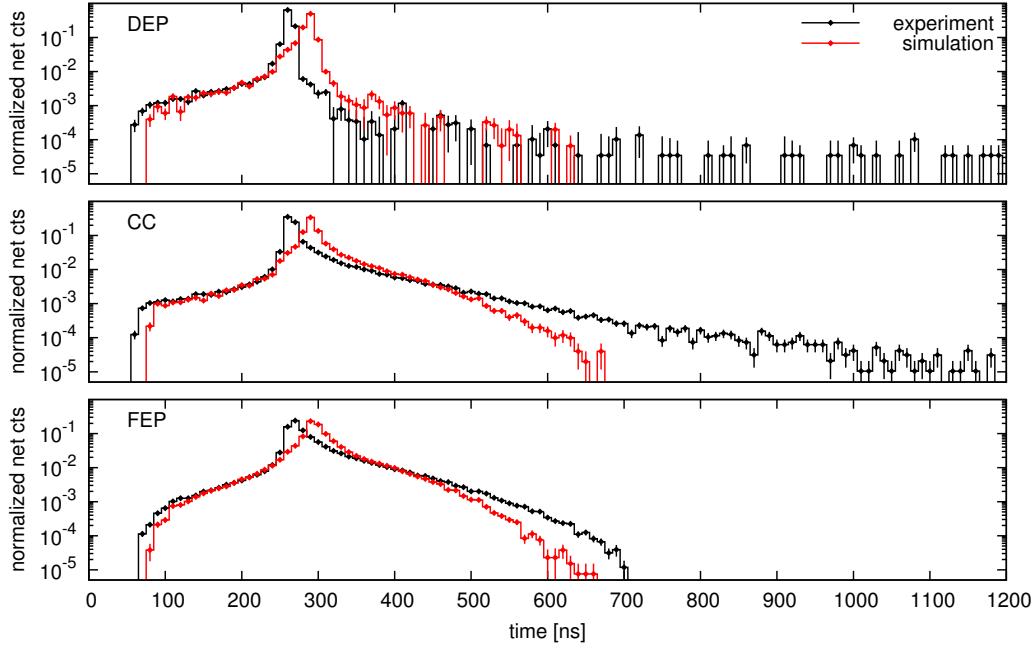


Figure 5.12: Experimental and simulated distributions of the rise time for the region around the DEP, the Compton continuum at 2 MeV (CC) and the 2.6 MeV FEP. The error bars account for Gaussian statistical uncertainties. The DEP and the FEP distribution are corrected for the background. The integrals of the histograms are normalized to one.

close to the p+ electrode. The region above the band is composed mainly of MSE which have typically slower rise times than SSE (this is visible in Figure 5.8). Consistently, all the full absorption peaks (consisting mainly of multiple Compton scatterings followed by photo-absorption) show an important tail in this region, while the DEP (containing the single-site e^- and e^+ absorptions after pair-production) has a very weak tail. According to the simulation, events occurring in a small volume close to the outer radius of the groove (type III charge collection trajectories in Section 5.2.2) are also expected to have increased rise times. It is however evident from the plot that the simulation creates events with rise times only up to 600 ns while the experimental data show a significant number of events with rise time > 600 ns ($\sim 1.5\%$ of the total).

The simulated and experimental data can be compared in more detail in Figure 5.12, which shows distributions of the 10%–90% rise time in narrow energy regions around the DEP, the Compton continuum at 2 MeV and the 2.6 MeV FEP. For the DEP and FEP distributions, the contribution from their Compton continuum backgrounds is subtracted. While the shape of the distribution below ~ 250 ns (corresponding to the fast signals from the type II events) is reproduced fairly well, the main peak and the region above it show some differences between the simulation and experimental histograms. As we already noted

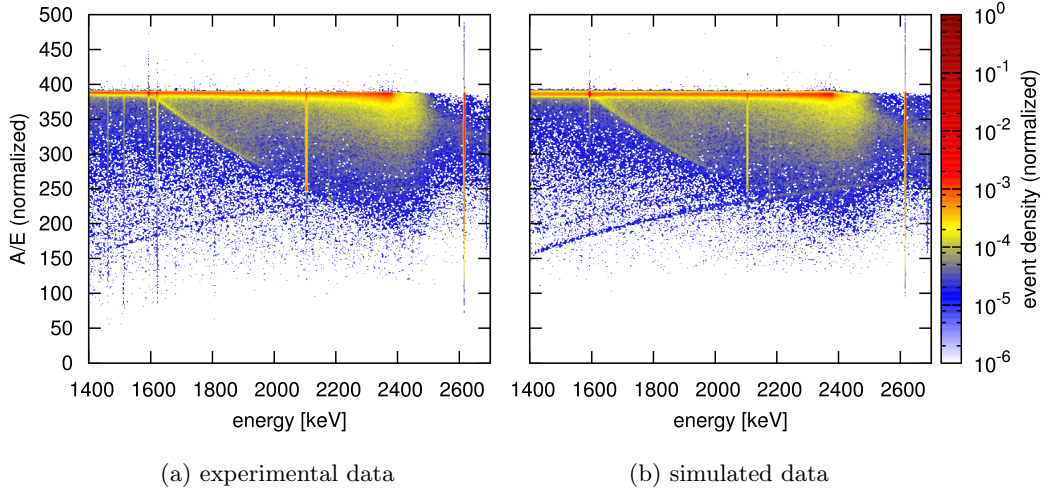


Figure 5.13: Experimental and simulated distributions of the A/E parameter as a function of energy for ^{228}Th source measurement. In the simulation only the ^{208}Tl is considered. The density plots are normalized according to the number of events in the 2.6 MeV FEP.

in the previous subsection, the simulation is not perfect in some aspects. The charge carrier mobility model is likely responsible for the shift of the rise time histogram maximum, while the enhanced drift velocity anisotropy in the simulation could explain the broadening of the peak. Minor discrepancies in the geometry description of the p+ electrode and the groove, as well as the finite grid width of the pulse library, could account for the small ~ 20 ns shift between the start of the experimental and simulated histogram, as well as for a part of the excess long rise time events in the experiment. In addition, some unidentified pile-up events could show up with very long rise times, up to a few μs .

Most of the signals with rise time above ~ 500 ns (most clearly visible in the Compton continuum histogram in Figure 5.12) are however expected to come from the region close to the n+ surface. The Li-diffused n-side of the p-n junction can not be fully depleted of conduction band electrons and forms the well-known dead layer covering the outer surfaces of p-type Ge detectors. The appearance of pulses with long rise times in n+ surface interactions was noticed before with conversion electron measurements in Ref. [108] and can be clearly observed by irradiating the detector with ^{241}Am gamma rays, as reported in Ref. [109, 110]. In the following, we will refer to these signals with long rise time as “slow pulses”. The topic will be discussed in detail in Section 6.3.

Figure 5.13 shows the distribution of the parameter A/E as a function of energy. The plots show a well defined horizontal band of increased event density, composed of SSE. Below the band the region of MSE extends. Above the band, a region of events with amplified current signal is visible. These signals are expected by interactions occurring close to the p+ electrode as already discussed in Section 5.2.3. This interpretation of the A/E distribution

was previously validated by coincident Compton scattering measurements (providing clean SSE samples at several energies) and by collimated ^{228}Th measurements (providing DEP events restricted to the detector volume close and far from the p+ electrode) [89, 88]. Another visible feature in the plot is a diagonal band between the DEP and the Single Escape Peak (SEP), composed of pair-production events (as explained in Ref. [89, 88]), and two weak narrow bands in the MSE region, which are caused by cascade summing events⁵. There is no significant difference between the plots from the experimental and simulated data apart from the ^{212}Bi lines present in the measurement and not in the simulation. All the features of the A/E distribution are reproduced by the simulation.

Figure 5.14 shows the A/E distribution for energy slices around the DEP, the Compton continuum at 2 MeV and the SEP at 2103.5 keV. As in Figure 5.12, the distributions from the DEP and SEP are corrected for the Compton continuum background contribution. The simulation is in good agreement with the experimental data in all three energy regions. However, a small deviation at low A/E values is visible in the Compton continuum region. This excess can be associated with the presence of the near n+ electrode slow pulses in experimental data. We can assume that, because of the stretching of charge carrier cluster, the peak in the current signal gets wider and its amplitude is reduced. By applying a cut on the rise time at 600 ns (black histogram in Figure 5.14) the agreement in the tails improves significantly.

The bottom panels of Figure 5.14 show the A/E distributions of the Compton continuum, SEP and DEP in the region near the SSE-band peak ($A/E \sim 385$). The simulated SSE peak is a little wider than in the experimental data and the shape is slightly different. This discrepancy is clearly visible in the DEP plot and it is probably due to the same simulation inaccuracies discussed earlier. The Compton continuum and SEP distributions show that for MSE-dominated distributions the overall agreement is significantly better. This demonstrates that the partitioning of the energy depositions into individual charge clusters (Block I) is simulated accurately.

5.4 Conclusions

In this chapter the first comprehensive modeling of the signal formation and development in BEGe detectors is presented. The simulation developed in this work was used to study in detail the response of the detector to charged particle and gamma-ray interactions. In particular, the pulse shape dependence from the interaction location was investigated, improving the understanding of this detector design.

⁵The two visible additional bands result from the summation of the SSE in the Compton continuum with either the 511 keV or 583 keV full energy gamma absorption from the ^{208}Tl cascade. This results in the energy of the event being shifted but the A value staying the same since the SSE from the Compton scattering still dominates the current signal.

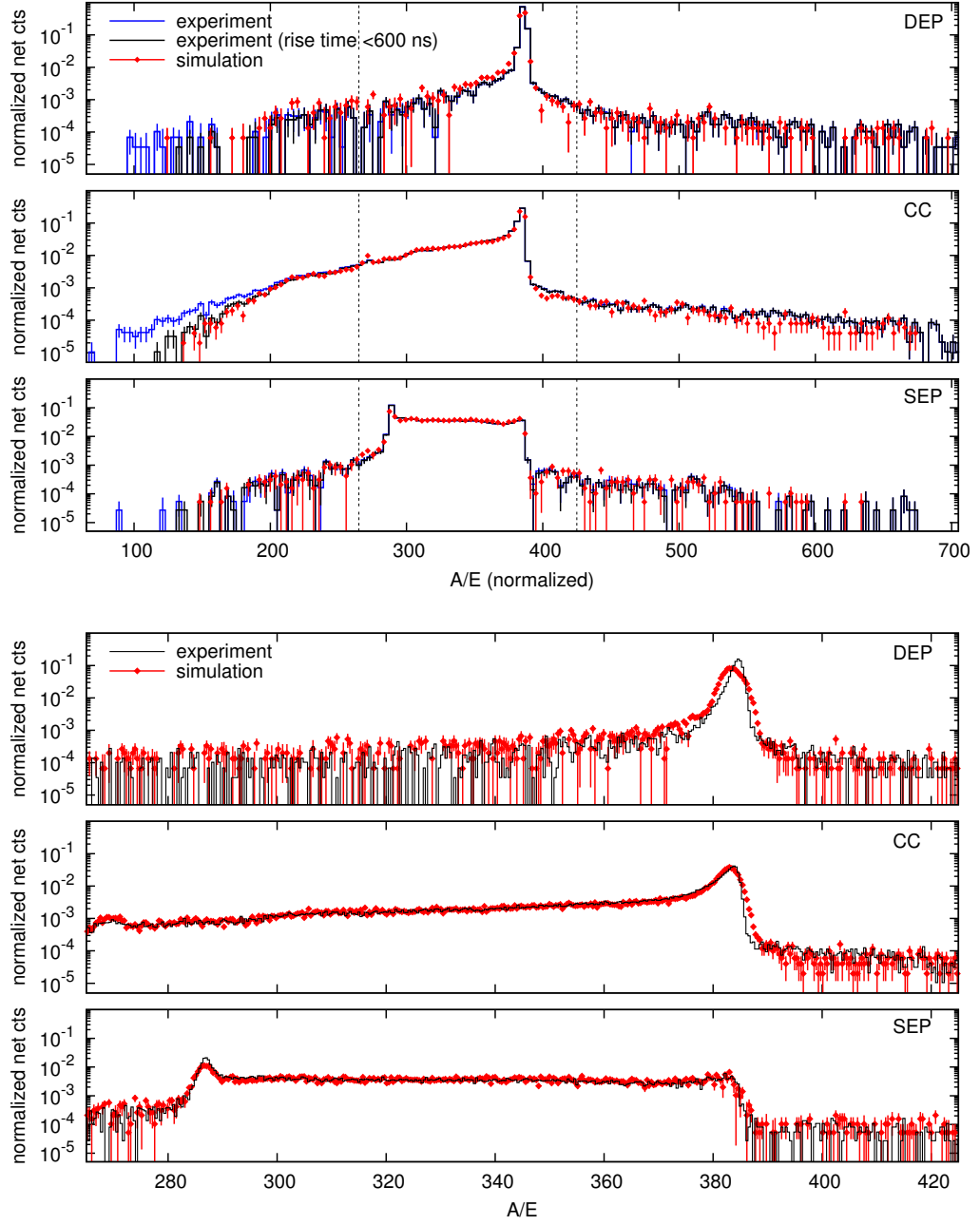


Figure 5.14: Experimental and simulated distribution of the A/E parameter in the region around the DEP, the Compton continuum at 2 MeV (CC) and the SEP. The error bars account for Gaussian statistical uncertainties. The DEP and the SEP distributions are corrected for the background. The integrals are normalized to one. The top panels show the experimental histograms before and after a cut on the rise time to remove slow pulses not included in the simulation. The regions defined by the gray vertical lines are enlarged in the bottom panels.

The electric field created by the electrode geometry of BEGe detector has been traced back to a peculiar charge collection mechanism. The holes generated by interactions in most of the detector active volume are collected first in the center of the detector, and then drift toward the small read-out electrode along a common trajectory. The comprehension of this effect – named funnel effect – is of great importance for $0\nu\beta\beta$ experiments, since it allows for an efficient discrimination of the signals induced by single-site and multiple-site events (A/E method).

The simulation results were compared to the experimental data and found to be in quantitative agreement, although some discrepancies have been identified. The simulation proved to reproduce quite accurately the distributions of the A/E parameter. It can hence be used to estimate the pulse shape distribution performances in scenarios that are not easily accessible experimentally.

Chapter 6

Background rejection and signal identification studies

This chapter summarizes the studies performed in the framework of this thesis work about pulse shape discrimination (PSD) techniques for BEGe detectors. In Section 6.1, we assess the discrimination efficiency of the A/E method for the $0\nu\beta\beta$ signal of ^{76}Ge and the background due to two cosmogenic isotopes produced in germanium, which are potentially critical for GERDA Phase II, i.e. ^{68}Ge and ^{60}Co . These decays occur inside the detector and their experimental study is difficult (even impossible in case of $0\nu\beta\beta$). This analysis is thus performed using the simulation tool described and validated in the previous chapter, which was shown to reproduce quantitatively the distribution of the A/E parameter. The results of this work have been published also in Ref [71].

The second part of the chapter describes the experimental characterization of the BEGe detector response to interactions on the surface of the Ge crystal and the development of PSD techniques for their identification. This issue is extremely important considering that various background sources expected in GERDA Phase II are alpha- or beta-emitting isotopes (e.g. ^{210}Po , ^{42}K and the isotopes in the ^{222}Rn decay chain), which produce mostly energy depositions on the surface of the detectors. Section 6.2 deals with interactions on the surface of the B-implanted read-out electrode and the groove. Section 6.3 focuses on energy depositions in the thick Li-diffused n+ surface layer which covers most of the Ge crystal.

6.1 Decays internal to the germanium crystal

In this section, the pulse shape simulation presented in Chapter 5 is used to assess the performance of the A/E parameter on different types of events (the parameter concept is discussed in Section 5.2.3). First the A/E method is applied to an experimental data set obtained with ^{228}Th and ^{60}Co sources placed outside the detector cryostat. The PSD

analysis is applied also to a set of simulated data reproducing the experimental measurements. The comparison of the PSD performances computed from the two sets of data is used to investigate systematic uncertainties and biases present in the simulation. The pulse shape simulation is hence used to evaluate the survival probability of decays occurring inside the Ge crystal and difficult to assess experimentally. The processes considered are neutrinoless double beta decays of ^{76}Ge and decays of ^{68}Ge and ^{60}Co .

This information is of great interest for GERDA Phase II. The evaluation of the $0\nu\beta\beta$ signal acceptance is an input of the analysis of the $0\nu\beta\beta$ half-life. ^{68}Ge and ^{60}Co are produced by cosmic ray interactions during the detector production above ground and can be critical backgrounds for GERDA Phase II. The average background index expected in the first three years of data taking is $\lesssim 2 \cdot 10^{-3}$ cts/(keV·kg·yr) for ^{68}Ge and $\lesssim 2 \cdot 10^{-4}$ cts/(keV·kg·yr) for ^{60}Co [111].

Obtaining experimentally these results is however challenging. $0\nu\beta\beta$ events can be studied only using a proxy. Typically, they are substituted by double-escape events from the 2.6 MeV gamma-line of ^{208}Tl . These events are created when the gamma-ray interacts via pair-production. The electron and positron energy is deposited within a few millimeters from the primary interaction site and the 511 keV annihilation gammas escape the detector without energy losses. These events resemble the $0\nu\beta\beta$ signal – which has two electrons in the final state – but have some substantial differences. In particular, the total event energy is lower (1592 keV) and the event distribution inside the Ge crystal is not homogeneous (double escape events have higher probability to occur close to the surface). Concerning ^{68}Ge and ^{60}Co , their typical activity in HPGe detectors is too low for precise measurements. The activation of these isotopes in larger quantities is possible but not trivial. For instance, it could be achieved by irradiating a detector with fast neutrons [112] or by an extended exposition to cosmic rays at high altitudes.

6.1.1 A/E cut performance on simulated and experimental data

The A/E pulse shape discrimination performances for simulated and experimental data have been compared using two high-statistic data sets produced by ^{228}Th and ^{60}Co sources located over the detector on its symmetry axis. The ^{228}Th source (^{208}Tl in the simulation) was placed at a distance of 2 cm from the Al end-cap (the same data set of Section 5.3). The ^{60}Co source was instead located directly at the end-cap. The detector, the data acquisition system and the signal processing used are the same described in Section 5.3.1.

As discussed in the previous chapter, the distribution of the A/E parameter for single-site events (SSE) is narrow and peaked around a precise value. Multiple-site events (MSE) are reconstructed at lower A/E values than SSE. The A/E method rejects MSE by applying a cut at a fixed distance below the central value of the SSE distribution. Since the central

value has a slight linear dependence on the event energy (order of 1% per MeV), the cut is defined as a linear function with two parameters: an offset and a “slope”.

The calibration of the two cut parameters is performed using the Compton continuum of the 2.6 MeV gamma-line of ^{208}Tl . As shown in Figure 5.13, the single-site events form a high-density band (in this case peaked at $A/E \sim 385$). The slope of the cut is calibrated by fitting the central values of the band at different energies following the procedure proposed and validated in Ref. [88]. The cut offset is calibrated by fixing the survival probability of the net area of the DEP to 90%, which corresponds to a $\sim 98\%$ acceptance of SSE (see Ref. [88] for the interpretation of these values). It should be mentioned that in Ref. [88] the offset was defined according to the shape and spread of the A/E distribution in the DEP region¹, features which are not reproduced perfectly by our simulation (see Figure 5.14, bottom DEP panel). The new definition, being based on the integral of the A/E distribution, is expected to be less affected by variations of the SSE peak profile.

The results of the PSD cut for experimental and simulated data are shown in Figure 6.11 and are listed in Table 6.1 (columns labeled “DEP fixed to 90%”). The experimental results are consistent with those obtained in previous works. Small differences with the values quoted in Refs. [89, 92] can be traced back to the data treatment, the implementation of the analysis or the position of the source (affecting the SSE/MSE composition of the Compton continuum regions).

The survival probabilities computed for the simulated data are systematically higher than the experimental results, indicating that the offset of the cut is shifted. Although the offset is defined using the integral of the A/E distribution, its calibration is still sensitive to the small differences between the experimental and simulated distributions in the left tail of SSE peak. In particular, the shift has been traced back to the different precision with which the simulation reproduces the A/E distribution of SSE and MSE. The modeling inaccuracies that affect the shape and width of the SSE peak have a smaller effect on the distribution of multiple-site events, for which the A/E value is defined by the number of interaction sites rather than the shape of the pulse induced by each charge cluster. The shift of the offset position in the simulated data is hence correlated to the SSE/MSE ratio of the sample used for its calibration.

To improve the accuracy of the cut results on simulated data, the calibration of the cut offset should be performed on a sample having similar SSE/MSE ratio to the sample we want to apply the cut to. The offset calibration performed using the DEP (DEP-based cut) is hence appropriate for $0\nu\beta\beta$ signals. Additional calibrations are instead required to study the acceptance of the backgrounds due to cosmogenic ^{68}Ge (MSE sample) and ^{60}Co (highly-MSE). To this purpose we used the SEP of ^{208}Tl and of the summation peak (SP) of the two ^{60}Co gamma-lines. The cut acceptance in these regions has been fixed according

¹The peak in the A/E distribution of the DEP region formed by SSE was fitted with a Gaussian function and the offset defined such that the cut is set 2σ below the centroid.

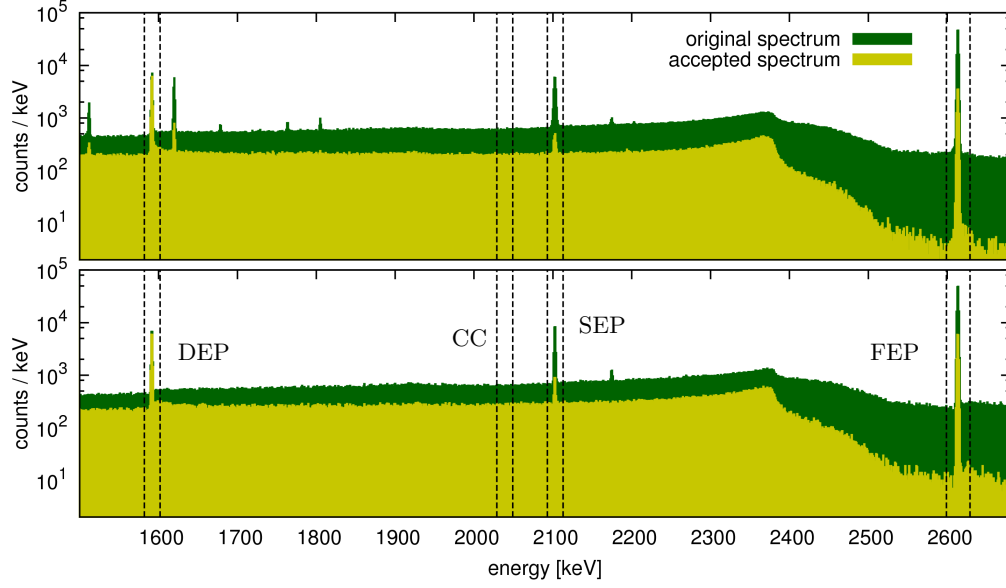


Figure 6.1: (Top) Experimental and (bottom) simulated energy spectrum measured by a BEGe detector irradiated with a ^{228}Th source (^{208}Tl in the simulation). The spectra are shown before and after applying the PSD cut tuned to have 90% acceptance of the DEP. The boundaries of the relevant energy regions are marked with dotted lines.

Table 6.1: Survival probabilities of ^{208}Tl and ^{60}Co induced-events in different regions of interest (ROI) after the PSD cuts. The highlighted values are fixed by the cut calibration. The results for DEP, SEP and FEP of ^{208}Tl , the two ^{60}Co lines at 1173 keV and 1332 keV (FEP1 and FEP2 in the table) and their Summation Peak (SP) are calculated using the net peak areas. The CC region corresponds to an 80 keV wide section of Compton continuum centered at $Q_{\beta\beta}$. The uncertainties given in parenthesis for the least significant digits include statistical as well as systematic uncertainties. The ^{208}Tl FEP and the ^{60}Co FEP1 lie outside of the range covered by the calibration of A/E energy dependence (1.35 MeV to 2.38 MeV) so it can be subject to additional systematic uncertainties.

source	ROI	experimental		simulated			
		DEP		DEP		SEP	SP
		fixed to 90%		fixed to 90%		fixed to 5.5%	fixed to 0.08%
^{208}Tl	DEP	0.900	(11)	0.900	(14)	0.84 (3)	0.61 (15)
^{208}Tl	SEP	0.055	(6)	0.079	(15)	0.055 (3)	0.038 (11)
^{208}Tl	FEP	0.073	(4)	0.12	(2)	0.088 (5)	0.059 (17)
^{208}Tl	CC	0.341	(14)	0.42	(3)	0.357 (17)	0.25 (7)
^{60}Co	FEP1	0.113	(6)	0.138	(17)	0.105 (6)	0.07 (2)
^{60}Co	FEP2	0.106	(6)	0.133	(17)	0.102 (6)	0.07 (2)
^{60}Co	SP	0.00080	(16)	0.0021	(7)	0.0012 (3)	0.0008 (3)
^{60}Co	CC	0.0082	(7)	0.012	(3)	0.0073 (9)	0.0043 (16)

to the experimental results listed in the first column of Table 6.1, i.e. the acceptance was fixed to 5.5% for the SEP (SEP-based cut) and to 0.08% for the SP (SP-based cut).

The survival probabilities computed for the new offset calibrations are shown in the last two columns of the table. The values obtained using the SEP-based cut for the regions with similar SSE/MSE ratio (i.e. the Compton continuum, FEP and SP regions) are in good agreement with the experimental data and compatible within the uncertainties². The SP-based cut results suffer from a higher uncertainty due to the very small number of events remaining in the SP after the cut. Although the cut should be applied to samples of pure MSE, the agreement with experimental data is reasonable for most of the highly MSE-dominated regions.

We can hence conclude that the simulation can be used to estimate the experimental efficiency of the PSD cut, calibrated by fixing the DEP acceptance to 90%. However, this is possible only if the calibration of the cut offset for the simulated data is performed using a sample which has similar SSE/MSE ratio compared to the sample we want to study. The more similar is the event topology, the more accurate is the agreement between simulated and experimental results. In cases when the MSE content of the region used for calibration is higher than in the studied events, the calculated survival probability will be underestimated, and vice versa.

6.1.2 $0\nu\beta\beta$ decay of ^{76}Ge and intrinsic cosmogenic isotopes

In this subsection, the A/E PSD cut is applied to simulations of $0\nu\beta\beta$ events and decays of ^{60}Co and ^{68}Ga homogeneously distributed inside the Ge-detector volume. Figure 6.2 shows the energy spectra of the three processes before and after the PSD cut using the DEP-based cut definition.

The $0\nu\beta\beta$ spectrum shows a peak at the $Q_{\beta\beta}$ energy (2039 keV) and a tail extending to low energies due to the events in which part of the total energy is either lost in the dead layer or escape the detector ($\sim 10\%$ of the total). Since the electrons generated by $0\nu\beta\beta$ decay events have a significant probability to emit a bremsstrahlung photon, not all the events in the $Q_{\beta\beta}$ peak and in the tail are SSE. The MSE contamination is similar to that in the DEP of ^{208}Tl . However, as the energy of the $0\nu\beta\beta$ decay event is higher than in DEP events, also the probability of bremsstrahlung and, in turn, of a MSE interaction is higher. The PSD cut survival probability is thus expected to be slightly lower.

The cosmogenic ^{68}Ge decays via electron capture (EC) into ^{68}Ga , which then decays with 1.13 h half-life into ^{68}Zn via β^+ decay (89% probability) or EC (11%). The positron has an energy end point of 1.9 MeV. To produce events at the ^{76}Ge $Q_{\beta\beta}$ its absorption has to be accompanied by an energy deposition from its annihilation photons. Such events have

²Part of the discrepancy in the ^{208}Tl Compton continuum region is due to the n+ electrode slow pulses which are not included in the simulation. Note that all the values are compatible within 1 sigma, except the ^{208}Tl DEP which is compatible at $\sim 2\sigma$ level.

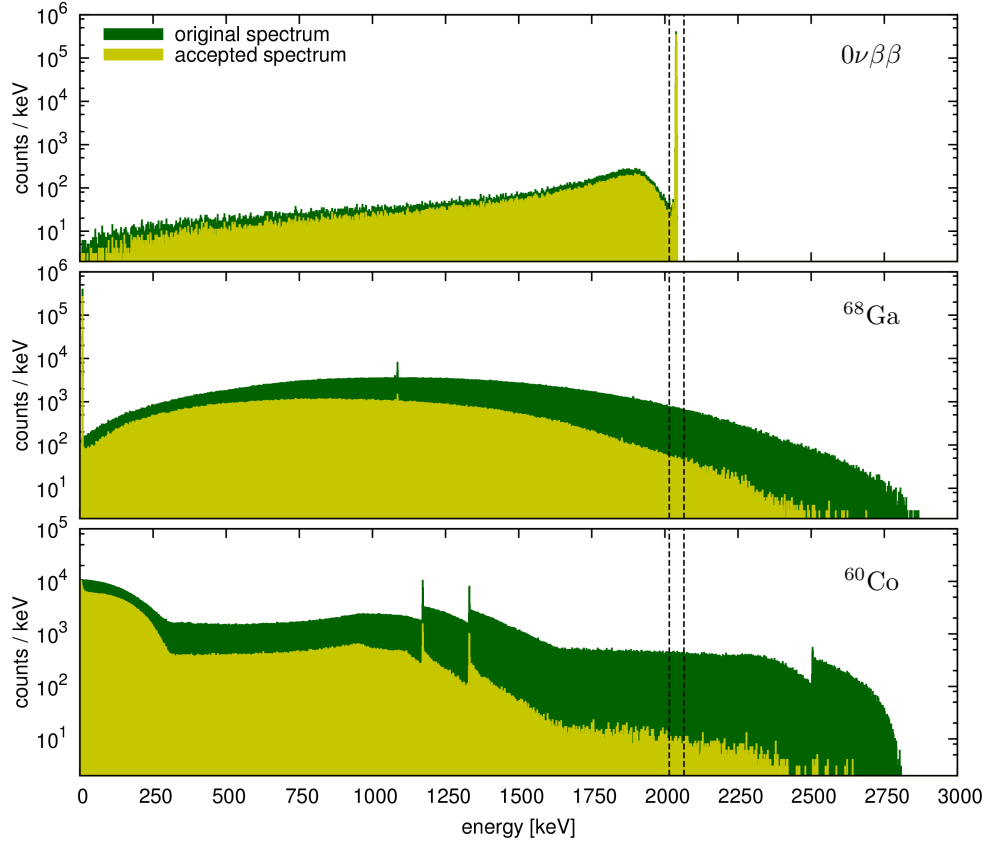


Figure 6.2: (Top) Simulated spectra of $0\nu\beta\beta$ decays, (middle) ^{68}Ga and (bottom) ^{60}Co inside a BEGe detector before and after the PSD cuts.

a topology resembling that of SEP events (strong electron/positron interaction combined with a weaker 511 keV gamma-ray interaction) and are expected to have similar survival probability.

The ^{60}Co spectrum shows the two characteristic peaks at 1173.2 and 1332.5 keV generated in cascade. As the decay occurs inside the detector, the probability of a coincident detection is high, resulting in the summation peak at 2505.7 keV. Moreover, the electron associated to the β^- decay of ^{60}Co to ^{60}Ni (end point energy of 318 keV) is also absorbed leading to the peculiar “triangular” tail at the high-energy side of the peaks. The events in the $Q_{\beta\beta}$ region are a result of the cascade gammas and beta summation and consequently their topologies are highly multi-site.

The survival probabilities in the energy region around $Q_{\beta\beta}$ are reported in Table 6.2 for the DEP-, SEP- and SP-based cut definitions. According to the comparison reported in the previous subsection, we assume that the most realistic value for the survival probability is

Table 6.2: Percentage of survived events of the simulated $0\nu\beta\beta$ decays and internal sources of background after the cut in an 80 keV wide region centered on the ^{76}Ge $Q_{\beta\beta}$. The highlighted numbers represent the most realistic predictions. The uncertainties, given in parenthesis for the least significant digits, include statistical as well as systematic uncertainties. The ^{60}Co result has an additional systematic uncertainty due to the difference on the event topology between the SP region and the studied region.

source	DEP fixed to 90%	SEP fixed to 5.5%	SP fixed to 0.08%
$0\nu\beta\beta$	0.86 (3)	0.77 (3)	0.57 (13)
^{68}Ga	0.063 (11)	0.045 (3)	0.032 (7)
^{60}Co	0.019 (4)	0.0130 (11)	0.009 ($^{+4}_{-2}$)

provided by the cut calibrated in the data region with the most similar event topology, i.e. the DEP-based cut for the $0\nu\beta\beta$ peak, the SEP-based cut and SP-based cut respectively for the Compton continuum region at 2 MeV of ^{68}Ga and ^{60}Co (highlighted values in Table 6.2). The survival probabilities estimated are $(86 \pm 3)\%$ for the $0\nu\beta\beta$, $(4.5 \pm 0.3)\%$ for internal ^{68}Ga decays, and $(0.9^{+0.4}_{-0.2})\%$ for internal ^{60}Co decays. These values represent a reasonable prediction, and are all consistent with the expectations discussed previously: $0\nu\beta\beta$ acceptance is slightly lower than for the DEP, ^{68}Ga survival probability is similar to the values for the SEP, and ^{60}Co suppression is lower than for SP events but still very high.

6.2 Energy depositions on the p+ B-implanted electrode and groove surfaces

This section describes an experimental study of the response of BEGe detectors to energy depositions in proximity of the small p+ electrode and groove. Interactions in this region of the detector were observed to produce peculiar signals with anomalous A/E values (higher than for SSE) [89]. These pulses are reproduced by our simulation and have been traced back to the particular trajectories along which the charge carriers are collected to the electrodes (see Figure 5.5, type II and type III trajectories).

The presence of these events was observed also in the distributions of the rise time and A/E parameter for isotropic ^{228}Th events (see Section 5.3.3). Although the overall distributions of these events are reproduced fairly well by the simulation, we do not expect our modeling to describe precisely the charge collection in this part of the detector. The electric potential gradient is extremely strong near the groove and p+ electrode ($\sim 10^3$ V/mm) and it is affected by geometrical details at the scale of tens of millimeters. However, neither the detector technical drawings nor the grid used to implement the detector geometry reach this accuracy. In addition, surface effects may play an important role while, in the simulation, charges pushed against the detector surface are not propagated. It is thus important to

characterize experimentally this region both to confirm our modeling and to study the PSD rejection efficiency for such events, which are produced by various background sources expected in GERDA Phase II.

To this purpose, the p+ electrode and groove surfaces of a BEGe detector have been scanned using a collimated alpha-beam. Alpha-rays have an attenuation length in Ge of the order of tens of μm and the dead layer covering these surfaces is expected to be $\lesssim 1\ \mu\text{m}$ thick. This measurement is hence expected to provide information about the small dead volume and possible unforeseen surface effects. The results of the first scan are presented in this section. The project has been a collaborative effort of the GERDA group at the Technical University of Munich (TUM). The author contributed by developing and performing the data processing and analysis discussed in the following. More details concerning the experimental setup and the analysis can be found in Ref. [113].

6.2.1 Experimental setup and data acquisition system

The scan of the p+ electrode and groove surfaces with collimated alpha-rays has been performed by installing a BEGe detector in a custom-made cryostat specifically designed to host a movable collimator. The collimator is $\sim 5\text{ cm}$ long and has a 1 mm diameter hole. Its position can be set with a $\lesssim 1\text{ mm}$ precision. The angle between the collimator – i.e. the direction of the alpha-beam – and the p+ electrode surface can be adjusted, but only opening the cryostat. In the considered data set the angle was fixed to 67° . This value has been chosen to irradiate both the inner and the outer lateral surfaces of the groove in the same set of measurements. In this configuration, the diameter of the p+ electrode surface irradiated by the alpha-beam is $\sim 1.6\text{ mm}$. A sketch of the detector surface hit by the beam for various positions of the collimator is shown in Figure 6.3.

In the considered set of measurements, the alpha-beam has been generated by using a 36 kBq ^{241}Am source. The energy distribution of the alpha-particles emitted was measured by a silicon detector and it is shown in Figure 6.4. The energy spectrum has a broad peak centered at $\sim 4.1\text{ MeV}$ with a FWHM of $\sim 0.35\text{ MeV}$. The absence of sharp peaks at the alpha-emission energies of ^{241}Am is an intrinsic property of this particular source related to its age.

The detector installed in the setup is an experimental large-mass BEGe detector produced by Canberra Industries in collaboration with the GERDA group at TUM. The detector is made from natural Ge material and it is one of the largest-mass BEGe-type detector ever built by the manufacturer (1.018 kg). The detector has a diameter of 72 mm and a thickness of 52 mm. Its operational bias voltage is between 3.5 and 5 kV. The depletion of such a large crystal is possible thanks to a careful choice of the net impurity concentration. The net acceptor concentration has a gradient along the symmetry axis of the detector and changes from 0.7 to $-0.2 \cdot 10^{10}\text{ atoms/cm}^3$. The germanium material is p-type in the section

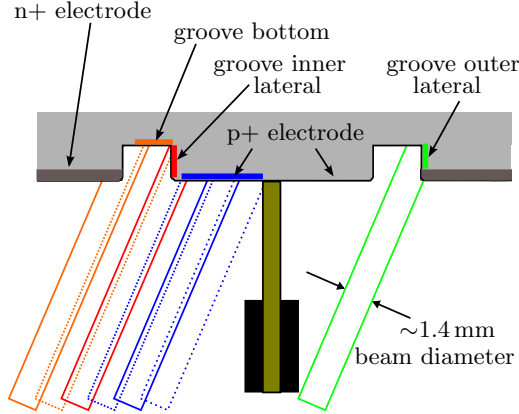


Figure 6.3: Sketch of the detector p+ electrode region. The alpha-beam position and the surface irradiated is shown for a selection of measurements. The pin electrode used to read-out the signal (drawn in brown) shielded a significant part of the p+ electrode.

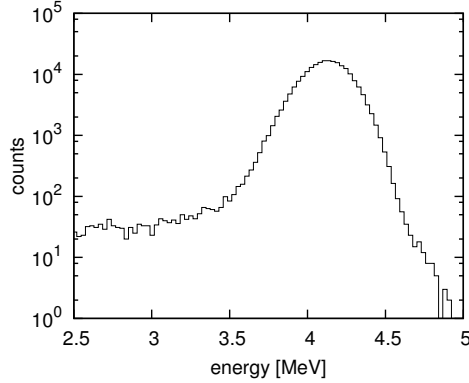


Figure 6.4: Energy spectrum of the ^{241}Am source installed in the setup as measured by a passivated implanted planar silicon (PIPS) detector.

of the crystal close to the p+ electrode. The acceptor and donor concentration is fully compensated at a distance of ~ 4 cm from the p+ electrode and the remaining part of the crystal is n-type. The electrode scheme of this detector has been adapted to the crystal features to optimize the PSD capabilities. In particular, the p+ electrode dimension has been reduced by 20-30% compared to the standard geometry. Before being operated in our setup, the detector was characterized in the original vacuum cryostat provided by the manufacturer. Its spectroscopy performances were found to be good and compatible with standard BEGe detectors.

During the operation of the detector in our custom-made cryostat, we observed an extremely high rate of pulses induced by electrical discharges. The origin of these discharges is presently not understood. It is however related to our setup, since discharges were not observed during the previous operation of the detector in the original cryostat. Traces containing discharges have been rejected off-line by applying proper quality cuts. The issue is discussed in the following section.

The setup is operated in the TUM underground laboratory (15 m.w.e) to reduce the cosmic-ray background. It is shielded with lead layers to screen the detector from natural radioactive gamma-sources and covered by a 1 m^2 plastic scintillator panel for further suppression of muon-induced events.

The detector front-end read-out is performed by the standard charge sensitive preamplifier provided by Canberra (model 2002CSL [49]). The output signal is sampled by a 14 bit FADC running at 100 MHz sampling frequency (Struck SIS 3301 [114]) and stored to disk

for off-line analysis. The plastic scintillator signals of the muon-veto system are shaped by a spectroscopy amplifier with an integration time of $1\,\mu\text{s}$ and then recorded by the FADC in coincidence with the Ge channel.

6.2.2 Data processing and selection

The off-line analysis was performed using the GELATIO framework. The Ge and PMT channels have been processed along two independent chains of modules. The HPGe signals were processed along the same module chain described in Section 2.2.1. The off-line energy reconstruction provides a resolution of $\sim 3.2\,\text{keV}$ at the $2.6\,\text{MeV}$ gamma-line, slightly worse than the value achieved in the standard vacuum cryostat provided by the manufacturer ($\sim 2.5\,\text{keV}$). The PMT traces – shaped by the spectroscopy amplifier – are analyzed with a leading-edge discriminator to identify muon-induced signals (*TriggerModule*). The events with Ge trace saturating the FADC dynamic range – typical of muon induced events – have been used as a pure sample of muon events for an accurate definition of the time-correlation between the two channels ($\sim 1\,\mu\text{s}$) and to assess the muon-veto efficiency. The latter has been estimated to be $\sim 75\%$, limited by the absence of scintillation panels on the side of the setup and by muon-induced showers.

The data selection and definition of the quality cuts have been crucial parts of the analysis because of the extremely high rate of electrical discharges occurring during the measurements. The signals induced by discharges have the same polarity as the physical pulses and a similar shape. Traces containing only pulses induced by discharges are not problematic for our analysis. They have relatively low amplitude and are thus reconstructed at low energy. However, when discharges occur in coincidence with physical events, the parameters extracted by the off-line processing are altered (e.g. the energy is overestimated). This kind of events – which could bias the analysis results – create a continuum distribution in the energy spectrum extending up to high energy.

The quality cuts applied to the data are based on the same parameters discussed in Section 2.2.2. The traces generated by discharges occurring in coincidence with physical signals resemble pile-up events and can be discarded using the same filters. The quality cuts have been tuned using calibration data produced by a ^{228}Th source placed externally to the cryostat. The amount of discarded events is $\sim 70\%$ in the Compton continuum regions, which are dominated by physical events piling-up with discharges, and $\sim 20\%$ of the net counts in the full absorption peaks, which are formed by pure physical events. The pulses reconstructed in the region of interest (energy of the alpha-induced signal) have been visually inspected and found to be all compatible with physical events. Given the amount of events rejected and the possibility of introducing biases in the analysis, we carefully monitored the stability of the cuts in various energy regions (including gamma-lines and Compton continuum) over the full data taking.

An illustrative energy spectrum, reconstructed by a 63 h measurement during which the alpha-beam was irradiating the p+ electrode surface, is shown in Figure 6.5 before and after the application of the quality cuts. The energy region below 2.6 MeV is dominated by the natural radioactivity. Several prominent gamma-lines are present, including the ^{208}Tl 2615 keV gamma-line (^{232}Th decay chain) whose signal has a high statistical significance. The high energy part of the spectrum shows a continuum event distribution due to non-vetoed muons and a broad peak at ~ 4 MeV due to the alpha-induced signal (see Figure 6.4).

6.2.3 Data analysis

The set of measurements presented in this section has been performed by moving the collimator in steps of 1.5 mm along a diameter of the detector, from one side of the groove to the other. As shown in Figure 6.3, the measurements are grouped according to the type of surface irradiated: *a)* p+ electrode surface; *b)* groove inner later surface; *c)* groove bottom surface; and *d)* groove outer lateral surfaces. For each position of the collimator, data have been taken for 1 to 3 days to accumulate at least a thousand counts in the alpha peak (after quality cuts). Long measurements were needed to compensate the low activity of the source, the flux reduction caused by the use of the collimator, and the large amount of events discarded by the quality cuts. The data set includes also calibration runs performed by placing a ^{228}Th source outside the detector cryostat and background runs (measurements in which the alpha-beam aims at the thick n+ layer providing no signals). The effective live time of each measurement after quality cuts is estimated using the number of counts in the background gamma-line at 2.6 MeV and it is $\sim 20\%$ of the measurement time.

In the first part of the analysis, the signal pulse shape and the charge collection efficiency have been studied as a function of the region irradiated by the alpha beam. The signals reconstructed in the alpha peak have been visually checked and no unexpected pulse shapes were observed. Since the beam is not point-like and the different types of surface can be irradiated at the same time, we computed the average signal which is statistically more significant than single pulses³. The average signals reconstructed from a selection of measurements is shown in Figure 6.6. Their shape is consistent with the modeling discussed in the previous chapter.

The charge collection efficiency was studied by comparing the energy distribution of the alpha-induced events with the spectrum shown in Figure 6.4. In particular, a shift of the central value of the distribution is proportional the thickness of the dead layer and to the loss of charges occurring during their transportation to the electrodes. A deformation of the peak shape is instead expected if significant variations of detector response occur on the scale of tenths of millimeters (over the irradiated region). The peak measured by irradiating

³The calculation has been performed by using the *AveragePulseModule* implemented in GELATIO. The algorithm, described in detail in Appendix B, is designed to ensure the convergence of the average to the most frequent pulse shape of the sample.

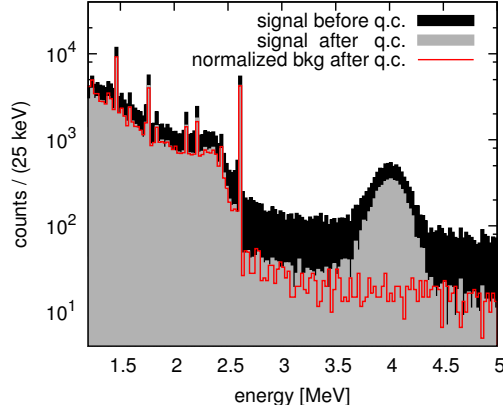


Figure 6.5: Energy spectrum before and after quality cuts (q.c.) measured by irradiating the p+ electrode with the alpha-beam. The background spectrum is normalized according to the intensity of the 2615 keV gamma-line.

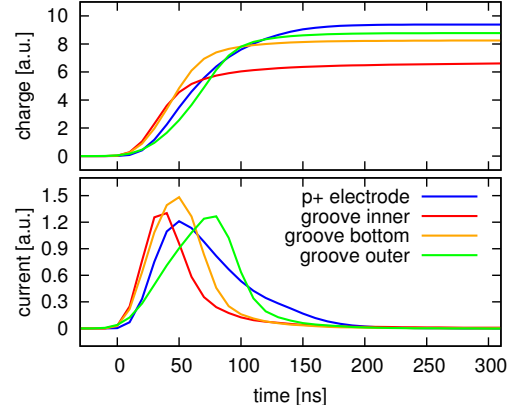


Figure 6.6: Selection of average charge and current signals induced by alpha-interactions on the p+ electrode and groove surfaces. The signals have been aligned using a leading-edge discriminator.

the p+ electrode is shown in Figure 6.5. Its shape is unchanged and its central value is shifted at lower energies of 138 ± 3 keV. Using Monte Carlo simulations, we converted the energy shift in a dead layer thickness of 519 ± 15 nm (computed taking into account the beam incidence angle). Given the B-implantation depth provided by the manufacturer (~ 300 nm), our result may indicate the presence of additional material on the detector surface or that the dead layer extends beyond the p+ electrode. Much stronger shifts along with distortions of the peak shape have been observed for interactions on the groove surfaces. The topic is not discussed in this analysis because of the low counting statistic and the broad energy distribution of our alpha-source, which makes difficult to deconvolve the detector response. Further studies are planned in the next future with more detectors and alpha-sources providing sharp energy peaks.

The second part of the analysis aimed at investigating the potential discrimination efficiency for surface events achievable with PSD techniques. To this purpose, we first focused on the A/E parameter which, according to the simulation results discussed in the previous chapter, is expected to yield optimal discrimination performances (alpha-induced events should be reconstructed at higher A/E values than SSE). Before computing the parameter A , the signals have been integrated with a four-fold 50 ns moving average (*MWAverageModule*), differentiated and interpolated down to 1 ns (*CurrentPSAModule*).

The A/E event distribution as a function of the energy is shown in the left panels of Figure 6.7, divided according to the type of surface irradiated. The low-energy part of the plot is dominated by background gamma-lines. The 2.6 MeV gamma-ray from ^{208}Tl creates the usual SSE band (high-density region at $A/E \sim 1$) and the corresponding MSE

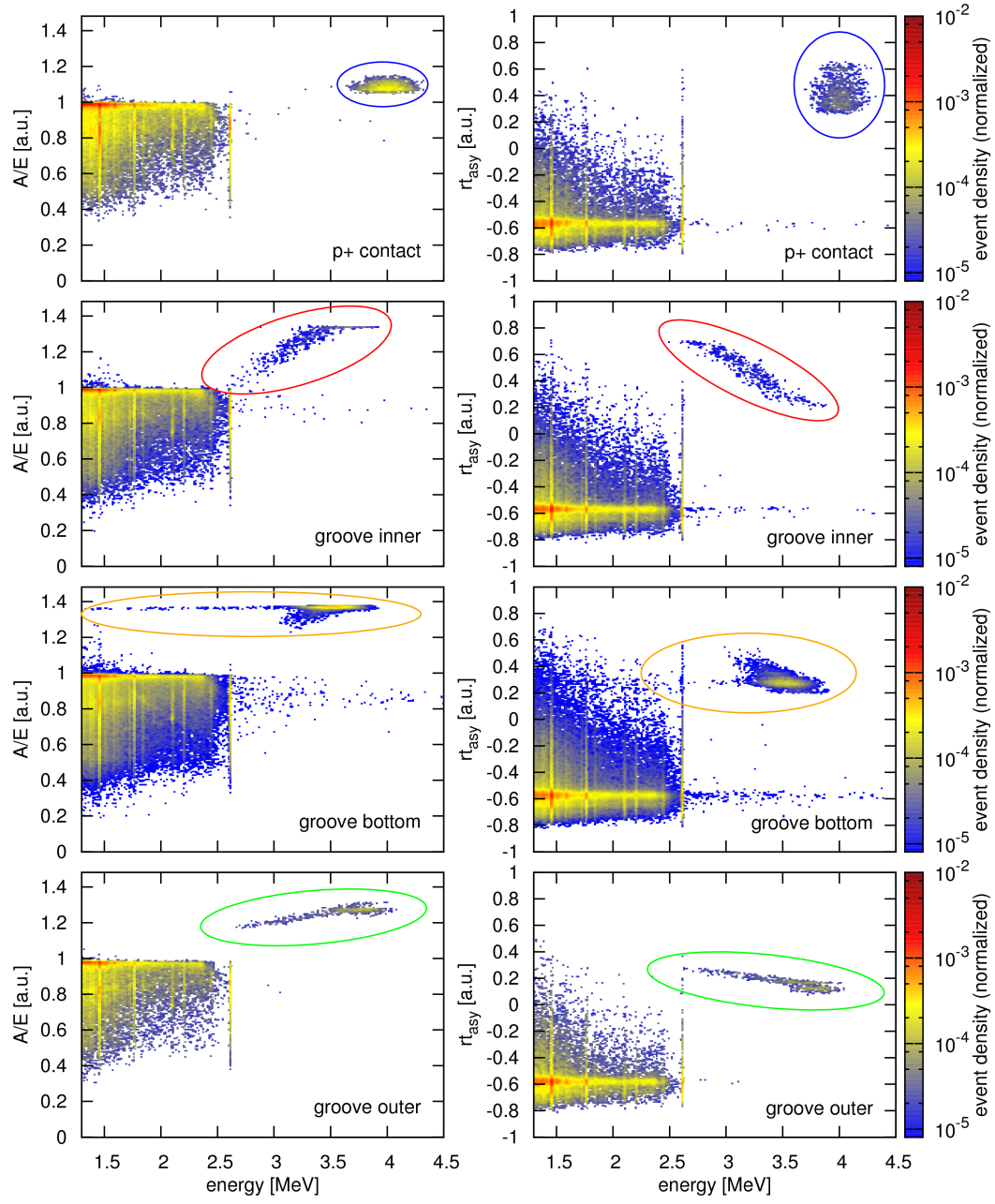


Figure 6.7: (Left) Experimental distributions of the A/E and (right) rt_{asy} parameters as a function of energy. The events due to alpha-interactions on specific detector surfaces are indicated by ellipses.

Table 6.3: Survival probabilities of alpha-induced events occurring in different parts of the detector surface. The values are computed averaging the measurements in which the same surface type was irradiated and correcting for the background (reason why a few survival probabilities are negative). The last line of the table gives the average survival probability weighted for the area covered by each type of surface in a standard detector (as Phase II detectors). The upper limits are given at 95% C.I. assuming Gaussian distributions. The computation was performed using a Bayesian approach and assuming for the survival probability a flat prior probability distribution defined between 0 and 1.

surface	(A/E) -based cut		$(A/E + rt_{\text{asy}})$ -based cut	
	survival prob.	upper limit	survival prob.	upper limit
p+ electrode	0.004 ± 0.004	0.012	0.003 ± 0.004	0.011
groove inner	0.062 ± 0.035	0.121	0.057 ± 0.035	0.116
groove bottom	-0.001 ± 0.005	0.010	-0.001 ± 0.005	0.010
groove outer	-0.002 ± 0.006	0.011	-0.002 ± 0.006	0.011
surface weighted average	0.012 ± 0.037	0.080	0.011 ± 0.036	0.079

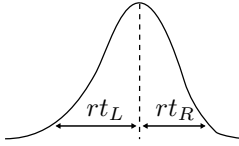
distribution extending at lower A/E values. At high energy, the spectrum shows a continuum distribution of MSE events induced by non-vetoed muon. The alpha-induced events cluster in the energy range between 2.6 MeV and 4.3 MeV and are reconstructed at higher A/E values compared to SSE events. However, the cluster formed by interactions on the inner lateral surface of the groove gets close to the SSE band at low energy.

For rejecting alpha-induced events, the A/E cut discussed in Section 6.1.1 has been extended to discard both the events below and above the central value of the SSE A/E distribution. It thus accepts only the events in a band of the A/E plots in Figure 6.7 and is defined by three parameters: a slope, a lower offset and an upper offset. The slight slope due to the energy dependence of the A/E parameter is computed from the ^{228}Th calibration data, using the Compton continuum regions of the 2.6 MeV gamma-line. The lower and upper offsets are defined independently by fixing the net acceptance of the DEP to 90% and 1% respectively. The final survival probability of double escape events is hence 89%. Although alpha-induced events seems to occur only above the SSE band, we decided to reject also the events below the band to minimize the influence of muon-induced background events and improve the accuracy of our estimates.

The results of the cut, combining in quadrature statistical and systematic uncertainties, are summarized in Table 6.3. The survival probabilities are given as fraction of the events surviving the PSD cut in the energy window containing the alpha-signal. The number of events before and after the cut is corrected for the background normalized using the effective live time. To evaluate the systematic uncertainties resulting from the choice of the energy window edges, the computation has been repeated varying the window position of ± 50 keV with 1 keV step. The results obtained confirm the expected good discrimination capabilities

of the A/E parameter. In general, all the survival probabilities are compatible with zero ($\lesssim 1\%$ at 95% C.I.). Only the value computed for interactions on the inner lateral surface of the groove is slightly higher, $(6.2 \pm 3.5)\%$, probably because of background fluctuations. However, considering that the cluster created by these type of events is the closest one to the SSE band (see red ellipse in Figure 6.7), this result could also be related to an actual inefficiency of the cut.

To exclude inefficiencies of the A/E cut, a new PSD parameter has been developed and applied to the data. The parameter, named “rise time asymmetry” parameter, is defined as:

$$rt_{\text{asy}} = \frac{rt_R - rt_L}{rt_R + rt_L}$$


The diagram shows a symmetric bell-shaped curve representing a current pulse. A vertical dashed line marks the peak. Two horizontal arrows, labeled rt_L and rt_R , extend from the peak down to the 10% amplitude level on the left and right sides of the curve, respectively, indicating the rise times.

where rt_R and rt_L are the rise times of the current pulse computed by moving forward and backward from the highest current peak down to the 10% of the peak amplitude. The rt_{asy} parameter is expected to assume positive values for interactions close to the p+ electrode – generating signals with the current peak at the beginning of the signal – and negative values for interactions in rest of the detector volume – for which the current peak occurs at the very end of the signal. The distribution of rt_{asy} as a function of energy is shown in the right panels of Figure 6.7. Before computing the parameter, the signals were processed along the same filters used to extract A . The events in the low-energy part of the spectrum and the muon-induced events are mostly reconstructed at negative values of the rt_{asy} parameter and create a high-density band at $rt_{\text{asy}} \sim -0.55$. Alpha-induced events are instead reconstructed at positive values.

The overall discrimination performance of the rt_{asy} parameter is worse than A/E . However in the rt_{asy} plot the red cluster formed by the events on the groove inner lateral surface increases its separation from bulk-volume events at low energies, while in the A/E plot it moves toward the SSE band. Consequently, a combined use of the two parameters should improve the suppression factors in case of an actual inefficiency of the A/E parameter. To verify it, we applied the A/E cut in combination with an energy-independent cut on the rt_{asy} parameter accepting only events below 0.15 (88% combined DEP acceptance). The results are provided in the last two columns of Table 6.3. The suppression factors computed are practically unchanged compared to the previous results. We thus conclude that the results obtained for the A/E parameter are not related to an inefficiency of the cut, but rather to an inaccurate background subtraction, which could arise from small variations of the discharge rate over the data-taking.

6.3 Energy depositions in the Li-diffused surface layer forming the n+ electrode

In this section, we discuss the BEGe detector response to energy depositions near the Li-diffused surface layer forming the n+ electrode. The diffusion of lithium is the most common technique used to create the n+ electrodes in p-type HPGe detectors and was already applied with Ge(Li) detectors in the 1960s. Signals with anomalously long rise times, produced by interactions in the region of the Li-diffused material, were reported early in 1964 and attributed to an inefficient charge collection due to a weak electric field region [115]. This idea has been strengthened by successive experimental observations reported by various groups using different detectors (see Ref. [110] for a review of the main results). Nowadays, the existence of a “transition” layer, located between the fully active volume and the fully dead layer formed by the n+ electrode, seems well established [109, 110]. In this region, the dominant charge transportation mechanism is the diffusion. Holes produced in the transition layer are collected to the read-out electrode only if they diffuse and enter in the detector active volume. Given the long collection time, additional charge losses are expected because of trapping and recombination processes.

The occurrence of slow signals was observed also with our BEGe detector in measurements with uncollimated ^{228}Th (see Section 5.3.3). The contamination of slow signals was 3-4% in the Compton continuum region at $Q_{\beta\beta}$ and it was not reproduced by the simulations⁴. These measurements – in which the whole Ge crystal is irradiated – showed that the volume generating slow signals is a non-negligible fraction of the total, but did not provide any information concerning its location inside the detector.

To investigate the issue, we performed additional measurements with low-energy gamma-sources. The results – first presented in Ref. [116] (2010) – provided compelling evidences that the slow pulses observed with our BEGe detector were produced by energy depositions in the n+ layer and confirmed the slow-pulse generation model aforementioned. They also provided strong indications that surface events can be efficiently identified through PSD techniques. This is of particular interest as various background components expected in GERDA Phase II result in surface energy depositions, e.g. beta-rays from ^{214}Bi and ^{42}K . To study the suppression efficiency of these backgrounds, a large campaign of measurements with beta-emitting sources and multiple detectors was performed by D. Budjáš. Here we summarize the main results of this work which has been already discussed in details in Ref. [117].

The first set of measurements was performed using uncollimated ^{241}Am . The interaction probability of the 59.5 keV gamma-ray of ^{241}Am follows an exponential profile $e^{-d/\lambda}$, where d is the distance from the surface and $\lambda \sim 0.9\text{ mm}$ is the characteristic interaction length.

⁴The contamination was not reproduced because the transition layer was not implemented in the simulation.

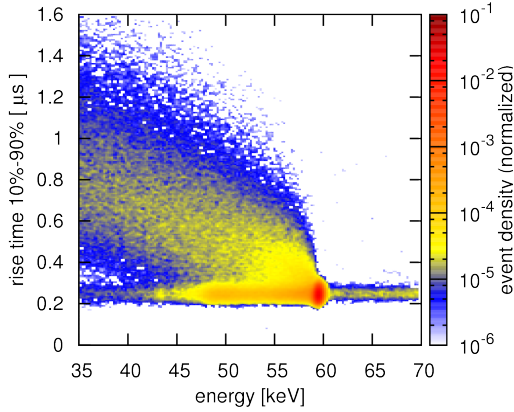


Figure 6.8: Distribution of the rise time 10%-90% in a data set produced by irradiating the detector with an uncollimated ^{241}Am source. The parameter is extracted after interpolating the signals down to 1 ns sampling period.

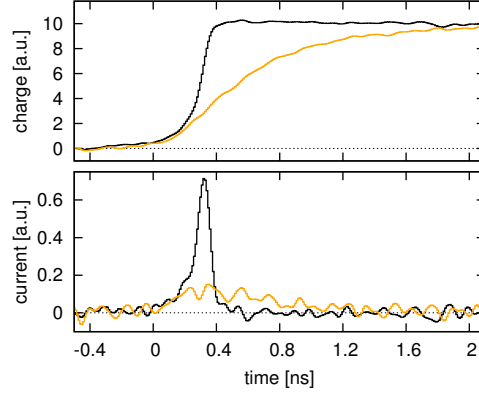


Figure 6.9: Illustrative examples of a standard (in black) and a slow pulse (orange) reconstructed at the same energy. The signals have been integrated by a three-fold 50 ns moving average to reduce the noise and interpolated down to 1 ns sampling period.

Consequently, the whole Li-diffuse layer ($\lesssim 1$ mm thick), up to the detector active volume, was probed in the same measurement. The distribution of the ^{241}Am events as a function of the reconstructed energy and rise time is shown in Figure 6.8 for the same detector considered in the previous chapter (BE3830/S model). All the features of the plot are consistent with the transition-layer model. The events reconstructed at 59.5 keV create a high-density cluster at rise time values around 250 ns. These are events in which the gamma-ray deposits all its energy inside the Ge crystal and the charge carriers produced are completely collected. This implies that the energy is deposited entirely in the fully active volume and the resulting signal has a normal shape (“type I” pulses). Two bands originate from the cluster. The first is horizontal and contains events that, having the same collection time of the ones in the cluster, can be attributed to energy depositions in the fully active volume. The second band is broader and extends to higher rise time values as the energy decreases. It is formed by events in which part of the energy is released in the transition layer. The energy dependence of the band is also consistent with the model. For a given energy deposition, the time needed to collect the hole produced in the transition layer – and hence the pulse rise time – increases with the distance between the interaction site and the active volume. Conversely, the fraction of charge carriers reaching the active volume – which is proportional to the reconstructed energy – decreases for geometrical reasons as the diffusion process is isotropic. Illustrative pulses taken from each band are shown in Figure 6.9.

The peculiar shape of the slow pulses can be exploited for an efficient pulse shape discrimination. As shown in Figure 6.9, slow pulses have broad current signals, with a

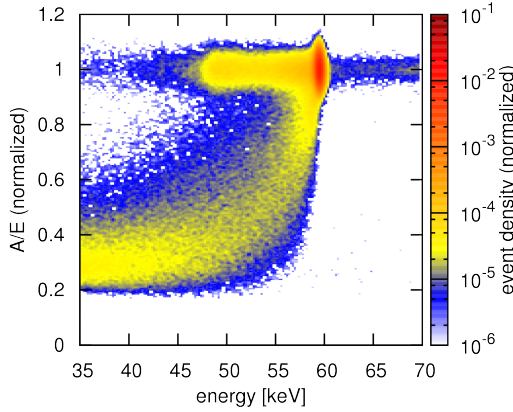


Figure 6.10: Distribution of the A/E parameter in a data set produced by irradiating the detector with an uncollimated ^{241}Am source. The parameter has been extracted after interpolating the signals down to 1 ns sampling period and applying a three-fold 50 ns moving average.

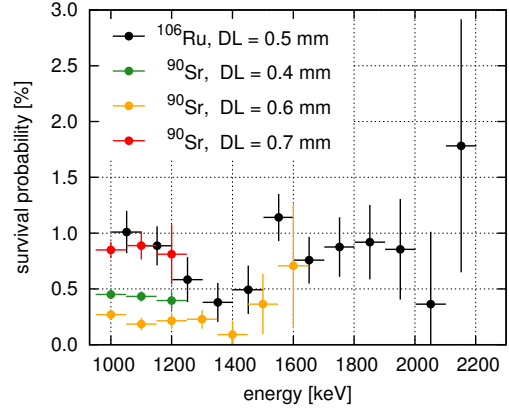


Figure 6.11: Survival probability (in percentage) of surface interactions near the n+ electrode computed as a function of energies for various detector with different dead-layer (DL) thicknesses. The values refer to the standard A/E cut (DEP acceptance fixed to 90%). Adapted from Ref. [117].

significantly lower maximum amplitude compared to SSE pulses. The standard A/E -based cut discussed in the previous sections can hence be used to reject surface interactions along with multiple site events. The effectiveness of such a cut is visible in Figure 6.10, which shows the A/E distribution for the ^{241}Am events as a function of energy. Also in this case we have two bands overlapping in the high-density cluster at 59.5 keV: the horizontal SSE band, at $A/E \sim 1$, and the slow-pulse band, extending to lower A/E values in the MSE region. Given the separation between the two bands, we expected the A/E cut to have a high discrimination efficiency.

To evaluate the performance of the A/E cut on the beta-induced background components expected in GERDA Phase II, further measurements have been performed on different BEGe detectors using beta-emitting sources, i.e. ^{90}Sr and ^{106}Ru . The analysis of these data sets is described in Ref. [117] and the outcome is summarized in Figure 6.11. The plot shows the survival probability obtained with four detectors having different dead layer thicknesses. The values are given according to the standard A/E cut, calibrated to accept 90% of the DEP net area. The survival probability was found to be $\lesssim 1\%$ within the statistical uncertainty for all the measurements performed and for a wide energy range. In particular, the survival probability at $Q_{\beta\beta}$ extracted from the ^{106}Ru data set is $< 1.6\%$ at 95% C.I. (computed similarly to the values in Table 6.3). This result was recently confirmed also by experimental measurements with a BEGe detector operated in the LArGe setup [118]. Considering the relatively large sample of detectors analyzed and the overall stability of the values, this excellent performance can be assumed also for Phase II BEGe detectors.

6.4 Conclusions

The results presented in this chapter show the excellent discrimination efficiency achievable with BEGe detectors and PSD techniques on several background components that are potentially critical for GERDA Phase II. In particular, we focused on the cosmogenic isotopes of Ge, which create simultaneous multiple-site energy depositions inside the Ge crystal, and external sources emitting alpha- or beta-rays, which produce energy depositions on the surface of the detectors. We found that the A/E PSD method can be used to suppress all the considered backgrounds while maintaining a large acceptance of the $0\nu\beta\beta$ signal.

The evaluation of the survival probabilities of decays occurring inside the Ge crystal (i.e. decays of ^{68}Ga , ^{60}Co and $0\nu\beta\beta$ events) was performed using our pulse shape simulation tool. These results are extremely important considering the difficulties of studying these decays experimentally. In addition, this is the first time that a pulse shape simulation tool undergoes a full validation against experimental data and proves to have the accuracy needed to study PSD techniques. The survival probabilities at $Q_{\beta\beta}$ were estimated to be $(86 \pm 3)\%$ for $0\nu\beta\beta$ events, $(0.9^{+0.4}_{-0.2})\%$ for ^{60}Co and $(4.5 \pm 0.3)\%$ for ^{68}Ga . The results are presently dominated by systematic uncertainties related to analysis adjustments developed to overcome the imperfections of the simulation. Nevertheless, they represent a reasonable prediction of the PSD background discrimination efficiency for GERDA Phase II detectors.

The study of surface interactions on the p+ B-implanted electrode and groove surfaces has been performed through scans with a collimated alpha beam. To this purpose, a BEGe detector has been operated in a custom-made cryostat specifically designed to host a movable collimator. The shape of the signals measured was found to be consistent with the BEGe detector modeling presented in the Chapter 5 and no surface effects have been observed. We estimated that the alpha-background survival probability achievable with the parameter A/E is better than 8% at 95% C.I., although measurements on other detectors are needed to check for possible dependences on the Ge material and electrode geometry.

We also investigated the detector response to energy depositions in the Li-diffused layer forming the n+ electrode. As reported in the literature, n+ surface interactions result in signals with long rise time. All data collected support the existence of a transition layer – located between the fully active and fully dead volumes – in which the electric field is negligible and charges move by diffusion. We also showed that the peculiar shape of these slow signals can be exploited to efficiently suppress beta-emitting background sources via PSD. The survival probability at $Q_{\beta\beta}$ was found to be $< 1.6\%$ (95% C.I.) and consistent among detectors with different Li-diffusion profiles. This result is robust and, for similar electronic noise levels, we expect a similar performance with Phase II BEGe detectors.

Chapter 7

Background expectation and experimental sensitivity

GERDA Phase II will start the exploration of $0\nu\beta\beta$ half-life values in the 10^{26} yr range within a few years of data taking. The collaboration plans to reach this sensitivity level by accumulating ~ 100 kg·yr of exposure with a background index $\lesssim 10^{-3}$ cts/(keV·kg·yr). To fulfill these exposure and background requirements, a major upgrade of the experimental apparatus is planned for summer 2013. The upgrade will allow the deployment of additional 30 custom-made BEGe detectors, increasing the target mass of ^{76}Ge from ~ 18 kg (sum of the eight $^{\text{enr}}\text{Ge}$ coaxial detectors) to ~ 38 kg. In addition, new devices will be installed to detect the liquid-argon scintillation light, which will be used as anti-coincidence veto to reject background events.

In this chapter, we discuss the background composition expected in GERDA Phase II. In Section 7.1, the background model developed in Chapter 3 for Phase I is adapted to account for the hardware upgrades. Section 7.2 summarizes the active techniques for background reduction that will be applied in Phase II – e.g. the PSD techniques discussed in Chapter 6 – and their efficiencies. Finally, our expectations regarding the sensitivity for the $0\nu\beta\beta$ search and the background surviving the analysis cuts are presented in Section 7.3. The expectation values provided in this chapter are given under the assumption that all the current R&D activities for GERDA Phase II will be completely successful. The most critical issues are summarized and discussed in Section 7.4.

7.1 Backgrounds expected in Phase II configuration

The upgrade planned to expand the detector array affects several parts of the experimental apparatus, in particular the detector mounting and the string lock-system. The new detectors will be deployed in additional strings with low-mass holders designed according to the BEGe

detector geometries. The cables and the front-end electronics will also be optimized to take full advantage of the low capacitance of BEGe detectors and their PSD performance.

The Phase II upgrade includes also the installation of new devices to detect the liquid argon (LAr) scintillation (XUV light emitted at 128 nm), which is produced by charged particles or radiation depositing energy in the LAr volume. The simultaneous detection of a signal in the Ge detectors and the LAr scintillation light can thus be used to suppress background sources generating events with multiple energy depositions. The instrumentation of the GERDA LAr volume will rely on the combined deployment of low-background photo-multipliers (Hamamatsu, model R11065-10) – the same technology used in the LArGe setup [94] – and WLS (wavelength shifting) fibers read-out with Si photo-multipliers [119]. To ensure a good detection efficiency of the LAr scintillation signal produced by interactions near to the detectors, a redesign of the Phase I mini-shroud will also be necessary.

As discussed in the first part of the dissertation, the mini-shroud is a cylinder made from a 60 μm Cu foil. It was not present in the original design of GERDA and has been introduced to isolate the LAr volume immediately surrounding the detectors from the rest of the cryostat. This solution was adopted to mitigate the background induced by the ^{42}K ions, progeny of a cosmogenic isotope of argon. This isotope contributes to the background at $Q_{\beta\beta}$ through its 3.5 MeV beta-ray, which can reach the detector surface only when the decay occurs within a few millimeters of distance. The mini-shroud serves a twofold purpose: it screens the electric field induced by the detector bias voltage, avoiding the attraction of ^{42}K ions, and creates a physical barrier that prevents ^{42}K ions from being transported close to the detectors by the convective flows of LAr.

The mini-shroud design for Phase II has to ensure a strong suppression of the ^{42}K background and an efficient transmission of the LAr scintillation signal. The current solutions rely on Cu meshes, for the electrical decoupling of the inner and outer space, and hermetic vessels, for a physical separation of the two volumes. While meshes are directly transparent to the XUV light, the hermetic vessels will be made from a material transparent to the visible light and, at the same time, able of wavelength-shifting the XUV light¹. Prototypes are presently under test in the LArGe setup and the first results are promising.

The background level and composition expected in the final Phase II configuration have been computed using the Phase I background decomposition discussed in Chapter 3. The contribution of each background source identified in Phase I is reported in the first columns of Table 7.1, separated according to the signal induced in the detectors (type of particle emitted in the decay and location of the energy depositions). For each background contribution, the table shows the expected value in the Phase II configuration and the list of factors that determine a variation of the rate. The table differentiates between coaxial and BEGe detectors as the background expectations are usually different. In particular,

¹Currently considered designs include mini-shrouds made of nylon coated with a WLS material, or plastic scintillators, e.g. polyvinyltoluene PVT and polystyrene PS, able to shift the XUV light.

Table 7.1: Background components at $Q_{\beta\beta}$ in GERDA Phase I and expectations in the final Phase II configuration without analysis cuts. The components are separated according to the radioactive isotope, the decay position and the type of particle interacting inside the detectors. For each entry we list the hardware changes that will affect its count rate and for which we apply a corrective factor to the Phase I rate. All the values are provided in units of 10^{-3} cts/(keV·kg·yr), the background goal of Phase II. The last entry is the sum of the count rates of each contribution, given by the best value (when available) or the upper limit. The final value is thus an overestimation of the expected BI, as it is clearly visible from the comparison with the experimental rate measured in Phase I.

			Phase I	coaxial detectors		BEGe detectors	
Signal			BI	Phase II config	BI	Phase II config	BI
^{214}Bi	γ		$\lesssim 10.0$	MS/etching	$\lesssim 1.0$	MS/etching	$\lesssim 1.0$
	β	n+ elect	2.1	etching	0.2	etching/S-V/DL	6.5
	β	p+ elect	<0.3		<0.3	S-V	<0.1
^{208}Tl	γ		$\lesssim 10.0$	MS/etching	$\lesssim 1.0$	MS/etching	$\lesssim 1.0$
^{42}K	γ		<2.0		<2.0		<2.0
	β	n+ elect	<0.1		<0.1	S-V/DL	<3.2
	β	p+ elect	2.9		2.9	S-V	1.3
^{210}Po	α	p+ elect	1.1	$T_{1/2}$	<0.1		<0.1
^{222}Rn	α	p+ elect	1.5		1.5	S-V	0.7
^{60}Co	β/γ	int	<1.3	$T_{1/2}$	<1.0		<0.3
^{68}Ge	β/γ	int	—		—		<2.3
Sum			<32 (20^{+6}_{-4} measured)		<10.1		<18.5

the expectations for background sources producing surface energy depositions are corrected to account for the different detector geometry, i.e. the surface to volume ratio, and the thickness of the n+ electrode dead-layer. The scaling factors used to compensate for the surface/volume ratio of BEGe detectors are ~ 1.6 for the n+ electrode surface and ~ 0.4 for the p+ electrode and groove surfaces (labeled as “S-V” factors in Table 7.1). The variation of the n+ dead layer thickness on beta-induced background has been estimated by means of Monte Carlo simulations and found to be corrected by a factor ~ 20 (“DL” factor, computed assuming an average value of 2 mm for coaxial and 1 mm for BEGe detectors).

The changes expected in comparison to the Phase I background model can be summarized as follows:

- **^{214}Bi and ^{228}Th :** these isotopes were found to be the dominant component of the Phase I background, providing a count rate of $\sim 10^{-2}$ cts/(keV·kg·yr) at the $Q_{\beta\beta}$ energy. According to the results of screening measurements [120] and Monte Carlo simulations, the U and Th activity seems to be concentrated in the mini-

shroud material and/or on the detector Li-diffused n+ surface [121]. In this case, the contamination could in principle be reduced by a selection of the material used to produce the Phase II mini-shrouds and/or by etching the outer Li-diffused surface of the crystals. These operations would lower the total background index to the level due to the contamination in the holders and cables, which is expected to be at the level of $\sim 10^{-3}$ cts/(keV·kg·yr). These expectations are included in Table 7.1 by applying a scaling factor of 0.1 on the Bi and Th backgrounds (labeled as “MS/etching” factor). To provide a conservative estimate, we do not take into account the further background suppression expected by the reduction of the material used in the BEGe detector strings with respect to the Phase I setup (about a factor 3 w.r.t the total mass of detectors deployed).

- **^{42}K :** the new generation of mini-shrouds could, in principle, reduce the ^{42}K background as compared to the Phase I solution. However, the experimental validation of the new concepts is at an early stage and the potential improvements cannot be quantified yet. We thus make the simple assumption that the new design will be equivalent to the previous one concerning the mitigation of the ^{42}K background, but, at the same time, it will transmit the LAr scintillation signal allowing the detection of energy depositions inside the mini-shroud volume.
- **^{210}Po :** the ^{210}Po contamination observed in Phase I – which was mainly due to a single detector – likely occurred during the refurbishment process at Canberra. The estimation of the ^{210}Po background in Phase II is performed by taking the present activity and rescaling it according to the half-life of this isotope ($T_{1/2} = 138$ d). The estimation for BEGe detectors is based on data collected with five $^{\text{enr}}\text{Ge}$ BEGe detectors in the GERDA setup. The values reported in Table 7.1 are averaged over the first three years of Phase II (assuming fall 2013 as starting point for physics analysis).
- **^{222}Rn :** This background component is still not fully understood. Its presence was not assessable from the data set analyzed in Chapter 3 because of the low counting statistics. However, the signals due to the decay chain of ^{222}Rn have been identified in a recent analysis based on the total data set available [81]. The comparison of data and Monte Carlo simulations favors scenarios in which ^{222}Rn decays in the LAr volume next to the detectors, providing a BI of $1.5 \cdot 10^{-3}$ cts/(keV·kg·yr). Given the absence of additional information, we assume this value also for coaxial and BEGe detectors in the Phase II configuration. However, the validity of this assumption should be thoroughly investigated in the next future.
- **^{60}Co and ^{68}Ge (cosmogenic):** The activity of the cosmogenic isotopes in Phase I detectors refers to the values reported in Ref [48]. The expectations for BEGe detectors are instead based on the total exposure to cosmic rays accumulated during the detector

production chain [111]. The values are corrected for the isotope half-lives – 5.3 yr for ^{60}Co and 271 d for ^{68}Ge – and averaged out over the first three years of Phase II.

Under these assumptions and considerations, the background index for the coaxial detectors operated in Phase II is $< 10 \cdot 10^{-3}$ cts/(keV·kg·yr) before any analysis cut, about a factor 3 lower than in Phase I. The total background budget will not be dominated by a specific component, but rather split among several sources, i.e. ^{214}Bi , ^{208}Tl , ^{42}K , ^{222}Rn and cosmogenic ^{60}Co . The BI expected for BEGe detectors before analysis cuts is $< 19 \cdot 10^{-3}$ cts/(keV·kg·yr). The estimate is higher than for coaxial detectors mainly because of the thinner n+ dead-layer, which is less effective in shielding beta-rays, and a higher activity of cosmogenic short-lived ^{68}Ge . It should be noted that the background due to ^{42}K beta-rays was computed assuming the scenarios providing the highest count rate compatible with the measured concentration and, consequently, is likely to be lower than the values quoted.

7.2 Active techniques for background reduction

The background expectations presented in the previous section are consistent with the design of the GERDA apparatus [39]. To achieve the background index of 10^{-3} cts/(keV·kg·yr), Phase II will rely on active techniques for background reduction. These are: *a*) pulse shape discrimination (BEGe detectors); *b*) multiple detector / LAr scintillation anti-coincidence (all detectors); and *c*) time coincidence (all detectors). The surviving probabilities of each background source expected in Phase II after the application of the analysis techniques are summarized in Table 7.2.

Pulse shape discrimination techniques provide a powerful tool to extract, from the signal time-structure, information about the spatial distribution of the interaction sites inside the detector. As discussed in Chapter 6, the application of these techniques in combination with BEGe detectors allows the suppression of several background sources. For our estimate, we refer to the survival probabilities at $Q_{\beta\beta}$ evaluated for the *A/E* method in Chapter 6 and Ref. [89]. These are: 20-25% for ^{214}Bi and 35-45% for ^{208}Tl and ^{42}K gamma-induced backgrounds²; <8% for alpha- and beta-induced interactions on the B-implanted p+ electrode and groove surface³; < 1.6% for beta-rays penetrating the detector through the Li-diffused n+ electrode; <1% and <5% for, respectively, ^{60}Co and

²The survival probabilities for these isotopes is proportional to the SSE/MSE composition of the Compton Continuum at $Q_{\beta\beta}$. This is proportional to the probability that cascade gamma-rays generate summation events, which, in turn, depends on the particular decay scheme of the isotope and on the distance between source and detector. The survival probabilities of ^{214}Bi and ^{208}Tl were directly measured, while for ^{42}K is conservatively taken equal to ^{208}Tl .

³Note that the survival probability was measured for alpha-rays on the p+ electrode and is here extended to beta-rays. This is well motivated since, according to our detector modeling, the two types of events are expected to induce similar pulse shapes. The assumption was recently confirmed by direct measurements with beta-sources [122].

Table 7.2: Survival probabilities at $Q_{\beta\beta}$ of the background components expected in GERDA Phase II after the application of active background reduction techniques. The values are conservatively given for the scenarios providing the lowest suppression efficiency. The values of the anti-coincidence cut are given as average of all detectors (BEGe and coaxial), with the exception of the value for ^{68}Ga which is given only considering BEGe detectors (this background is absent in coaxial detectors).

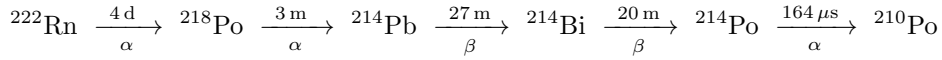
	Signal	BEGe PSD	Detector & LAr anti-coincidence	BEGe time coincidence
^{214}Bi	γ	0.25		—
	β n+ elect	<0.016	$\lesssim 0.2$	—
	β p+ elect	<0.08		—
^{208}Tl	γ	0.4	<0.01	—
^{42}K	γ	0.4	0.1	—
	β n+ elect	<0.016	—	—
	β p+ elect	<0.08	—	—
^{210}Po	α p+ elect	<0.08	—	—
^{222}Rn	α p+ elect	<0.08	—	TBD
^{60}Co	β/γ int	0.01	$\lesssim 0.05$	—
^{68}Ga	β/γ int	0.045	0.2	0.24

^{68}Ga (^{68}Ge progeny) decaying internally to the Ge crystal. In the following we will not consider PSD techniques applied to the coaxial detectors since their development is still in a very early stage and their potential efficiency unclear.

The anti-coincidence cut is used to reduce the background due to sources that produce simultaneous energy depositions spatially separated, e.g. ^{214}Bi and ^{228}Th , which decay emitting gamma-rays. It is applied when a signal occurs in coincidence with a trigger in other detectors or with the detection of the LAr scintillation light. The detector anti-coincidence cut was already applied in Phase I. However, the increased granularity of the Phase II detector array – which will be composed of almost 40 detectors – will enhance significantly the effectiveness of this cut. The total survival probabilities of the anti-coincidence cut (both multiple-detectors and LAr-veto) have been estimated by means of Monte Carlo simulations. The simulations included the tracking of optical photons [123, 124], which was previously validated against experimental measurements performed in the LArGe setup [94, 95]. The survival probabilities are reported in the third column of Table 7.2. The values are given with respect to the scenario providing the highest survival probability, e.g. ^{214}Bi decays on the n+ surface of the crystals and ^{208}Tl decays far from the detectors. The survival probabilities cover a wide range, given by the different decay scheme of the isotopes considered and the decay location simulated. The survival probabilities at $Q_{\beta\beta}$ are of the order of $\sim 1\%$ for ^{208}Tl

and internal ^{60}Co , 20-30% for ^{214}Bi and internal ^{68}Ga , and $\sim 10\%$ for ^{42}K gamma-rays. The survival probabilities for ^{42}K beta-rays and for the isotopes undergoing pure alpha-decays (i.e. ^{210}Po , ^{222}Rn and its daughters) are assumed to be 100%. These isotopes create events at $Q_{\beta\beta}$ only when the decay occurs next to the detector surface and the alpha- or beta-ray enters the detectors without releasing a significant fraction of its energy in the LAr.

The last technique for background reduction is based on the identification of time correlated events due to the isotopes occurring in a decay chain. This can be used to suppress the background due to the progenies of ^{68}Ge and ^{222}Rn . The decay of ^{68}Ge into ^{68}Ga is associated with the emission of a 10 keV X-ray or Auger electron ($\sim 86\%$ probability) and it is shortly followed by the decay of ^{68}Ga , which is a short-lived isotope with 68 m half-life and Q-value above $Q_{\beta\beta}$. The detection of the ^{68}Ge X-ray will be possible in the GERDA setup thanks to the low capacitance of BEGe detectors, which provides a low noise level and, in turn, a low-energy threshold. The ^{68}Ga background can hence be reduced to 24.4% by rejecting all the signals occurring within 204 minutes from a 10 keV event (three half-lives of ^{68}Ga). The identification of the isotopes occurring in the ^{222}Rn decay chain is also possible but more complicated. The decay sequence is:



(see Table 3.1 for more details). In case of surface contaminations, only a fraction of the decays is detected and the energy information is frequently degraded. In addition, although some steps of the chain could be easily tagged by the combined use of the HPGe detector and LAr-scintillation signals (e.g. Bi-Po coincidences), their identification efficiency is strongly affected by the profile of the detector dead-layer and the spatial distribution of the contamination. The application of a time-coincidence cut to reduce ^{222}Rn -induced background should hence be kept in consideration, however it is premature to make a prediction of its potential suppression efficiency.

The techniques discussed in this section can reduce significantly the background level of GERDA Phase II but, at the same time, they will reduce the detection efficiency of the $0\nu\beta\beta$ signal. In particular, the application of PSD techniques reduces the acceptance of $0\nu\beta\beta$ events. The survival probability of the A/E method was studied in Section 6.1.2 using simulated data and the best estimate was $(86 \pm 3)\%$ for the events in the peak at $Q_{\beta\beta}$. This value should be reduced to $\sim 85\%$ since we use the modified A/E cut defined in Section 6.2.3 which rejects also surface events near the p+ electrode⁴.

The detector or LAr scintillation anti-coincidence cut does not affect the survival probability of the $0\nu\beta\beta$ signals at $Q_{\beta\beta}$, for which all the energy is released inside the

⁴The standard A/E cut – rejecting MSE and slow pulses – is calibrated by fixing the survival probability of double escape events to 90%. The extended version of the cut, which rejects also surface events on the p+ electrode, is calibrated fixing to 89% the DEP survival probability. The reduction of the survival probability for $0\nu\beta\beta$ events can be assumed, to first approximation, equal to the reduction for double escape events.

Germanium crystal. Nevertheless, it reduces the live time of the data set because of the scintillation light produced by ^{39}Ar decays in liquid argon⁵ and the intrinsic dark rate of the PMTs. The former is at the level of 1 kHz, resulting in a dead time of the order of 0.1%. The latter is difficult to predict and it can easily become the dominant contribution. For example, the total dark rate in the LArGe setup is $\lesssim 10$ kHz (for six 8" PMTs), resulting in a $\sim 3\%$ reduction of the live time [94].

The application of the time-coincidence cut results also in a direct reduction of the live time of the data set. In the simple case of ^{68}Ge , an actual identification of the 10 keV X-ray would provide the aforementioned performance with a reduction of the live time of $< 1\%$. However, the count rate in the region of the 10 keV signal can be easily dominated by other background sources, causing a significant increment of the total dead-time introduced by the cut.

7.3 Surviving backgrounds and sensitivity to the $0\nu\beta\beta$ signal

In the previous sections we discussed the expectations concerning the background composition (Table 7.1) and the performances of active techniques for background reduction in GERDA Phase II (Table 7.2). The information is combined in this section to estimate the final BI achievable in GERDA Phase II. The estimates for each background component are reported in Table 7.3, differentiating between coaxial and BEGe detectors.

The starting BI for coaxial detectors is $< 10 \cdot 10^{-3}$ cts/(keV·kg·yr). The application of active techniques is, in this case, limited to the anti-coincidence cut and it results in a reduction of the BI down to $< 5 \cdot 10^{-3}$ cts/(keV·kg·yr). This value is dominated by two components producing surface interactions on the p+ electrode: beta-rays from ^{42}K (55% of the total) and alpha-decays of the isotopes in the ^{222}Rn decay chain (29% of the total). If these two components are not considered, the BI estimate drops to $< 0.8 \cdot 10^{-3}$ cts/(keV·kg·yr) – within the specifications of Phase II. It is hence important to recall that the estimated count rate of these two components in Phase I is not strongly constrained by the data. The ^{42}K -induced background on the p+ electrode was estimated for the scenario providing the highest count rate, i.e. all the ^{42}K ions in the detector bore-hole were located on the p+ surface. The ^{222}Rn background is not fully understood and the value used in our calculation can be inaccurate.

In case these two components were confirmed to be critical, their contribution could still be suppressed using PSD techniques. In Chapter 3, we developed a new PSD method (based on the rt_{5-50} parameter) which allows for a 95% rejection of events in proximity of

⁵The ^{39}Ar activity in LAr is about 1 Bq/kg and the volume instrumented is roughly equivalent to 10^3 kg of argon.

Table 7.3: Background composition expected in GERDA Phase II configuration before (“expected BI”) and after (“residual BI”) the application of active techniques for background reduction. All the BI values are provided in units of 10^{-3} cts/(keV·kg·yr), the background goal of Phase II. Note that values lower than the least significant digit have been rounded up.

Signal			Coaxial			BEGe		
			expected BI	survival probab	residual BI	expected BI	survival probab	residual BI
^{214}Bi	γ		$\lesssim 1.0$		< 0.2	$\lesssim 1.0$	< 0.05	< 0.05
	β	n+ elect	0.2	< 0.2	< 0.04	6.5	< 0.01	< 0.02
	β	p+ elect	< 0.3		< 0.06	< 0.1	< 0.02	< 0.01
^{208}Tl	γ		$\lesssim 1.0$	< 0.01	< 0.01	$\lesssim 1.0$	< 0.01	< 0.01
^{42}K	γ		< 2.0	0.1	< 0.2	< 2.0	0.04	< 0.08
	β	n+ elect	< 0.1	—	< 0.1	< 3.2	< 0.02	< 0.05
	β	p+ elect	2.9	—	2.9	1.3	< 0.08	< 0.10
^{210}Po	α	p+ elect	< 0.1	—	< 0.1	< 0.1	< 0.08	< 0.01
^{222}Rn	α	p+ elect	1.5	—	1.5	0.7	< 0.08	< 0.06
^{60}Co	β/γ	int	< 1.0	$\lesssim 0.05$	< 0.05	< 0.3	< 0.01	< 0.01
^{68}Ge	β/γ	int	—	—	—	< 2.3	< 0.01	< 0.01
Sum			< 10.1		< 5.2	< 18.5		< 0.38

the p+ electrode and groove surface. This was achieved at the cost of a strong reduction of the $0\nu\beta\beta$ acceptance (by 30%) and, for this reason, this PSD method was not considered in Section 7.2. However, the results provided by the rt_{5-50} parameter demonstrate the feasibility of rejecting ^{42}K and ^{222}Rn induced backgrounds on the surface of the p+ electrode. In principle, the efficiency of such a technique could be improved with respect to the rt_{5-50} method, which was not developed for enhancing the sensitivity to the $0\nu\beta\beta$ signal.

The background level at $Q_{\beta\beta}$ for BEGe detectors after the application of the active techniques is significantly better than for coaxial detectors. Although the initial BI is $< 19 \cdot 10^{-3}$ cts/(keV·kg·yr), about a factor two higher than for coaxial, the combined use of the PSD and the anti-coincidence cut brings the final BI below $0.4 \cdot 10^{-3}$ cts/(keV·kg·yr). Given the low count rate of ^{68}Ge , the application of the time-coincidence reduces the final BI of less than 5%. This improvement comes along with a reduction of the $0\nu\beta\beta$ detection efficiency of the order of 1%. Thus, we do not expect this cut to be particularly useful for improving the $0\nu\beta\beta$ half-life sensitivity. Similarly to coaxial detectors, also for BEGe detectors a significant fraction of the final BI is due to surface interactions on the p+ electrode. However, as discussed in Section 6.2.3, the survival probability of these events

after the PSD cut were compatible with zero and the factor assumed in our calculation (8% survival probability at 95% C.I.) is likely to be higher than the true value. In conclusion, the final BI estimated for BEGe detectors in Phase II is more than a factor two lower than the background goal and no critical components have been identified.

The background predictions presented in this chapter have been used to study the range of $0\nu\beta\beta$ half-life ($T_{1/2}^{0\nu}$) values that GERDA will probe as a function of the data-taking live time. The analysis is performed considering the overall exposure of Phase I and Phase II, divided into three subsets: *a*) coaxial detectors in Phase I, *b*) coaxial detectors in Phase II, and *c*) BEGe detectors in Phase II. The statistical treatment of multiple subsets is based on the approach described in Ref. [125] and the software implemented by A. Caldwell.

The relevant parameters assumed for each subset are listed in Table 7.4. These are the amount of ^{76}Ge target mass, the background index, the energy resolution and $0\nu\beta\beta$ detection efficiency. In particular, the detection efficiency of the $0\nu\beta\beta$ signals is separated in different contributions: the fraction of the detector active mass, the percentage of $0\nu\beta\beta$ decays in the active volume that are reconstructed in the 2039 keV peak, and the acceptance of the analysis cuts. The parameters of the Phase I subset (subset *a*) are given w.r.t. the full data set available at the time of this work⁶. The values of the Phase II subsets are instead taken from Table 7.2 and 7.3 (subsets *b*₁ and *c*). In addition, we consider two slight modifications of the parameters used for the coaxial detectors in Phase II. First we consider the application of the rt_{5-50} -PSD cut, which would suppress the ^{222}Rn and ^{42}K count rate on the p+ electrode while reducing to 70% the $0\nu\beta\beta$ acceptance (subset *b*₂). Secondly, we consider the case that these background components were not present at all (subset *b*₃). As previously discussed, this last scenario is probably optimistic but, at the same time, reasonable as the count rate of these background components was likely overestimated and/or not strongly constrained by the data. In addition, its study is useful to evaluate the maximum improvement theoretically achievable using PSD techniques for the rejection of surface events on the p+ electrode⁷.

The limits on $T_{1/2}^{0\nu}$ computed separately for each subset and for their global analysis are shown in Figure 7.1. The global analysis is performed considering at the same time the subsets *a*, *b* and *c* and is repeated changing the values of the subset-*b* parameters (*b*₁, *b*₂, *b*₃). The time axis is shifted to fix the origin at the end of Phase I. In the plot, the time interruption needed to upgrade the apparatus is not considered and the beginning of Phase II coincides with the stop of Phase I.

As already discussed in Section 3.4, the $T_{1/2}^{0\nu}$ limit achievable at the end of Phase I with 20 kg·yr of exposure is $\sim 0.2 \cdot 10^{26}$ yr (90% C.I.). With the beginning of Phase II, the curves become steeper because of the reduced backgrounds index and the increased

⁶The value is computed using the data of all the runs and the detectors from Nov 9, 2011, to Jan 5, 2013 equivalent to an exposure of 15 kg·yr.

⁷This scenario is indeed equivalent to an ideal cut which accepts 100% of the $0\nu\beta\beta$ signal and rejects all background events.

Table 7.4: Summary of the parameters of the subsets used in the global analysis. The mass of ^{76}Ge has been computed considering an average enrichment factor of 86.3% for coaxial and 87% for BEGe detectors. The fraction of active mass and the amount of $0\nu\beta\beta$ events occurring in the active volume and reconstructed in the 2039 keV peak have been estimated with MC simulations. The $0\nu\beta\beta$ acceptance after the PSD cut and the dead-time introduced by the LAr scintillation anti-coincidence cut are here given in terms of $0\nu\beta\beta$ detection efficiency.

subset	^{76}Ge [kg]	BI [cts/(keV·kg·yr)]	FWHM [keV]	$0\nu\beta\beta$ detection efficiency			
				active mass	peak fraction	PSD	LAr veto
a) coax	12.6	$2.2 \cdot 10^{-2}$	4.5	87%	91%		
b_1) coax	15.1	$5.2 \cdot 10^{-3}$	4.5	87%	91%		97%
b_2) coax	15.1	$8.0 \cdot 10^{-4}$	4.5	87%	91%	70%	97%
b_3) coax	15.1	$8.0 \cdot 10^{-4}$	4.5	87%	91%	(100%)	97%
c) BEGe	17.4	$4.0 \cdot 10^{-4}$	2.5	93%	90%	85%	97%

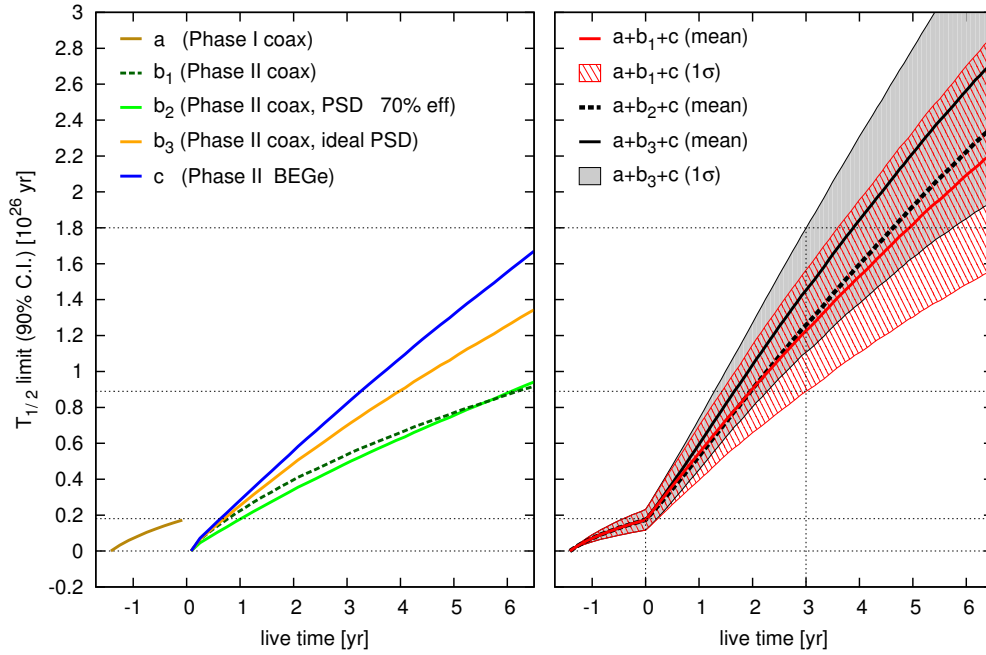


Figure 7.1: Average $T_{1/2}^{0\nu}$ limit (90% C.I.) achievable by GERDA as a function of the data-taking live time. The sensitivity curves are shown for each of the subsets of Table 7.4 (left plot) and for their global analysis (right). The bands show the statistical uncertainty on the average $T_{1/2}^{0\nu}$ limit (1σ). The width of the energy window used to estimate the signal count rate is 7 keV for coaxial and 6 keV for BEGe detectors. The sensitivity curves computed using the average or median value of the $T_{1/2}^{0\nu}$ -limit distribution are practically unchanged.

target mass. The three global sensitivity curves are all relatively close, within 15% in the range of live-time values shown in the plot. In particular, we can see that the application of a PSD cut to reject surface events will not improve the experimental sensitivity, if the $0\nu\beta\beta$ acceptance is lower than 70%. Independently of the curve considered, GERDA will start exploring $T_{1/2}^{0\nu}$ values in the range of 10^{26} yr in less than three years of data taking, reaching $T_{1/2}^{0\nu} = 2 \cdot 10^{26}$ yr in about five years. However, these values refer to the average limit achievable and the sensitivity of a specific realization of the experiment can differ significantly (see 1σ bands in the plot).

7.4 Conclusions and discussion

In this thesis we presented a decomposition of the GERDA Phase I background and a detailed study of the pulse shape discrimination performance achievable with BEGe detectors in Phase II. The results achieved have been used in this last chapter to show the feasibility of the sensitivity goal of Phase II. The BI expected for coaxial detectors after the analysis cuts is at the level of 10^{-3} cts/(keV·kg·yr) while for BEGe detectors is even lower. Given this estimates, the average $T_{1/2}^{0\nu}$ limit achievable within three years of Phase II data-taking is in the range $1\text{--}2 \cdot 10^{26}$ yr.

It should be emphasized that the strong reduction of the BI with respect to Phase I might reveal new background sources not considered in this work. Nevertheless, since these additional contributions are not clearly visible in Phase I, their BI should not exceed 10^{-2} cts/(keV·kg·yr). Considering that all the backgrounds observed so far can be suppressed by more than a factor 10 after the off-line analysis for BEGe detectors, it is reasonable to assume a similar efficiency also for the new components. Thus, even if there are background sources not considered in this analysis, they should not prevent us from reaching the sensitivity goal of GERDA Phase II.

The achievement of these promising results is however contingent to a positive outcome of the current R&D activities, in particular to the development of:

- a new read-out chain (including the front-end electronics) with significantly improved performance compared to Phase I. In particular, the new read-out solution should provide a stability and resolution of the PSD parameters (e.g. the A/E parameter) similar to the results obtained with the detectors in vacuum cryostat;
- hardware and software to monitor and improve the stability of the data-taking, which is essential for the application of PSD techniques and the achievement of the efficiency considered in this chapter;
- a radio-pure mini-shroud which efficiently suppresses the ^{42}K background without blocking the LAr scintillation signal;

- new devices to detect the LAr scintillation light with the same efficiency provided by the MC simulations.

The fulfillment of all the requirements will certainly be challenging. Nonetheless, the expertises acquired during the development of the Phase I apparatus and the analysis of the background data, gives us confidence in the feasibility of these goals.

Summary and outlook

This dissertation focused on the study of the background measured in GERDA Phase I and on solutions for background reduction in Phase II. The latter included the development of the new custom-made HPGe detectors and related pulse shape analysis techniques. Given the background measured in Phase I, we showed that GERDA Phase II has the potentiality to reach its physical goal and start the exploration of $0\nu\beta\beta$ half-life values in the range of 10^{26} yr within a few years of operations. The main outcomes of the dissertation are summarized in the following.

To the purpose of handling the data stream of the GERDA experiment, a new analysis framework has been designed, implemented and benchmarked. Along with the software, we developed and optimized the algorithms used for processing the digitized signals and to monitor the data quality. These tools have been used so far to provide the reference analysis of the GERDA data.

The overall performance of the apparatus has been closely monitored for the first part of data taking and found to meet the experimental requirements. In particular, the energy scale and resolution of the HPGe detectors were found to be stable, with fluctuations in general $\lesssim 1$ keV. The main features of the background energy spectrum have been traced back to sources that were already considered in the design phase of GERDA, although their relative contributions were not known with accuracy. The intensities of the gamma-lines have been estimated to be at least an order of magnitude lower compared to the previous experiments. This improvement reflects also on the count rate at $Q_{\beta\beta}$, which is at the level of ~ 0.02 cts/(keV · kg · yr).

A first decomposition of the GERDA Phase I background at $Q_{\beta\beta}$ has been obtained by the combined use of pulse shape analysis, Monte Carlo simulations and spectral fitting. To this aim, we developed a new pulse shape discrimination technique for the identification of surface interactions on the p+ electrode of coaxial detectors. The method has been designed and benchmarked using both simulated and experimental data and proved to be robust and efficient. The data set considered in the analysis has a total exposure of 6.1 kg · yr and an average background index of $20^{+6}_{-4} \cdot 10^{-3}$ cts/(keV · kg · yr) (runs from 25 to 32). The background at $Q_{\beta\beta}$ was found to be dominated by the high-energy gamma-rays produced in the decay of ^{214}Bi , ^{208}Tl and ^{42}K . Their combined contribution has

been estimated to be $14.7^{+4.8}_{-4.4} \cdot 10^{-3}$ cts/(keV·kg·yr), equally shared between ^{214}Bi and ^{208}Tl with a small contribution from ^{42}K . The gamma-ray count rate is reduced to $11.1^{+5.6}_{-3.6} \cdot 10^{-3}$ cts/(keV·kg·yr) in case of a strong ^{214}Bi contamination on the detector n+ surface. Secondary background components were identified in the beta-rays from ^{42}K and ^{214}Bi , and alpha-rays from ^{210}Po . Given the history of the detectors, also a weak contribution from cosmogenic ^{60}Co is expected.

The second part of the dissertation investigated the BEGe detector design and its combined use with pulse shape discrimination techniques. For a thorough understanding of the BEGe detector pulse shapes, we developed and validated an integrated simulation tool reproducing the response of HPGe detectors to charged particles and radiations. The software relies on the GEANT4 and MAGE packages, to compute the energy depositions inside the Ge crystal, and on an enhanced version of the MGS software, to describe the charge carrier transportation through the crystalline lattice. The signals induced on the read-out electrodes by the movement of the charge carriers are finally convolved with the front-end electronics response and the experimentally measured noise. The simulation has been validated against experimental data and found to be in quantitative agreement. The validation included both data collected with collimated low-energy gamma-sources – producing well localized interactions – and isotropic ^{228}Th measurements – providing events spread across the entire Ge crystal.

Thanks to this simulation tool, we developed the first comprehensive modeling of the signal formation and evolution in BEGe detectors. The characteristic shape of BEGe detector pulses has been traced back to a unique charge collection mechanism. The holes generated by interactions in most of the detector active volume are first collected in the center of the detector, and then drift toward the read-out electrode along a common trajectory. The comprehension of this mechanism – named funnel effect – had strong implications in the design of the detectors and the study of PSD techniques. In particular, it was found to be at the basis of the excellent performance achieved by the A/E method in the discrimination of single-site events ($0\nu\beta\beta$ -like) from multiple-site events (typical of gamma-induced background).

For all the background components observed in Phase I and/or expected in Phase II, we have investigated the discrimination performance that can be achieved with BEGe detectors through pulse shape analysis. Previous studies – leading to the development of the A/E method – had covered exhaustively gamma-emitting sources outside the Ge crystal. In this work, we focused on the actual $0\nu\beta\beta$ signal and the remaining background components. The latter include the cosmogenic isotopes produced in Ge, which create simultaneous multiple-site energy depositions inside the Ge crystal, and external sources emitting alpha- or beta-rays, which produce energy depositions on the surface of the detectors. The results of this study showed that the A/E method can suppress all the considered backgrounds while maintaining a large acceptance of the $0\nu\beta\beta$ signal.

The survival probabilities of $0\nu\beta\beta$ events and decays of cosmogenic ^{68}Ga and ^{60}Co were estimated using our pulse shape simulation tool. These results are remarkable given the difficulties of studying experimentally these signals – produced by decays internal to the Ge crystal – and of reproducing with this kind of integrated simulations the experimental efficiency of a pulse shape discrimination technique. The $0\nu\beta\beta$ acceptance was found to be $(86 \pm 3)\%$, while the internal backgrounds were drastically suppressed to $(0.9^{+0.4}_{-0.2})\%$ for ^{60}Co and $(4.5 \pm 0.3)\%$ for ^{68}Ga . These results – presently dominated by systematic uncertainties – provides a reasonable prediction of the PSD background discrimination efficiency for GERDA Phase II detectors.

To study alpha- and beta-induced backgrounds on the surface of the detectors, several experimental activities have been pursued. The detector response to energy depositions on the B-implanted (p+ electrode) and groove surfaces has been studied through scans with a collimated alpha beam. To this purpose, a BEGe detector was operated in a custom-made cryostat designed to host a movable collimator. Data were found to be consistent with our BEGe detector modeling and no clear surface effects were observed. The survival probability of alpha-induced background – for a slight modified version of the A/E method – was estimated to be $< 8\%$ (95% C.I.). The real value is probably much lower, however measurements on other detectors are needed to check for possible dependences on the Ge material and electrode geometry. Energy deposition in the Li-diffused surface layer (n+ electrode) were studied with low-energy gamma-beams and beta-emitting isotopes. As reported in the literature, interactions in this region of the detector – where the semiconductor junction is located – result in pulses with anomalously long rise time. Thanks to this feature, we found that beta-induced backgrounds at $Q_{\beta\beta}$ can be reduced to $< 1.6\%$ (95% C.I.) with the standard A/E method.

Given the decomposition of the GERDA Phase I background and the estimated pulse shape discrimination performances, we showed that the background achievable in Phase II – after off-line analysis – is at the level of 10^{-3} cts/(keV·kg·yr). Under these assumptions, GERDA will set new limits on $T_{1/2}^{0\nu}$ at the level of $1\text{--}2 \cdot 10^{26}$ yr within three years of data-taking. This result is however contingent to the positive outcome of various R&D activities that are presently ongoing. In particular, to reach the aforementioned pulse shape discrimination efficiencies with BEGe detectors operated in the GERDA setup, the performance of the read-out chain and its stability have to be significantly improved (especially with respect to the A/E parameter).

Contingent on the physics outcome of the current generation of $0\nu\beta\beta$ experiment, the MAJORANA and GERDA collaborations plan to build together a much larger ^{76}Ge tonne-scale experiment and explore $0\nu\beta\beta$ half-life $> 10^{27}$ years. To reach such a sensitivity, a background index at the level of 10^{-4} cts/(keV·kg·yr) and several 1000 kg·yr of exposure are required. The results achieved in this dissertation indicate that, despite the challenges of increasing the target mass, the background reduction strategy of GERDA can address

the requirements of the next generation of experiments. In particular, we showed that BEGe detectors are excellent devices for the $0\nu\beta\beta$ search of ^{76}Ge and their use in Phase II can reduce the background index to $< 4 \cdot 10^{-4}$ cts/(keV·kg·yr). Besides the excellent spectroscopic performance and pulse shape discrimination features, these detectors have a low capacitance, which results in a low noise level and, in turn, a low-energy threshold. Thanks to these characteristics, the design of BEGe detectors can be beneficial also for other ultra-low background experiment searching for weak signals, e.g. light WIMP, neutrino coherent-scattering and neutrino magnetic moment.

Appendix

Appendix A

Framework for digital signal processing and analysis

In this appendix, the design and implementation of the GERDA data analysis framework is presented and discussed. The software is called GELATIO (GERDA LAYouT for Input/Output) [53]. It has been developed to handle the processing and analysis of the detector signals recorded in the GERDA setup and the R&D activities related to the experiment. It is designed to be solid, user-friendly, flexible, maintainable over a long lifetime and scalable to the future phases of the experiment. Thanks to its generic interfaces, it could be used also in other activities involving off-line analysis of digitized pulses. The appendix is organized as follows. In Section A.1 the main requirements driving the software design and the basic concepts of the framework are presented in detail. Section A.2 describes the software implementation and the technical solutions pursued. A few examples about the validation and the application of the framework are reported in the last section.

The software has been developed in collaboration with L. Pandola, P. Zavarise and O. Volynets. The most important contributions of the author concern the concept and design of the framework, the implementation of the modules and the development of the algorithms used to analyzed the signals.

A.1 Concept and design

GELATIO aims to provide a common and flexible analysis platform to the GERDA collaboration, which simplifies the implementation and execution of new analysis as well as the sharing of algorithms and results. To meet these requirements it is important to:

- decouple the algorithm implementation from the IO operations, in particular from the extraction of the traces and other information stored by the FADCs in the raw data.

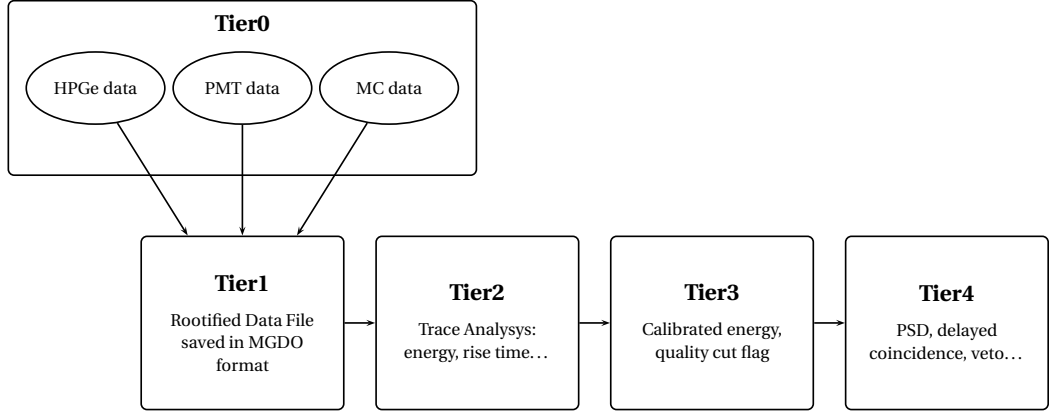


Figure A.1: The hierarchical organization of the data in GELATIO. The framework organizes the output of each step of the analysis in a different level (Tier) starting from the raw data (Tier0) up to the condensed parameter of the final analysis. The Tier1 contains the same information of the raw data but encoded with a different format based on ROOT [126] and MGDO. More details can be found in sect. 3.2.

In this way, the same analysis flow can be applied to data sets acquired with different hardware and / or encoded in different formats

- provide a flexible interface to the signal processing filters allowing the users to carry out easily highly customized analysis
- optimize the computational performances and be cross-platform compatible, hiding the technical aspects to the end users.

The solution worked out is based on two paradigms which are discussed below: multiple level data organization and modular digital signal processing.

A.1.1 Multi-level data structure

The raw data, the information extracted by the signal processing and the analysis results are stored in a hierarchical structure. This approach aims to increase flexibility and enables a multi-user customized data analysis. Alternative analyses can be created as forks of the default one, sharing part of the data flow until a given level and then creating a parallel stream of information. The multi-level structure includes naturally in the framework the conversion of the raw data into a new standardized format which is optimized for signal processing and data storage. After the conversion, all data can be processed along the same analysis stream independently of the parent data acquisition (DAQ) system data format.

The multi-tier structure is depicted in Figure A.1. The raw data provided by the different DAQ systems and by the Monte Carlo simulations are stored in the lowest level (“Tier0”).

The data are then converted into a new encoding and stored as “Tier1”. The first two tiers contain exactly the same amount of information, the only difference being that while the Tier0 is the native DAQ format, the Tier1 is a standardized format that can be chosen to be solid, flexible, exportable and easily readable. The Tier1 data are distributed to the GERDA collaborators as the starting point for the analysis. Higher-level tiers – which are produced from the Tier1 – are meant to contain the analysis results. The “Tier2” files store the output information obtained by applying the digital analysis to the individual traces of each event, as rise time, amplitude, average noise, baseline average value, etc. Similarly, the “Tier3” files store information extracted from the Tier2, e.g. the actual energy spectrum obtained by calibrating the amplitude spectrum with the appropriate calibration curves. As the analysis becomes more and more refined (noise rejection, pulse shape discrimination analysis, delayed coincidence, veto, etc.), the information can be stored in higher-level tiers.

A drawback of this approach is the additional request for disk space due to the coexistence of the same information in both the Tier0 and the Tier1. However the GERDA collaboration decided to perform a blind analysis and the events with energy close to the region of interest ($Q_{\beta\beta}$ of ^{76}Ge) have to be removed from the data set. Consequently, the raw data cannot be distributed and the data blinding is naturally applied in the conversion of raw data to Tier1.

A.1.2 Modular digital signal processing

The core of GELATIO is the digital signal processing which creates the Tier2 files starting from the detector signals stored in the Tier1. In this step different algorithms are applied to the signals in order to extract efficiently the pulse shape information, for instance maximum amplitude, rise time, baseline slope, etc. In gamma-ray spectroscopy these operations are usually performed by chains of elementary digital filters (differentiation, integration, deconvolution, etc.) optimized to reduce the noise and to extract the information with high precision.

To support a highly customizable analysis, the design of GELATIO is based on a modular approach. The analysis is divided into modules, each handling a unique and consistent task of the digital data processing, as for instance energy reconstruction and baseline subtraction. Each module includes a chain of elementary digital filters which is optimized to extract the information of interest from the signal trace. The computed information as well as the shaped traces can be used as input for other modules. The list of active modules and the parameters used by the internal chain of filters are controlled by the user through an appropriate ASCII initialization file (INI file).

This design provides a wide flexibility as complicated chains of modules can be created by the user in an open and transparent way through the INI file. The same module can be run many times within the same execution and used in different chains, each time with different sets of parameters. Moreover, the user can easily create new modules implementing his own

customized analysis tasks. The new modules are immediately available for registration in the INI file and can be combined with the standard ones to create new chains. The data flow and the INI file of an illustrative analysis are reported in Figure A.2 and Figure A.3, respectively.

A.2 Implementation

The core of the framework is implemented in C++ to ensure an easy and natural interfacing with several scientific general-purpose projects. This choice provides also high computational performances, wide flexibility thanks to the object-oriented programming support, and cross-platform compatibility. GELATIO depends on the CLHEP [127] and FFTW3 [128] libraries for scientific computing, and on the ROOT [126] and TAM [129] libraries for the management of the modular analysis, the data storage and the graphical tools. All the external software packages mentioned above are freeware and open-source. GELATIO additionally depends on the MGDO package [130] for the basic digital signal processing algorithms and for the definition of the objects used to encapsulate the information in the Tier1 output. MGDO (Majorana-GERDA Data Objects) is a set of libraries that are jointly maintained and developed by the Majorana and GERDA collaborations. They are specifically designed to improve the encapsulation and the handling of complex data as dedicated C++ objects.

GELATIO is distributed to the GERDA collaborators in the form of a source code. It can be compiled on any platform supporting GNU C++, including Linux and MacOS. A `configure` script takes care of setting automatically the appropriate paths and environment variables necessary to compile the code. The installation procedure has been successfully tested on both 32- and 64-bit operating systems.

To ensure flexibility and good computational performances, the framework includes both compiled and interpreted code. In Section A.2.1 and Section A.2.2 the implementation of the two executables in charge for the raw data to Tier1 conversion and for the actual modular data analysis (Tier2 production) are described in detail. Then the suite of Bash and Python scripts to handle the data streaming through the different tiers is presented in Section A.2.3. Section A.2.4 eventually describes the graphical interface used to display the event traces, define the shaping parameters and create the INI files.

A.2.1 Conversion of raw data to the analysis format

The binary data format chosen for Tier1 is a ROOT file containing a `TTree` of MGDO objects (`MGTEvent` and `MGTRun`). The MGDO objects employed in the Tier1 output are containers which encapsulate the basic information of individual events (signal traces, time stamps, DAQ flags, etc.) and of runs (start and stop times, run type). The usage of a

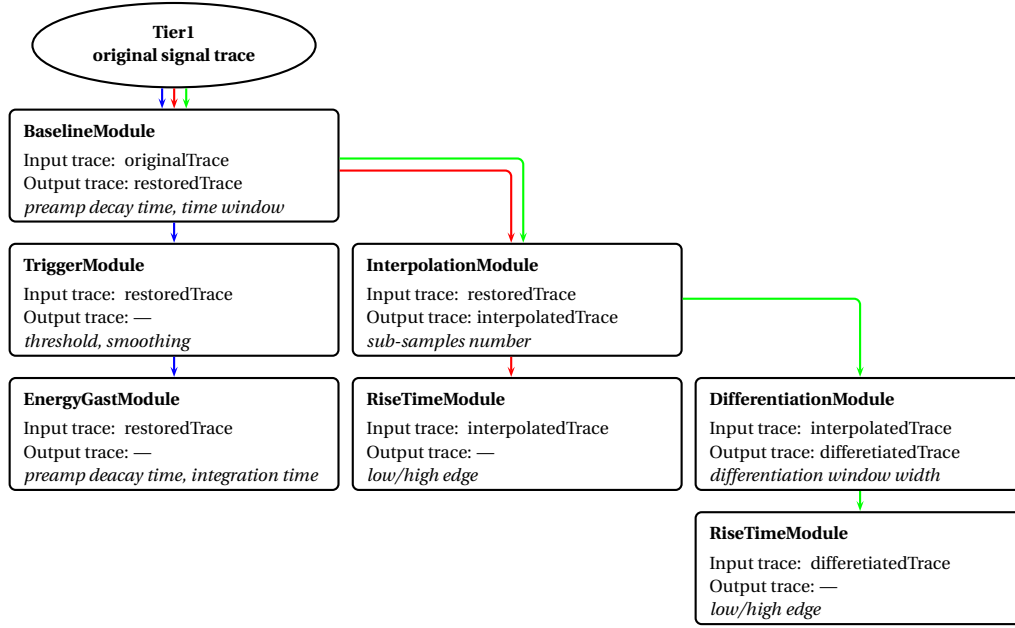


Figure A.2: Data flow of an illustrative analysis which uses three chains of modules. The first chain (blue arrows) reconstructs the event amplitude. It includes the following steps: baseline restoration, pile-up correction (*BaselineModule*) and localization of the pulse leading edge (*TriggerModule*). The output trace of *BaselineModule* and the trigger computed by *TriggerModule* are used as input for *EnergyGastModule*, which reconstructs the pulse amplitude according to the Gast moving-window-deconvolution approach [107]. The second chain (red arrows) extracts the rise time of the signal. The output trace of *BaselineModule* is interpolated by *InterpolationModule*, to push the time resolution below the sampling frequency, and finally sent to *RiseTimeModule*. The last chain (green arrows) computes the rise time of the derivative of the signals (current signal). The first three modules are shared with the second chain. The output signal of *InterpolationModule* is fed to *DifferentiationModule* to compute the numerical derivative, and eventually is parsed to a second instance of *RiseTimeModule*. The figure shows for each module the input and output trace (second and third line) and the main parameters used by the internal algorithms (last line).

```

[Parameters]
FileList=tier1_r01.root tier1_r02.root
OutputFile=output.root
LogFile=output.log

[TaskList]
Task_BaselineModule_1=true
Task_TriggerModule_1=true
Task_EnergyGastModule_1=true
Task_InterpolationModule_1=true
Task_RiseTimeModule_1=true
Task_DifferentiationModule_1=true
Task_RiseTimeModule_2=true

[Task_BaselineModule_1]
InputTraceName=originalTrace
OutputTraceName=restoredTrace
BaselineRestorationStart=100ns
BaselineRestorationStop=2us
TauPreamp=47us
PileUpCorrection=true

[Task_TriggerModule_1]
InputTraceName=restoredTrace
NumberOfSigmaThs=3
TimeAboveThs=100ns
IntegrationWindowWidth=50ns

[Task_EnergyGastModule_1]
InputTraceName=restoredTrace
DifferentiationWindowWidth=10us
IntegrationWindowWidth=8us
FlatTopPosition=0.4

[Task_InterpolationModule_1]
InputTraceName=restoredTrace
OutputTraceName=interpolatedTrace
SubSampleNumber=10

[Task_RiseTimeModule_1]
InputTraceName=interpolatedTrace
LowEdge=10
HighEdge=90

[Task_DifferentiationModule_1]
InputTraceName=InterpolatedTrace
OutputTraceName=differentiatedTrace
DifferentiationWindowWidth=50ns

[Task_RiseTimeModule_2]
InputTraceName=differentiatedTrace
LowEdge=10
HighEdge=90

```

Figure A.3: Example of an INI file implementing the analysis described in Figure 2. The INI file is organized in blocks. The first two blocks (Parameters and TaskList) are used to define the input and output files and to register the list of modules, respectively. The following blocks are used to define the parameters of the registered modules, as for instance the input and output traces.

ROOT files has many advantages, most notably the streamers of the ROOT objects, the compression routines and the interface to the ROOT graphic utilities.

The conversion of raw data in the Tier1 format is performed by the executable **Raw2MGDO**, which accepts a list of raw data files and lets the user customize the name and the number of the output files. The framework contains dedicated classes (“Decoders”) which are used by **Raw2MGDO** to decode the supported binary raw files, in order to read the information to be copied to the Tier1 structure. At the moment, six different decoders are available in GELATIO, supporting all data formats currently employed in the GERDA activities. The decoders take care of extracting the information from the raw file and of all the required preprocessing – as endianness inversion – before writing them in the ROOT file. The GELATIO decoders inherit by the same virtual base class, in order to improve flexibility and to avoid code duplication. The common interface defined by the virtual base class eases the extension / upgrade of the present decoders as well as the implementation of new decoders to read any other binary data format.

Such an approach makes the framework able to handle in a completely transparent way a data stream containing an unspecified number of DAQ channels, each with digitized traces

of unspecified length. This is required because the number of operational detectors and the digitization parameters will change during the experiment lifetime. Similarly, GELATIO is able to handle a mixed stream coming from different types of detectors (e.g. HPGe detectors and PMTs in LArGe [94]). Also the simulated traces can be treated in the same way of the experimental data and be processed along the same analysis flow, enabling an easy and direct Monte Carlo-to-data comparison.

The computational performances of the conversion program are affected by the encoding and type of raw data and by the ROOT compression options required. For instance, a typical GERDA calibration run (about $3.5 \cdot 10^6$ waveforms, each having 4096 samples, total size about 30 GB) is completely converted into the Tier1 format in about 100 minutes using a single thread¹. The processing time is substantially reduced if the ROOT compression option is switched off, at the expense of additional disk space. It has to be emphasized that the conversion of raw data into the Tier1 format must be done only once, so the best compromise is usually to pay in CPU computing time to obtain a smaller output.

A.2.2 Implementation of digital signal processing

To implement the modular analysis following the design discussed in Section A.1.2, the framework relies on the Tree-Analysis Module (TAM) package. TAM [129] is a free package for ROOT developed to provide a very general and modular interface for analyzing data stored in a **TTree**. The software combines the features of two ROOT objects: the **TSelector** method for processing trees and the **TTask** for handling a hierarchical structure of modules in a user-transparent way.

In GELATIO each analysis module is a concrete class derived by the basic interface **TAModule** provided by TAM via an additional GELATIO-specific base class named **GERDAModule**. TAM is used to handle the event loading from the Tier1 file, the exchange of information among different modules and the object output list. Moreover, the interfacing with TAM ensures the compatibility with the ROOT extension PROOF (Parallel ROOT Facility) [131] enabling the software to run several threads in parallel.

The executable in charge of the Tier2 creation takes care to instantiate the TAM interface (initializing the analysis modules according to the instruction provided through the INI file) and to store all the outputs of the same execution in a single ROOT file. The output is a collection of ROOT objects usually containing a **TTree** for each module but also histograms or signal traces. The software provides also a master **TTree** which can be used for unrestricted and parallel access to information contained in any other **TTree** in the file, via the ROOT friendship mechanism.

¹ The testing and benchmarking of GELATIO has been performed on a server running Scientific Linux 5.5 64-bit and mounting a Dual Xeon E5620 CPU (2×4 cores at 2.4 GHz with 2×12 Mb cache), 16 GB of RAM, and 20 hard-disks (2 TB) connected through a SATA 3 Gb/s interface and operated in RAID6/XFS.

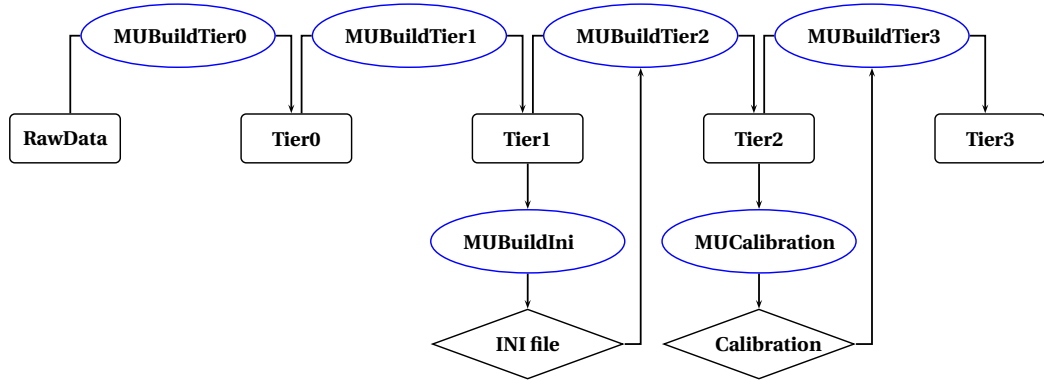


Figure A.4: Data flow of the information through the different tiers performed by using the suite of utilities (blue nodes) included in GELATIO. These utilities are designed to provide an interface to import raw data in the framework, convert them into the Tier1 format, create the INI file and run the digital signal processing. Moreover, the utilities allow the user to perform an interactive and graphical calibration of the amplitude spectra.

The CPU time required to run an analysis depends on the number of active channels and modules as well as on the module parameters. A typical calibration run containing $3.5 \cdot 10^6$ traces, each 4096 samples long, is processed according to the GERDA standard analysis chain in less than 4 hours by using a single thread of the reference benchmark machine.

A.2.3 Utilities

To help the handling of the data stream through the different tiers, GELATIO includes a suite of utilities implemented as Bash and Python scripts. The utilities work over a well-defined directory structure (“analysis file system”) and provide a user-interface for each step of the analysis. The scripts take care of identifying which files should be processed and of storing the results of each step in the proper directory, including a log file collecting the standard outputs generated by the executables. Since the information is stored in fixed directories inside the file system, each user is immediately able to recover any output.

In Figure A.4, the steps of the data flow are depicted together with the associated utility. The utilities up to the Tier2 builder are implemented as simple Bash scripts and are designed to provide an interface to the file system and to run the GELATIO executables with the proper options. The last two routines are more complicated as they are supposed to provide to the user an interactive graphical tool to calibrate the energy spectra and to create the Tier3. Moreover, they take care of storing the calibrating parameters of each channel in different directories of the output TFile, together with all the information important for the debugging, i.e. the calibration log files and the plots of the fits. These utilities

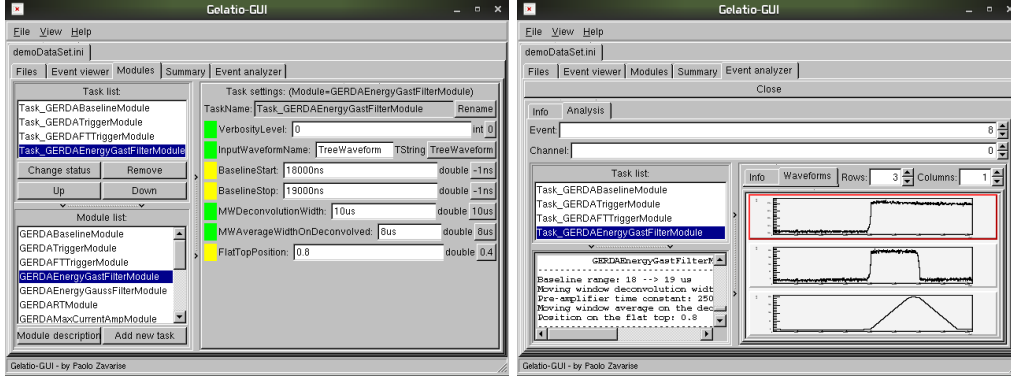


Figure A.5: Illustrative screen shots of the GUI provided by GELATIO.

are implemented in Python to take advantage of the ROOT binding PyROOT which enables cross-calls from Python to ROOT/CINT [126].

A.2.4 The graphical interface

The graphical user interface (GUI) of GELATIO has been developed by P. Zavarise using the graphical components provided by ROOT. The native ROOT solution has been preferred to the usage of more flexible and practical graphical libraries in order to ensure the integration with the rest of GELATIO and to minimize any further external dependency.

The GUI aims to help the user in the creation and in the testing of the INI files. The list of modules can be simply defined by selecting the desired entries from a list. When a module is selected, the GUI displays a list of the customizable parameters and the user can change the default values. The interface warns the user through a color-code label if the values entered are not correct, i.e. values out of the admitted range or wrong physical units.

The signal analysis implemented in the INI file can be tested by visualizing the input/output traces of each module and of each intermediate step of the shaping through the chain of elementary filters included in each module. This feature proved to be extremely useful for debugging the analysis chain and for optimizing the analysis parameters. A further important function of the interface is to provide a flexible multi-channel event viewer to browse channel-by-channel the events contained in the selected Tier1 files. Figure A.5 shows the layouts of the GUI in charge of creating the INI file (left panel) and of visualizing the analysis processing (right panel).

A.3 Application and Benchmarking

The framework has been used up to now to handle and analyze data from several GERDA-related activities, including calibrations with radioactive sources. In particular, GELATIO

has been used for the data analysis of all the GERDA R&D activities related to the Broad Energy Germanium (BEGe) detectors presented in this thesis. The present analysis of the LArGe data is based on GELATIO; in this case, the framework is able to handle the data streams coming from the HPGe detector and from the PMTs of the instrumented liquid argon veto. Finally, the framework has been used to provide the reference analysis of the GERDA data during the commissioning and is currently used in GERDA Phase I (handling the flow of 14 HPGe detectors).

Up to now GELATIO was used on data files coming from six independent DAQ systems, differing for binary data format, number of channels, sampling frequency and sampling window. It proved to be able to handle correctly multiple DAQ channels – possibly referred to different kinds of detectors – and pile-up corrections that must be applied for source calibration runs, because of the higher counting rate. The software turned out to be stable and robust. Fixes for the few minor bugs reported since the release of the stable version are made available in regularly-updated versions of GELATIO.

A.4 List of software packages

CLHEP	library that provides C++ utility classes specifically designed for high energy physics simulation and analysis software [127]
FFTW3	C subroutine library for computing the discrete Fourier transform [128]
MGDO	set of libraries designed and implemented by the Majorana and GERDA collaborations to improve the encapsulation and the handling of complex data as dedicated C++ objects
PyROOT	Python extension module that allows the user to interact with any ROOT class from the Python interpreter [126]
PROOF	ROOT extension enabling the software to run several threads in parallel [131]
ROOT	C++ object oriented data analysis framework [126]
TAM	free package for ROOT developed to provide a very general and modular interface for analyzing data stored in a <code>TTree</code> [129]

Appendix B

Module description

This appendix provides a brief description of the modules implemented by the author in the GELATIO framework and used for the analyses discussed in this dissertation. All the parameters of the modules can be set through the INI file as discussed in Section A.1.2.

AveragePulseModule. This module is used to calculate the average pulse of a data sample. One by one, the pulses are aligned in time with respect to the temporary average pulse by minimizing the mean absolute deviation (MAD). If the minimum MAD value is below a defined threshold, the pulse is accepted and the average pulse is recomputed. The module divides the computation into two parts. In the first one (converging loop), the threshold should be set relatively high to ensure the convergence of the average pulse to the most frequent pulse shape. In the second phase, the final average pulse produced in the converging loop is used as first waveform of the new average and, setting a strict threshold, only the correct signals with the right pulse shape are accepted.

BaselineModule. This module analyzes the baseline of a trace, computing the average value, RMS, average residual, slope, etc. It also performs a baseline restoration and, possibly, a pile-up correction. The baseline restoration is a simple shift of the trace, performed along the ADC scale and centering the baseline average value to zero. The pile-up correction consists in the subtraction from the full trace of an exponential function defined as:

$$f(t) = a + b \cdot e^{-t/\tau}.$$

The parameters a and b are estimated by fitting the signal baseline with the function:

$$\tilde{f}(t) = a + b - b \cdot \frac{t}{\tau},$$

given by the first two terms of the Taylor's expansion of $f(x)$.

CurrentPSAModule. The module calculates the current pulse and analyzes its features. The current pulse computation is performed by using a moving window differentiation with customizable width. Optionally, the signal can also be interpolated to increase the time resolution of the parameters extracted (the algorithm is described in *InterpolationModule*). The first step of the analysis is the identification of the absolute maximum of the current pulse and its time position (parameter A and t_A). The falling time from the maximum to a user-defined percentage of A is found by moving backward/forward with respect to t_A . The rise time and the current integral between A and these edges are used to assess the asymmetry of the current pulse shape.

EnergyGastModule. This module reconstructs the event energy according to the Gast moving window deconvolution (MWD) method. The algorithm is composed of a MWD and a moving window average (MWA). The MWD is equivalent to a differentiation and a deconvolution with an exponential function. Its application transforms the charge pulse into a square-wave like signal. By applying a MWA – with smaller width compared to the MWD – the signal is shaped into a trapezoidal signal whose amplitude is proportional to the event energy. For details about the algorithm see Ref. [107].

EnergyGaussModule. Module designed to reconstruct the event energy by using an approximated Gaussian filter. The pulse is (optionally) deconvolved from the exponential decay tail, differentiated and then integrated several times to achieve an approximated Gaussian shaping. The energy information is eventually stored in the maximum amplitude of the quasi-Gaussian pulse.

FADCModule. This module extracts and stores into the Tier2 the information provided by the FADC, e.g. timestamp, decimal timestamp (timestamp in parts of 10^{-9} s), energy, muon veto flag, event type, which channels are active in an event.

FTTriggerModule. The incoming pulse is differentiated and deconvolved with an exponential function through a moving window deconvolution. Then, the pulse is integrated through a moving window average and a leading-edge discriminator is applied over the shaped pulse. It takes as first trigger position the first sample above the threshold. After the trigger, the signal has to stay above the threshold for a defined time otherwise the trigger is rejected and a new trigger is searched for, starting from the first sample below the threshold. The threshold is dynamically defined as the baseline RMS multiplied by a customizable factor. This module provides the starting time of the pulse with lower precision than *TriggerModule*, but yields information about multiple trigger in the same events (pile ups).

InterpolationModule. This module performs an interpolation of the input waveform. The number of sub-sample can be defined in the INI file, as well as the part of the waveform the module has to work on. The interpolation is obtained in two steps. First, we divide each sample of the original waveform in sub-samples without changing the original amplitude. This operation creates spurious frequencies in the waveform, which are above the FADC sampling frequency and are not physical. To remove them, the waveform is integrated using multiple moving average window (MWA) with width equal to the original sampling period (10 ns usually). The number of MWA, related to the efficiency of removing these frequencies, can be defined by the user.

MWAverageModule. This module applies a moving average window to the input pulse and provides the resulting pulse to other modules. To reduce the computation time the module can work only on a part of the waveform (defined as time window).

RiseTimeModule. The module computes the rise time of a pulse, i.e. the time difference between the sample corresponding to the 90% of the maximum amplitude of the pulse and the sample at the 10% of the maximum amplitude of the pulse. The percentages can be set in the INI file. The computation is done in two steps. First the maximum amplitude is computed as difference of the absolute maximum of the pulse and of the average baseline value. Then, the amplitude corresponding to the rise time edges is computed and the first sample below these amplitudes is searched for moving backwards from the position of the absolute maximum. The maximum can be estimated as the average of the amplitudes of more samples. The selection is performed according to a threshold defined as the baseline RMS multiplied by a user-defined factor. The samples around the maximum for which:

$$\text{amplitude} - \text{maximum amplitude} < \text{threshold}$$

are used to estimate the pulse maximum. These samples are searched for starting from the absolute maximum position, moving backwards and forwards, until the condition is valid. It is also possible to use the energy reconstructed by a previous module to estimate the maximum of the pulse.

TriggerModule. This module implements a leading-edge discriminator which takes as trigger position the first sample above the threshold. After the trigger, the signal has to stay above the threshold longer than a defined time interval. Otherwise the trigger is rejected and a new trigger is searched for starting from the first sample below the threshold. The threshold is dynamically defined as the baseline RMS multiplied by a defined factor.

Appendix C

Statistical models

This appendix describes the statistical models used in this thesis. The models have been implemented as dedicated applications based on the BAT analysis toolkit [78] adapting the existing templates. The models are solved using a Bayesian approach and the posterior probability density functions (pdf) is computed through Markov Chain Monte Carlo methods.

C.1 Signal in presence of measured background

The model here described is a simplified version of the statistical treatment discussed in Ref. [30]. The model is used to estimate the rate of a signal given a measured number of counts when *a)* both background and signal are present and *b)* when only background is present. The measurement results are indicated in the following with n_{s+b} and n_b respectively.

The expected average number of counts (λ and ν) can be expressed in terms of the signal and background rates (S and B) and of three scaling factors accounting for the probability of detecting an event in the specific measurement (k_S , k_{B1} and k_{B2}):

$$\lambda(S, B) = S \cdot k_S + B \cdot k_{B1} \quad (\text{C.1})$$

$$\nu(B) = B \cdot k_{B2} \quad (\text{C.2})$$

For instance, if we consider the energy spectrum of a calorimeter detector, the scaling factors would be given by the product of detection efficiency, width of the energy window considered and live time of the measurement. In all the applications of this thesis, k_S , k_{B1} and k_{B2} are considered as constant parameters with known values.

Assuming that both the signal and background events are due to a Poisson process, the probability of measuring n_{s+b} and n_b (likelihood) can be written as:

$$P(n_{s+b}, n_b | S, B) = P(n_{s+b} | S, B) P(n_b | B) \quad (\text{C.3})$$

$$= \frac{e^{-\lambda} \cdot \lambda^{n_{s+b}}}{n_{s+b}!} \cdot \frac{e^{-\nu} \cdot \nu^{n_b}}{n_b!} \quad (\text{C.4})$$

The results of the analysis are extracted from the global posterior probability distribution, which is expressed using the Bayes' theorem in terms of the likelihood function and the prior pdf's for S and B , $P_0(S)$ and $P_0(B)$:

$$P(S, B | n_{s+b}, n_b) = \frac{P(n_{s+b}, n_b | S, B) P_0(S) P_0(B)}{\int P(n_{s+b}, n_b | S, B) P_0(S) P_0(B) dS dB} \quad (\text{C.5})$$

The parameter of interest, usually S , can be estimated marginalizing the global poster pdf:

$$P(S | n_{s+b}, n_b) = \int P(S, B | n_{s+b}, n_b) dB. \quad (\text{C.6})$$

In this thesis, the best estimate is given using the mode of the posterior pdf and the smallest interval. In case of an upper limit (S_x), the value is extracted for a defined probability x (e.g. $x = 68\%$ or 90%) solving the equation:

$$\int_0^{S_x} P(S | n_{s+b}, n_b) dS = x. \quad (\text{C.7})$$

C.1.1 Gamma-line intensities

The model has been applied in Section 2.3 to estimate the intensity of the gamma-lines in the GERDA energy spectrum (see Table 2.2). In this application the parameters were defined as:

- n_{s+b} , number of counts in the signal region, which is defined as a 17 keV window centered at the nominal energy of the gamma-emission ($E_\gamma \pm 4\sigma$ where $\sigma \sim 2.1$ keV, equivalent to a FWHM of 5 keV);
- n_b , sum of the counts in the two 8.5 keV energy windows contiguous to the signal region (from $E_\gamma - 8\sigma$ to $E_\gamma - 4\sigma$ and from $E_\gamma + 4\sigma$ to $E_\gamma + 8\sigma$).
- $k_S = k_{B1} = k_{B2}$, are given by the product of the width of the energy window ($8\sigma = 17$ keV) and the exposure of the data set, i.e. 6.1 cts/(keV·kg·yr) for the enriched detectors and 3.2 cts/(keV·kg·yr) for the natural ones.

The parameters S and B are assumed to be positive and with flat prior probability distributions.

C.1.2 p+ electrode alpha- and beta-event count rate at $Q_{\beta\beta}$

The model has been also used to give the values summarized in Figure 3.11. The count rate below the rt_{5-50} cut is the sum of two contributions: surface events on the p+ electrode and groove region (signal) and gamma-events (background). The model parameters were defined as:

- n_{s+b} , count rate below the rt_{5-50} cut threshold integrated over $Q_{\beta\beta}^{160}$.
- n_b , the corresponding count rate above the band, which is expected to be dominated by gamma-events.
- k_S , efficiency of reconstructing the signal below the band (95%) multiplied for the exposure of the data set (6.1 kg·yr) and the $Q_{\beta\beta}^{160}$ window width (160 keV).
- k_{B1} , gamma-event acceptance below the cut threshold (27%) multiplied for the exposure and the width of the energy window. The acceptance value is extracted from calibration runs using the Compton continuum at 2 MeV created by the 2.6 MeV gamma-line.
- k_{B2} , gamma-event acceptance above the cut threshold (73%) multiplied for the exposure and the width of the energy window.

Also in this application we used flat priors defined only for positive values of the parameters.

C.2 Signal in presence of hypothetical background

This model, similarly to the previous one, aims at estimating the rate of a signal given the measured number of counts when both signal and background are present. However, it is applied when a measurement in presence of background alone is not available and it is substituted with a prior. The expected average number of counts, λ , can be expressed as:

$$\lambda(S, B) = S \cdot k_S + H \quad (\text{C.8})$$

where S is the signal rate, k_S a scaling factors accounting for the probability of detecting a signal event in the performed measurement and H is the number of background events.

The probability of measuring n_{s+b} counts (likelihood) can be now written as:

$$P(n_{s+b}|S, H) = \frac{e^{-\lambda} \cdot \lambda^{n_{s+b}}}{n_{s+b}!} \quad (\text{C.9})$$

The analysis is performed using the global posterior probability distribution, derived using the Bayes' theorem in terms of the likelihood function and the prior pdf's, $P_0(S)$ and $P_0(H)$:

$$P(S, H|n_{s+b}) = \frac{P(n_{s,b}|S, H) P_0(S) P_0(H)}{\int P(n_{s,b}|S, H) P_0(S) P_0(H) dS dH} \quad (\text{C.10})$$

The poster pdf is hence marginalize to extract the quantity of interest:

$$P(S|n_{s+b}) = \int P(S, H|n_{s+b}) dH \quad (\text{C.11})$$

This model has been applied to estimate the total number of gamma-events in the $Q_{\beta\beta}^{160}$ region. The computation is performed using the number of counts above the rt_{5-50} cut threshold in this energy region (n_{s+b}) and considering the cut acceptance of gamma-events extracted by calibration data (73%). The parameter k_S is defined as the product of the gamma-events acceptance, the exposure of the data set and the width of the $Q_{\beta\beta}^{160}$ window. Both S and H are assumed to be positive. The prior used for S is flat, why for H we use a Poisson distribution:

$$P_0(H) = \frac{e^{-\alpha} \cdot \alpha^H}{H!} \quad (\text{C.12})$$

The computation has been performed for $\alpha = 0.5$ and $\alpha = 2.6$. The best value is quoted according to the mode of the poster pdf and the 68% probability smallest interval.

Acknowledgments

First of all, I would like to thank Stefan Schönert, my advisor and mentor, for his guidance, support and encouragement, which made this thesis work possible. His passion for science and positive attitude to life have inspired me every day during these last three years.

I am grateful to Dusan Budjáš and Luciano Pandola for their daily help and support. Most of the work described in this dissertation has been realized in collaboration with them. I really learned a lot from them, and not only about physics.

Thanks to all the members of the GERDA collaboration, working with them has been a great experience. In particular, I am thankful to Bernhard Schwingenheuer for many invaluable comments and suggestions that improved significantly the quality of my work. I thank Neslihan Becerici-Schmidt, Allen Caldwell and Béla Majorovits for their help, for all they have taught me about statistics and the fruitful collaborative work on Phase I background analysis that led to several of the results presented in Chapter 3. Thanks to Paolo Zavarise and Oleksandr Volynets, for the time spent together coding and designing our software. I am grateful to Nuno Fiuza de Barros for providing the suppression factors of the anti-coincidence cut used in Chapter 7 and the help with the preparation of the thesis. I am thankful to Enrico Bellotti, Carla Cattadori and Assunta di Vacri for the help and support with the detector characterization measurements.

A special thank to the members of E15 and the GERDA group at TUM for the nice time spent together and the daily discussions. In particular I would like to thank Marik Barnabé Heider, Tobias Bode, Jozsef Janicsko and Andrea Lazzaro. Most of the work described in Chapter 6 has been realized in collaboration with them. I would also like to thank them, along with Martin Hofmann and Raimund Strauss, for their help during the preparation of this dissertation.

I am particularly thankful to Calin A. Ur, Dino Bazzacco and the AGATA LNL group, for the hospitality and introducing me to gamma-spectroscopy, HPGe detectors and signal processing.

I would like to acknowledge the colleagues of the MAJORANA collaboration, for the valuable and stimulating exchange of information. In particular, I would like to express my gratitude to Jason Detwiler and Michael Marino, for many suggestions about software

design and implementation, and to Reynold Cooper, David Radford and Larry Darken, for the inspiring discussions about detector designs and pulse shape simulations.

The research activities presented in this dissertation have been partially supported by the Munich Cluster of Excellence “Origin and Structure of the Universe”. I acknowledge Prof. M. Linder for giving me the chance to work in his group at the Max-Planck-Institut für Kernphysik during my first year of PhD.

Finiti i ringraziamenti scientifici passiamo a quelli personali. Grazie di cuore a tutti gli amici che si sono presi cura di me e mi hanno sopportato, prima in Italia, e ora in Germania. In particolare grazie ad Andrea, Anna, Alessandro, Coma, Fabiana, la Goga e il Mazza. Un sentitissimo grazie alle mie famiglie, per avermi spinto e sostenuto fino a qui. Grazie a Dr. Po per l’immenso aiuto nella preparazione di questa tesi. Infine, un profondo grazie ad Anna, il cui pensiero e sostegno sono stati indispensabili per arrivare alla fine di questa tesi.

Bibliography

- [1] A. Barabash, *Double Beta Decay: Historical Review of 75 Years of Research*, *Phys.Atom.Nucl.* **74** (2011) 603–613, [[arXiv:1104.2714](#)].
- [2] W. Rodejohann, *Neutrinoless double beta decay and neutrino physics*, *J.Phys.* **G39** (2012) 124008, [[arXiv:1206.2560](#)].
- [3] F. Avignone, S. R. Elliott, and J. Engel, *Double Beta Decay, Majorana Neutrinos, and Neutrino Mass*, *Rev.Mod.Phys.* **80** (2008) 481–516, [[arXiv:0708.1033](#)].
- [4] J. Gomez-Cadenas, J. Martin-Albo, M. Sorel, P. Ferrario, F. Monrabal, et al., *Sense and sensitivity of double beta decay experiments*, *JCAP* **1106** (2011) 007, [[arXiv:1010.5112](#)].
- [5] J. Schechter and J. Valle, *Neutrinoless Double beta Decay in $SU(2) \times U(1)$ Theories*, *Phys.Rev.* **D25** (1982) 2951.
- [6] M. Duerr, M. Lindner, and A. Merle, *On the Quantitative Impact of the Schechter-Valle Theorem*, *JHEP* **1106** (2011) 091, [[arXiv:1105.0901](#)].
- [7] Particle Data Group, C. Amsler et al., *Review of Particle Physics*, *Phys.Lett.* **B667** (2008) 1–1340.
- [8] Particle Data Group, J. Beringer et al., *Review of Particle Physics*, *Phys.Rev.* **D86** (2012) 010001.
- [9] L. Wolfenstein, *Neutrino Oscillations in Matter*, *Phys.Rev.* **D17** (1978) 2369–2374.
- [10] S. Mikheev and A. Y. Smirnov, *Resonance Amplification of Oscillations in Matter and Spectroscopy of Solar Neutrinos*, *Sov. J. Nucl. Phys.* **42** (1985) 913–917.
- [11] S. Mikheev and A. Y. Smirnov, *Resonant amplification of neutrino oscillations in matter and solar neutrino spectroscopy*, *Nuovo Cim.* **C9** (1986) 17–26.
- [12] G. Fogli, E. Lisi, A. Marrone, D. Montanino, A. Palazzo, et al., *Global analysis of neutrino masses, mixings and phases: entering the era of leptonic CP violation searches*, *Phys.Rev.* **D86** (2012) 013012, [[arXiv:1205.5254](#)].

- [13] D. Forero, M. Tortola, and J. Valle, *Global status of neutrino oscillation parameters after Neutrino-2012*, [arXiv:1205.4018](#).
- [14] KamLAND Collaboration, S. Abe et al., *Precision Measurement of Neutrino Oscillation Parameters with KamLAND*, *Phys.Rev.Lett.* **100** (2008) 221803, [[arXiv:0801.4589](#)].
- [15] DOUBLE-CHOOZ Collaboration, Y. Abe et al., *Indication for the disappearance of reactor electron antineutrinos in the Double Chooz experiment*, *Phys.Rev.Lett.* **108** (2012) 131801, [[arXiv:1112.6353](#)].
- [16] DAYA-BAY Collaboration, F. An et al., *Observation of electron-antineutrino disappearance at Daya Bay*, *Phys.Rev.Lett.* **108** (2012) 171803, [[arXiv:1203.1669](#)].
- [17] RENO Collaboration, J. Ahn et al., *Observation of Reactor Electron Antineutrino Disappearance in the RENO Experiment*, *Phys.Rev.Lett.* **108** (2012) 191802, [[arXiv:1204.0626](#)].
- [18] E. K. Akhmedov, S. Razzaque, and A. Y. Smirnov, *Mass hierarchy, 2-3 mixing and CP-phase with Huge Atmospheric Neutrino Detectors*, [arXiv:1205.7071](#).
- [19] INO Collaboration, M. S. Athar et al., *India-based Neutrino Observatory: Project Report. Volume I*, 2006.
- [20] LAGUNA Collaboration, D. Angus et al., *The LAGUNA design study- towards giant liquid based underground detectors for neutrino physics and astrophysics and proton decay searches*, [arXiv:1001.0077](#).
- [21] LBNE Collaboration, T. Akiri et al., *The 2010 Interim Report of the Long-Baseline Neutrino Experiment Collaboration Physics Working Groups*, [arXiv:1110.6249](#).
- [22] E. Otten and C. Weinheimer, *Neutrino mass limit from tritium beta decay*, *Rept.Prog.Phys.* **71** (2008) 086201, [[arXiv:0909.2104](#)].
- [23] C. Kraus, B. Bornschein, L. Bornschein, J. Bonn, B. Flatt, et al., *Final results from phase II of the Mainz neutrino mass search in tritium beta decay*, *Eur.Phys.J.* **C40** (2005) 447–468, [[hep-ex/0412056](#)].
- [24] Troitsk Collaboration, V. Aseev et al., *An upper limit on electron antineutrino mass from Troitsk experiment*, *Phys.Rev.* **D84** (2011) 112003, [[arXiv:1108.5034](#)].
- [25] V. Lobashev, *The search for the neutrino mass by direct method in the tritium beta-decay and perspectives of study it in the project KATRIN*, *Nucl.Phys.* **A719** (2003) 153–160.

- [26] K. Abazajian, E. Calabrese, A. Cooray, F. De Bernardis, S. Dodelson, et al., *Cosmological and Astrophysical Neutrino Mass Measurements*, *Astropart.Phys.* **35** (2011) 177–184, [[arXiv:1103.5083](#)].
- [27] F. Feruglio, A. Strumia, and F. Vissani, *Addendum to: “Neutrino oscillations and signals in β and $0\nu 2\beta$ experiments” [Nucl. Phys. B 637 (2002) 345]: First KamLAND results*, *Nucl.Phys.* **659** (2003) 359–362.
- [28] K. Abazajian, M. Acero, S. Agarwalla, A. Aguilar-Arevalo, C. Albright, et al., *Light Sterile Neutrinos: A White Paper*, [arXiv:1204.5379](#).
- [29] W. Rodejohann, *Neutrino-less Double Beta Decay and Particle Physics*, *Int.J.Mod.Phys.* **E20** (2011) 1833–1930, [[arXiv:1106.1334](#)].
- [30] A. Caldwell and K. Kroninger, *Signal discovery in sparse spectra: A Bayesian analysis*, *Phys.Rev.* **D74** (2006) 092003, [[physics/0608249](#)].
- [31] S. R. Elliott and P. Vogel, *Double beta decay*, *Ann.Rev.Nucl.Part.Sci.* **52** (2002) 115–151, [[hep-ph/0202264](#)].
- [32] M. Gunther, J. Hellmig, G. Heusser, M. Hirsch, H. Klapdor-Kleingrothaus, et al., *Heidelberg - Moscow beta-beta experiment with Ge-76: Full setup with five detectors*, *Phys.Rev.* **D55** (1997) 54–67.
- [33] IGEX Collaboration, C. Aalseth et al., *The IGEX Ge-76 neutrinoless double beta decay experiment: Prospects for next generation experiments*, *Phys.Rev.* **D65** (2002) 092007, [[hep-ex/0202026](#)].
- [34] H. Klapdor-Kleingrothaus, I. Krivosheina, A. Dietz, and O. Chkvorets, *Search for neutrinoless double beta decay with enriched Ge-76 in Gran Sasso 1990-2003*, *Phys.Lett.* **B586** (2004) 198–212, [[hep-ph/0404088](#)].
- [35] O. Chkvorets, *Search for double beta decay with HPGe detectors at the Gran Sasso underground laboratory*, [arXiv:0812.1206](#). PhD Thesis, University of Heidelberg.
- [36] B. Schwingenheuer, *Status and prospects of searches for neutrinoless double beta decay*, [arXiv:1210.7432](#).
- [37] C. Arnaboldi, D. Artusa, F. Avignone, M. Balata, I. Bandac, et al., *A New limit on the neutrinoless beta beta decay of Te-130*, *Phys.Rev.Lett.* **95** (2005) 142501, [[hep-ex/0501034](#)].
- [38] NEMO-3 Collaboration, L. Simard, *The NEMO-3 results after completion of data taking*, *J.Phys.Conf.Ser.* **375** (2012) 042011.

- [39] GERDA Collaboration, I. Abt et al., *GERDA: the GERmanium Detector Array for the search of neutrinoless $\beta\beta$ decay of ^{76}Ge at LNGS, proposal to LNGS* (2004).
- [40] GERDA Collaboration, S. Schoenert et al., *The GERmanium Detector Array (GERDA) for the search of neutrinoless beta beta decays of Ge-76 at LNGS*, *Nucl.Phys.Proc.Suppl.* **145** (2005) 242–245.
- [41] M. Auger, D. Auty, P. Barbeau, L. Bartoszek, E. Baussan, et al., *The EXO-200 detector, part I: Detector design and construction*, *JINST* **7** (2012) P05010, [[arXiv:1202.2192](#)].
- [42] EXO Collaboration, M. Auger et al., *Search for Neutrinoless Double-Beta Decay in ^{136}Xe with EXO-200*, *Phys.Rev.Lett.* **109** (2012) 032505, [[arXiv:1205.5608](#)].
- [43] KamLAND Collaboration, S. Abe et al., *Production of Radioactive Isotopes through Cosmic Muon Spallation in KamLAND*, *Phys.Rev.* **C81** (2010) 025807, [[arXiv:0907.0066](#)].
- [44] KamLAND-Zen Collaboration, A. Gando et al., *Measurement of the double- β decay half-life of ^{136}Xe with the KamLAND-Zen experiment*, *Phys.Rev.* **C85** (2012) 045504, [[arXiv:1201.4664](#)].
- [45] KamLAND-Zen Collaboration, A. Gando et al., *Limit on Neutrinoless $\beta\beta$ Decay of Xe-136 from the First Phase of KamLAND-Zen and Comparison with the Positive Claim in Ge-76*, [arXiv:1211.3863](#).
- [46] E. Fiorini, A. Pullia, G. Bertolini, F. Cappellani, and G. Restelli, *A search for lepton nonconservation in double beta decay with a germanium detector*, *Phys.Lett.* **B25** (1967) 602–603.
- [47] Majorana Collaboration, V. Guiseppe et al., *The Majorana Neutrinoless Double-Beta Decay Experiment*, *IEEE Nucl.Sci.Symp.Conf.Rec.* **2008** (2008) 1793–1798, [[arXiv:0811.2446](#)].
- [48] M. Barnabè Heider, *Performance and stability tests of bare high purity germanium detectors in liquid argon for the GERDA experiment*. PhD thesis, Max Planck Institut für Kernphysik, Heidelberg, May, 2009.
- [49] CANBERRA Broad Energy Ge (BEGe) Detector, URL <http://www.canberra.com/products/485.asp>.
- [50] GERDA Collaboration, K.-H. Ackermann et al., *The GERDA experiment for the search of $0\nu\beta\beta$ decay in ^{76}Ge* , *The European Physical Journal C* **73** (2012) 1–29, [[arXiv:1212.4067](#)].

- [51] GERDA Collaboration, M. Agostini et al., *Measurement of the half-life of the two-neutrino double beta decay of Ge-76 with the Gerda experiment*, *J. Phys. G: Nucl. Part. Phys.* **40** (2013) 035110, [[arXiv:1212.3210](#)].
- [52] M. Agostini, L. Pandola, and P. Zavarise, *Off-line data processing and analysis for the GERDA experiment*, *J.Phys.Conf.Ser.* **368** (2012) 012047, [[arXiv:1111.3582](#)].
- [53] M. Agostini, L. Pandola, P. Zavarise, and O. Volynets, *GELATIO: A General framework for modular digital analysis of high-purity Ge detector signals*, *JINST* **6** (2011) P08013, [[arXiv:1106.1780](#)].
- [54] H. Klapdor-Kleingrothaus, L. Baudis, A. Dietz, G. Heusser, B. Majorovits, et al., *GENIUS-TF: A Test facility for the GENIUS project*, *Nucl.Instrum.Meth.* **A481** (2002) 149–159, [[hep-ex/0012022](#)].
- [55] M. Barnabe Heider, C. Cattadori, O. Chkvorets, A. Di Vacri, K. Gusev, S. Schoenert, and M. Shirchenko, *Performance of bare high-purity germanium detectors in liquid argon for the GERDA experiment*, in *Nuclear Science Symposium Conference Record, 2008. NSS '08. IEEE*, pp. 3513 –3516, Oct, 2008.
- [56] S. Riboldi et al., *A low-noise charge sensitive preamplifier for Ge spectroscopy operating at cryogenic temperature in the GERDA experiment*, in *Nuclear Science Symposium Conference Record (NSS/MIC), 2010 IEEE*, pp. 1386 –1388, Nov, 2010.
- [57] MIZZI Computer Software GmbH, URL www.mizzi-computer.de.
- [58] R. Isocrate et al., *MD2S - Digital sampling electronics for the MARS detector, A data acquisition system for the MD2S digital sampling electronics*, *Laboratori Nazionali di Legnaro - Annual Report* (2004) 226–227.
- [59] C. A. Ur et al., *A data acquisition system for the MD2S digital sampling electronics*, *Laboratori Nazionali di Legnaro - Annual Report* (2004) 228–229.
- [60] S. W. Smith, *The Scientist and Engineer's Guide to Digital Signal Processing*. California Technical Publishing San Diego, California, 1999.
- [61] M. Agostini, D. Budjas, L. Pandola, and P. Zavarise, *GERDA off-line analysis of HPGe detector signals*, *GERDA Scientific Technical Reports* (2011) GSTR–11–012.
- [62] P. Zavarise, M. Agostini, A. Machado, L. Pandola, and O. Volynets, *Off-line data quality monitoring for the GERDA experiment*, *J.Phys.Conf.Ser.* **375** (2012) 042028, [[arXiv:1111.7200](#)].
- [63] I. MacKenzie and J. Campbell, *On the use of the single escape peak in Ge(Li) spectroscopy*, *Nuclear Instruments and Methods* **101** (1972), no. 1 149 – 152.

- [64] N. Becerici Schmidt et al., *Measurement of the half-life of the two-neutrino $\beta\beta$ decay with GERDA*, *GERDA Scientific Technical Reports* (2012) GSTR-12-009.
- [65] WARP Collaboration, P. Benetti et al., *Measurement of the specific activity of Ar-39 in natural argon*, *Nucl.Instrum.Meth.* **A574** (2007) 83–88, [[astro-ph/0603131](#)].
- [66] H. Primakoff and S. P. Rosen, *Double beta decay*, *Reports on Progress in Physics* **22** (1959), no. 1 121.
- [67] C. M. Cattadori, *GERDA status report: Results from commissioning*, *J.Phys.Conf.Ser.* **375** (2012) 042008.
- [68] V. Ashitkov, A. Barabash, S. Belogurov, G. Carugno, S. Konovalov, et al., *Liquid argon ionization detector for double beta decay studies*, [nucl-ex/0309001](#).
- [69] R. B. Firestone and V. S. Shirley, *Table of Isotopes*. Wiley, New York, 1996.
- [70] P. Medina, C. Santos, and D. Villaume, *A simple method for the characterization of HPGe detectors*, in *Instrumentation and Measurement Technology Conference 2004. IMTC 04. Proceedings of the 21st IEEE*, vol. 3, pp. 828 – 1832 Vol.3, may, 2004.
- [71] M. Agostini, C. Ur, D. Budjas, E. Bellotti, R. Brugnera, et al., *Signal modeling of high-purity Ge detectors with a small read-out electrode and application to neutrinoless double beta decay search in Ge-76*, *JINST* **6** (2011) P03005, [[arXiv:1012.4300](#)].
- [72] M. Agostini, A. B. Machado, B. Schwingenheuer, and S. Shoenert, *Pulse shape simulation of a GTF detector*, *GERDA Scientific Technical Reports* (2011) GSTR-11-001.
- [73] D. Gonzalez, J. Morales, S. Cebrian, E. Garcia, I. Irastorza, et al., *Pulse shape discrimination in the IGEX experiment*, *Nucl.Instrum.Meth.* **A515** (2003) 634–643, [[hep-ex/0302018](#)].
- [74] M. Boswell, Y.-D. Chan, J. A. Detwiler, P. Finnerty, R. Henning, et al., *MaGe-a Geant4-based Monte Carlo Application Framework for Low-background Germanium Experiments*, *IEEE Trans.Nucl.Sci.* **58** (2011) 1212–1220, [[arXiv:1011.3827](#)].
- [75] R. Brugnera, A. Caldwell, A. Garfagnini, S. Hemmer, L. Pandola, and P. Zavarise, *Measurement of the ^{42}Ar contamination in natural argon with GERDA*, *GERDA Scientific Technical Reports* (2012) GSTR-12-004.
- [76] R. Aggarwal and A. Caldwell, *Error bars for distributions of numbers of events*, *The European Physical Journal Plus* **127** (2012) 1–8.

- [77] N. Becerici Schmidt and B. Majorovits, *Analysis of the Ra-226 background in GERDA Phase-I*, *GERDA Scientific Technical Reports* (2012) GSTR-12-012.
- [78] A. Caldwell, D. Kollar, and K. Kroninger, *BAT: The Bayesian Analysis Toolkit*, *Comput.Phys.Commun.* **180** (2009) 2197–2209, [[arXiv:0808.2552](#)].
- [79] Kirsch, A., *Simulation of ^{60}Co and ^{208}Tl decays in the Heat Exchanger*, *GERDA Scientific Technical Reports* (2012) GSTR-12-006.
- [80] N. Becerici-Schmidt, “ α -Background characterization for the GERDA experiment.” DPG Spring meeting, Teilchenphysik, 27.2.-2.3. 2012, T109.3.
- [81] Neslihan Becerici-Schmidt, GERDA Collaboration, private communication.
- [82] R. Cooper, D. Radford, K. Lagergren, J. F. Colaresi, L. Darken, et al., *A pulse shape analysis technique for the MAJORANA experiment*, *Nucl.Instrum.Meth.* **A629** (2011) 303–310.
- [83] Canberra Semiconductor NV, Lammerdries 25, B-2430 Olen, Belgium.
- [84] P. Luke, F. Goulding, N. Madden, and R. Pehl, *Low capacitance large volume shaped-field germanium detector*, *Nuclear Science, IEEE Transactions on* **36** (1989), no. 1 926 –930.
- [85] P. Barbeau, J. Collar, and O. Tench, *Large-Mass Ultra-Low Noise Germanium Detectors: Performance and Applications in Neutrino and Astroparticle Physics*, *JCAP* **0709** (2007) 009, [[nuc1-ex/0701012](#)].
- [86] D. Budjas, M. B. Heider, O. Chkvorets, S. Schoenert, and N. Khanbekov, *Pulse Shape Analysis with a Broad-Energy Germanium Detector for the GERDA experiment*, [arXiv:0812.1735](#).
- [87] I. Phillips, D.G., E. Aguayo, I. Avignone, F.T., H. Back, A. Barabash, et al., *The Majorana experiment: an ultra-low background search for neutrinoless double-beta decay*, *J.Phys.Conf.Ser.* **381** (2012) 012044, [[arXiv:1111.5578](#)].
- [88] D. Budjas, *Germanium detector studies in the framework of the GERDA experiment*. PhD thesis, Max Planck Institut für Kernphysik, Heidelberg, May, 2009.
- [89] D. Budjas, M. Barnabe Heider, O. Chkvorets, N. Khanbekov, and S. Schoenert, *Pulse shape discrimination studies with a Broad-Energy Germanium detector for signal identification and background suppression in the GERDA double beta decay experiment*, *JINST* **4** (2009) P10007, [[arXiv:0909.4044](#)].

- [90] M. Agostini, *Characterization of a Broad Energy Germanium detector through advanced pulse shape analysis techniques for the GERDA double-beta decay experiment*, Master's thesis, U. Padova, 2009.
- [91] A. di Vacri, M. Agostini, E. Bellotti, C. Cattadori, A. D'Andragora, A. Garfagnini, M. Laubenstein, L. Pandola, and C. Ur, *Characterization of broad energy germanium detector (BEGe) as a candidate for the GERDA experiment*, in *Nuclear Science Symposium Conference Record (NSS/MIC), 2009 IEEE*, pp. 1761–1767, Nov, 2009.
- [92] M. Agostini, E. Bellotti, R. Brugnera, C. Cattadori, A. D'Andragora, et al., *Characterization of a broad energy germanium detector and application to neutrinoless double beta decay search in ^{76}Ge* , *JINST* **6** (2011) P04005, [[arXiv:1012.5200](#)].
- [93] M. Barnabe Heider, D. Budjas, K. Gusev, and S. Schoenert, *Operation and performance of a bare broad-energy germanium detector in liquid argon*, *JINST* **5** (2010) P10007.
- [94] M. Heisel, *LArGe – A liquid argon scintillation veto for GERDA*. PhD thesis, U. Heidelberg, Apri, 2011.
- [95] M. Agostini, M. Barnabe Heider, D. Budjas, C. Cattadori, A. D'Andragora, A. Gangapshev, K. Gusev, M. Heisel, M. Junker, A. Klimenko, S. Schoenert, A. Smolnikov, and G. Zuzel, *LArGe R&D for active background suppression in GERDA*, *J.Phys.Conf.Ser.* **375** (2012) 042009.
- [96] M. Agostini et al., *Procurement, production and testing of BEGe detectors depleted in ^{76}Ge* , *Nuclear Physics B - Proceedings Supplements* **229-232** (2012), no. 0 489.
- [97] Budjas, D., *Production and test of isotopically modified Ge detectors for GERDA*, in *2nd International Conference on Advancements in Nuclear Instrumentation Measurement Methods and their Applications (ANIMMA)*, June, 2011.
- [98] D. Budjas, M. Agostini, L. Baudis, E. Bellotti, L. Bezrukov, et al., *Isotopically modified Ge detectors for GERDA: from production to operation*, submitted to *JINST*.
- [99] GEANT4, S. Agostinelli et al., *GEANT4: A Simulation toolkit*, *Nucl.Instrum.Meth.* **A506** (2003) 250–303.
- [100] J. Allison, K. Amako, J. Apostolakis, H. Araujo, P. Dubois, et al., *Geant4 developments and applications*, *IEEE Trans.Nucl.Sci.* **53** (2006) 270.
- [101] L. Mihailescu, W. Gast, R. Lieder, H. Brands, and H. Jager, *The influence of anisotropic electron drift velocity on the signal shapes of closed-end HPGe detectors*, *Nucl.Instrum.Meth.* **A447** (2000) 350–360.

- [102] B. Bruyneel, P. Reiter, and G. Pascovici, *Characterization of large volume HPGe detectors. Part I: Electron and hole mobility parameterization*, *Nucl.Instrum.Meth.* **569** (2006), no. 3 764 – 773.
- [103] Z. He, *Review of the Shockley-Ramo theorem and its application in semiconductor gamma-ray detectors*, *Nucl.Instrum.Meth.* **463** (2001), no. 1-2 250 – 267.
- [104] L. Darken. Canberra Semiconductor, private communication.
- [105] See <http://www.caen.it/nuclear/product.php?mod=N1728B>.
- [106] See <http://www.iphc.cnrs.fr/-TUC-.html>.
- [107] J. Stein, F. Scheuer, W. Gast, and A. Georgiev, *X-ray detectors with digitized preamplifiers*, *Nucl.Instrum.Meth.* **113** (1996), no. 1-4 141 – 145.
- [108] M. G. Strauss and R. N. Larsen, *Pulse height defect due to electron interaction in the dead layers of Ge(li) γ -Ray detectors*, *Nucl.Instrum.Meth.* **56** (1967), no. 1 80 – 92.
- [109] CoGeNT Collaboration, C. Aalseth et al., *Results from a Search for Light-Mass Dark Matter with a P-type Point Contact Germanium Detector*, *Phys.Rev.Lett.* **106** (2011) 131301, [[arXiv:1002.4703](#)].
- [110] MAJORANA Collaboration, E. Aguayo et al., *Characteristics of Signals Originating Near the Lithium-Diffused N+ Contact of High Purity Germanium P-Type Point Contact Detectors*, [arXiv:1207.6716](#).
- [111] Christopher O’Shaughnessy, GERDA Collaboration, private communication.
- [112] S. Elliott, V. Guiseppe, B. LaRoque, R. Johnson, and S. Mashnik, *Fast-Neutron Activation of Long-Lived Isotopes in Enriched Ge*, *Phys.Rev.* **C82** (2010) 054610, [[arXiv:0912.3748](#)].
- [113] M. Agostini, M. Barnabe Heider, T. Bode, D. Budjas, A. Lazzaro, and S. Schoenert, *BEGe detector response to alpha-induced energy depositions on the p+ electrode and groove surfaces*, *GERDA Scientific Technical Reports* (2013) GSTR–13–006.
- [114] STRUCK Innovative Systeme GmbH, 22399 Hamburg, Germany.
- [115] T. K. Alexander, J. D. Pearson, A. E. Litherland, and C. Broude, *Pulse-shape discrimination on the gamma-ray pulses from $^{19}\text{F}(d,n\gamma)^{20}\text{Ne}$ observed with a lithium-drifted germanium gamma-ray spectrometer*, *Phys. Rev. Lett.* **13** (Jul, 1964) 86–88.

- [116] M. Agostini, E. Bellotti, L. Baudis, D. Budjas, A. Caldwell, C. Cattadori, A. Di Vacri, V. Kornoukhov, A. Garfagnini, P. Grabmayer, M. Hult, J. Jochum, M. Laubenstein, L. Pandola, G. Pivato, S. Schoenert, M. Tarka, C. Ur, and K. Zuber, “Characterization of BEGe detectors in GERDA.” Workshop on Germanium-Based Detectors and Technologies, 18-20 May 2010, UC Berkeley.
- [117] A. Lazzaro, “Studies of high-purity Ge detector signals.” Master’s thesis, supervisors E. Previtali, S. Schoenert and M. Agostini, U. Milan Bicocca, 2012.
- [118] M. Agostini et al., *Investigation of the ^{42}K background suppression by using bare BEGe detector in LArGe*, *GERDA Scientific Technical Reports* (2012) GSTR–12–016.
- [119] J. Janicsko-Csathy, H. A. Khozani, X. Liu, B. Majorovits, and A. Caldwell, *Development of an anti-Compton veto for HPGe detectors operated in liquid argon using Silicon Photo-Multipliers*, *Nucl.Instrum.Meth.* **A654** (2011) 225–232, [[arXiv:1011.2748](#)].
- [120] Maria Laura di Vacri and Stefano Nisi, Inductively Coupled Plasma-Mass Spectrometric (ICP MS) analyses, LNGS chemistry laboratory, Oct 2012.
- [121] Neslihan Becerici-Schmidt, Stefan Schoenert and Bernhard Schwingenheuer, GERDA Collaboration, private communications and talks at the GERDA Collaboration meeting in Nov 2012.
- [122] Andrea Lazzaro and Dusan Budjáš, GERDA Collaboration, private communication and talk at the GERDA Collaboration meeting in Nov 2012.
- [123] Nuno Barros and al., GERDA Collaboration, LAr instrumentation working group, private communications and talks at the GERDA Collaboration meetings in Jun and Nov 2012.
- [124] Jozsef Janicsko, GERDA Collaboration, private communication.
- [125] A. Caldwell, *Example Analysis & Opening the Blinded Window(s)*, *GERDA Scientific Technical Reports* (2012) GSTR–12–500.
- [126] R. Brun and F. Rademakers, *ROOT: An object oriented data analysis framework*, *Nucl.Instrum.Meth.* **A389** (1997) 81–86.
- [127] L. Lonnblad, *CLHEP: A project for designing a C++ class library for high-energy physics*, *Comput.Phys.Commun.* **84** (1994) 307–316.
- [128] M. Frigo and S. Johnson, *The Design and Implementation of FFTW3*, *Proceedings of the IEEE* **93** (2005), no. 2 216 –231.

- [129] M. Ballintijn, C. Loizides and C. Reed, *Tree Analysis Modules*, URL <http://www.cmsaf.mit.edu/twiki/bin/view/Software/TAM>.
- [130] M. Agostini, J. Detwiler, P. Finnerty, K. Kroninger, D. Lenz, et al., *The MGDO software library for data analysis in Ge neutrinoless double-beta decay experiments*, *J.Phys.Conf.Ser.* **375** (2012) 042027, [[arXiv:1111.7260](#)].
- [131] M. Ballintijn, G. Roland, R. Brun, and F. Rademakers, *The PROOF distributed parallel analysis framework based on ROOT*, *eConf* **C0303241** (2003) TUCT004, [[physics/0306110](#)].